The Graphene Surface Force Balance

A thesis submitted for the degree of

Doctor of Philosophy



Christian Dennis van Engers

Magdalen College, University of Oxford

April 17, 2018

Abstract

The importance of capturing, storing and converting energy, exemplified through the desire for independence from fossil fuels and everyday use of portable electronic devices, has magnified interest in understanding processes at the interface between solids and electrolytes.

This thesis explores different experimental approaches towards measuring surface forces across electrolytes confined between polarizable surfaces in the Surface Force Balance (SFB). The main findings of the thesis concern the fabrication and implementation of *graphene* SFB (gSFB) lenses, which use graphene as transparent conductor for surface force measurements at the solid/electrolyte interface. Such lenses consist of hemi-cylindrical quartz discs, with a reflective coating and a graphene layer supported by epoxy.

The suitability of different graphenes produced using Chemical Vapor Deposition was investigated, concomitant with the development of a fabrication method for such lenses, including the fabrication of uniform epoxy layers and the template stripping of epoxy-supported graphene from mica templates. It was found that the smoothness of the graphene surfaces on the lenses was limited and factors contributing to this limitation are discussed. Analysis techniques were developed for the efficient determination of the contact distance without performing a contact calibration and determination of the radius of curvature using secondary Fringes of Equal Chromatic Order. Using these procedures, the surface and interfacial energy of graphene in dry nitrogen and liquids was determined

by applying JKR-theory to adhesion force measurements.

The presented fabrication and analysis techniques are not limited to gSFB and may be applied to different SFB setups. As such, the exciting prospect of using the newly developed methods in an alternative 3-mirror setup is discussed as well.

The work presented in this thesis contributes two novel techniques for the measurement of surface forces across electrolytes with control of the surface electrical potential and will allow for exciting new experiments.

Acknowledgements

This thesis would not have been possible without the contribution of many different people that I gratefully acknowledge.

First of all, my supervisor Prof. Susan Perkin for her tutelage and her support. I'm particularly appreciative of the scientific freedom I enjoyed, her writing advices and the way she has had my back throughout this project.

Our collaborators in the Materials Department, especially Prof. Nicole Grobert, for her supervision and allowing me to freely enter the lab and grow graphene.

Nico Cousens and Jude Britton, from whom I inherited the project, Vitaliy Babenko for his support in all things graphene, Bruno Zappone for his wisdom, patience and hospitality, and Marco Balabajew for daring to join me on what turned out to be a very nice and exciting collaboration.

I would like to thank everyone in the group I had the pleasure of interacting with on a daily basis for their support, advice, discussions and shared lab antics: Sam, Alex, Ellie, Adrian, Florian, Carla and Romain. I would also like to acknowledge the invaluable contributions of support staff in the SAF (Robert), Begbroke cleanroom (Radka), Lab Services (Levi), building management (Paul & Martin), the mechanical and electrical workshops, and the OMCS.

I am grateful for the financial support of the Zvi and Ofra Meiter Magdalen Graduate Scholarship and travel grants received from the Department of Chemistry and Magdalen

College.

I am thankful to Magdalen College for its provisions, particularly the MCR for good times and unique experiences.

I am indebted to my parents for their love and support, even though they'd rather I stayed closer to home. I thank my sister, Juliette, my friends in the Netherlands who let me leave, and my extended family, for their support.

Finally, I thank my partner for life, Julie Hennegan, for being able to pull me out of my head and her willingness to share life's adventures with me.

Declaration

This thesis is submitted for the degree of Doctor of Philosophy in Physical and Theoretical Chemistry at the University of Oxford. No part of this thesis has been accepted or is currently being submitted for any degree, diploma, certificate or other qualification in this University or elsewhere. This thesis is my own work, except where indicated.

Publications

The following published journal articles and manuscripts in preparation relate to the work conducted in this thesis:

Chapter 2
A.T. Murdock, C.D. van Engers, J. Britton, V. Babenko, S.S. Meysami, H. Bishop, A. Crossley, A.A. Koós, N. Grobert, *Targeted cleaning of copper foil surface impurities for improved synthesis of CVD graphene.*
Carbon 2017, 122, 207-216.

Chapter 3
J. Britton, N.E.A. Cousens, S.W. Coles, C.D. van Engers, V. Babenko, A.T. Murdock, A.A. Koós, S. Perkin, N. Grobert, *A Graphene Surface Force Balance.*
Langmuir 2014, 30, 11485–11492.

Chapter 3, 4, 5
C.D. van Engers, N.E.A. Cousens, V. Babenko, J. Britton, B. Zappone, N. Grobert, S. Perkin, *Direct measurement of the surface energy of graphene.*
Nano letters 2017, 17, 3815-3821.

Chapter 4
M. Balabajew*, C.D. van Engers*, S. Perkin, *Contact-free calibration of an asymmetric multi-layer interferometer for the Surface Force Balance.*
Review of Scientific Instruments 2017, 88, 123903.

Chapter 6
C.D. van Engers*, M. Balabajew*, S. Perkin, *A symmetrically polarizable electrochemical surface force balance.*
In preparation.

Chapter 6
M. Balabajew, C.D. van Engers, A. Southam, S. Perkin, *Potential dependent friction of imidazolium based ionic liquids.*
In preparation.

*Shared first authorship.

Contents

Abstract i

Acknowledgements iii

Declaration v

1 Introduction 1

1.1 Background 1

1.2 The Surface Force Balance 2

1.3 Surface force measurements with control of surface potential 4

1.4 The Graphene Surface Force Balance 7

2 Graphene growth 10

2.1 Graphene growth via chemical vapor deposition 10

2.1.1 Introduction 10

2.1.2 The production of graphene via chemical vapor deposition 11

2.1.3 Parameters important for CVD graphene growth 12

2.1.4 Analysis methods 17

2.2 Materials & Methods 21

2.2.1 Materials 23

2.3 Results & Discussion 25

2.3.1 Few Layer Graphene 25
2.3.2 Single Layer Graphene 30
2.3.3 Liquid Copper 32
2.3.4 Expanding Single Layer Graphene Crystals to mm-Dimensions . . . 34
2.3.5 Targeted removal of copper foil surface impurities for improved synthesis of CVD graphene 38

3 Graphene Transfer and Fabrication of Graphene SFB Lenses 43

3.1 Polymer-Assisted Graphene Transfer 46
3.1.1 Introduction 46
3.1.2 Materials & Methods 50
3.1.3 Results & Discussion 52
3.2 Fabrication of epoxy layers of uniform thickness 56
3.2.1 Introduction 56
3.2.2 Materials & Methods 58
3.2.3 Results & Discussion 61
3.3 Template stripping of graphene from mica 66
3.3.1 Introduction 66
3.3.2 Materials & Methods 67
3.3.3 Results & Discussion 67
3.4 Conclusion 77

4 Analysis of the interference spectra 78

4.1 Introduction 79
4.1.1 The different approaches to analyzing FECO 79
4.1.2 The different FECO orders and their origins in the gSFB 80
4.2 Radius of Curvature 86

4.3 Contact-free calibration 95
4.3.1 Introduction 95
4.3.2 Materials & Methods 96
4.3.3 Results & Discussion 98

5 Measurements using the Graphene Surface Force Balance 110

5.1 Direct measurement of the surface energy of graphene 111
5.1.1 Introduction 111
5.1.2 Materials & Methods 114
5.1.3 Results & Discussion 115
5.2 Outlook for gSFB measurements 121

6 The improved 3-mirror Au setup: new fabrication methods and optics for an old problem 123

6.1 Introduction 123
6.2 The tertiary fringes 127
6.3 Strengths and limitations 138
6.4 Running an experiment 145
6.5 Outlook 146

7 Summary & Outlook 147

Bibliography 150

Appendix A: List of Symbols 162

Appendix B: List of Abbreviations 163

Appendix C: Clean Handling & Practices 165

Chapter 1

Introduction

1.1 Background

Forces between surfaces, and at the interface between liquids and solids govern countless processes in our every-day lives. For example, our understanding of the mechanisms that govern the spreading of liquids on surfaces has motivated the development of coatings for non-stick pans, smudge-free glasses or touch screens, and the prevention of ice formation on airplane wings. At the basis of these technological advances lies the study of what happens at interfaces on the molecular scale, be it between olive oil and your pan, or the surface of a Boeing 747 and water vapor.

In the late 1960's and throughout the 1970's and 80's several important developments would allow for the investigation of surface and interfacial phenomena at the molecular level. In the early 1970's, Tabor, Winterton and Israelachvili reported the first measurements of van der Waals forces between surfaces across air using a so-called "Surface Force Apparatus" (SFA, also known as Surface Force Balance, SFB) [1, 2]. The device was further developed by Israelachvili and others for the use in liquids [3, 4], which allowed for the first direct measurements of electrostatic forces across dilute electrolytes [5, 6]

and structural forces that arise from ordering of molecules in a liquid at the liquid-solid interface [7].

Since the 1970's, many further scientific advances have been made using the Surface Force Balance (SFB). Investigations into electrochemical double-layer, structural and frictional forces in dilute [5, 6, 8] and more concentrated electrolytes [9, 10] have provided a wealth of knowledge into the nature of the solid-electrolyte interface. However, whilst experiments on many different liquids have been performed, almost all of these studies have used the same solid: muscovite mica.

Mica is a highly crystalline, layered aluminosilicate mineral that can be cleaved to reveal atomically smooth single crystal facets of cm^2 in size [11]. The large area atomic smoothness of the mica surface has made it a favored material among SFB users. However, mica is an insulator and therefore its surface electrical potential cannot be controlled. In contrast, many modern scientific questions, for example concerning the behavior of electrolytes in energy storage devices or even biological membranes, concern surface potential changes. Therefore, if the potential of the surfaces could be controlled, it would allow SFB users to address a wider range of problems in interfacial science. For example, it would allow for the investigation of the (dis-) charging dynamics of the electric double-layer in small pores, such as in electric double-layer capacitors, dye-sensitized solar cells or polymer-electrolyte batteries and fuel cells.

1.2 The Surface Force Balance

The Surface Force Balance (SFB) allows for the determination of absolute distances between surfaces in concurrence with the measurement of forces between them at both large (thickness of a hair), and small separations (the size of a molecule). This range of force measurements can be performed by using a surface with large radius, whilst being atom-

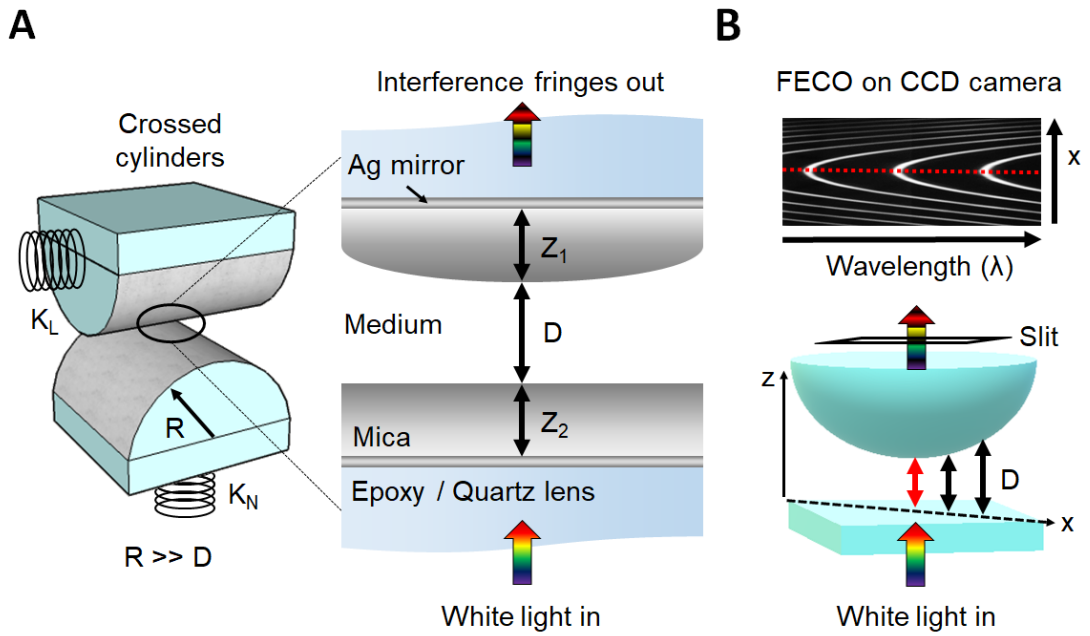


Figure 1.1: *Schematics showing the working principles of the Surface Force Balance. (A) Cylindrical quartz lenses are mounted in crossed-cylindrical geometry. The lenses are attached to springs to allow for the measurement of normal and lateral forces through deflection of the normal / lateral spring with spring contstant* $\boldsymbol{K}_N$ / $\boldsymbol{K}_L$. *Two back-silvered mica crystals are glued down onto the quartz lenses using epoxy. The interferometer is bounded by the two semi-transparent silver mirrors. Between the mirrors, light that interferes constructively over* $\boldsymbol{Z} = \boldsymbol{Z}_1 + \boldsymbol{Z}_2 + \boldsymbol{D}$ *passes through the interferometer. For mica experiments, single crystals of equal thickness are used, and* $\boldsymbol{Z}_1 = \boldsymbol{Z}_2$. *(B) The obtained interference fringes also provide geometric information. At a single wavelength only specific values of* $\boldsymbol{Z}$ *interfere constructively. In cross-cylindrical geometry, equal to a sphere on a flat surface, the value of* $\boldsymbol{Z}$ *increases away from the center (point of closest approach, red arrow). Therefore, the FECO has the shape of an arc. The apex of this arc, positioned at the red dotted line, corresponds to the point of closest approach and lies closest to the blue end of the spectrum.*

ically smooth. In this thesis, the SFB setup as proposed by Kumacheva and Klein [4] is used.

A schematic of the conventional SFB setup is shown in Figure 1.1. Two single crystals of back-silvered muscovite mica are glued silver-side down onto two cylindrical quartz lenses. The cylinders are crossed so that when the radii of the cylinders is the same, their geometry is equivalent to that of a sphere on a flat plane [12]. Forces measured in crossed-cylindrical configuration can be converted to the case of parallel plates, whilst avoiding the difficulty of aligning two plates in parallel.

Determination of the distance between the surfaces relies on the use of multiple beam interferometry (MBI). The interferometer is bounded by the two semi-transparent silver mirrors. Light that interferes constructively passes through the interferometer and emerges as an interference pattern (Figure 1.1-B). This allows the distance **D** between the mirrors to be determined with sub-nm precision. Since white light is used as light source, the distances between the mirrors needs to be larger than at least the diffraction limit of the shortest wavelength used, necessitating the use of a spacer between the mirrors. In the conventional SFB mica is used as spacer.

To measure forces between the surfaces one of the lenses is mounted on a spring with a known spring constant ($\mathbf{K_N}$ in Figure 1.1-A) and moved at a constant velocity towards the other lens. In the absence of any forces, the distance between the surfaces, **D**, decreases linearly. Forces can thus be measured by subtracting the expected surface distance due to the linear motion, from the measured distance, and multiplying with $\mathbf{K_N}$.

The measured forces can be compared to those measured in other experiments via normalization with the radius of curvature (**R**) (Figure 1.1-A). As shown in figure 1.1-B, the spectrometer slit selects a line within the plane perpendicular to the surface normal. Across this line the condition for constructive interference changes due to the constantly varying value of **D**, which is smallest at the point of closest approach between the surfaces. This gives rise to the curved fringes of equal chromatic order (FECO) in the interferogram and provides a direct measure of the surface geometry from which **R** can be determined.

1.3 Surface force measurements with control of surface potential

To extend the range of experiments that can be performed, a variety of SFB-techniques using polarizable materials, rather than mica, have been explored. The simplest approach

is to modify one of the lenses, replacing one of the mica crystals with a thin, transparent layer of template stripped gold. Gold surfaces prepared by template stripping can have RMS roughnesses down to 0.2 nm [13]. This is much rougher than the atomically smooth surface of mica (0.034 nm RMS), but still smaller than the length scales of many forces studied in electrolytes [14]. The low roughness combined with the optical properties and electrochemical stability of gold thus make it a suitable candidate for use as polarizable surface in SFB experiments.

Various groups have employed this asymmetric setup to study the interaction between gold and mica in dilute electrolytes [15, 16], such as the first observation of charge inversion between such surfaces [17]. Other asymmetric setups have been proposed using mica and a Hg droplet [18] or mica and graphene [19]. However, the asymmetry and inability to directly measure or control the electrical potential of the mica surface limits the type of experiments that can be performed and poses challenges to the interpretation of the experimental results.

To overcome these challenges, several symmetric setups have been proposed. The simplest approach relies on having a template stripped metal surface on one lens, and a doubly silvered mica crystal on the other [20]. However, the silver on the mica cannot be prepared via template stripping and has to be deposited directly. It therefore presents a rough surface with a RMS roughness > 1 nm, which makes the technique unsuitable for the measurement of surface forces with small length scales.

A successful symmetric setup was developed by the group of Kurihara in 2008 [21]. Further improvement was reported in 2014 to match the distance resolution of that of conventional SFB [22]. The setup was developed to allow for the use of opaque substrates, such as thick, template stripped metal films. In this setup, distances are not measured by measuring the constructive interference of light between the metal surfaces. Rather, laser interferometry is used to determine the displacement of a mirror situated at the back of

one of the lenses. A drawback of this approach is the loss of optical information. Since light doesn't pass through the studied medium or interfaces, there is no direct measure of changes to the refractive indexes or the surface geometry, such as the radius of curvature or continuity of the metal film. The latter is particularly important when using metal surfaces, which may be damaged due to cold welding. Further, this approach requires significant device modification and involves a more complicated optical setup.

There are several methods complementary to surface force measurements under potential control using the SFB. Among these, the most notable example is the atomic force microscope (AFM). The working principle of the atomic force microscope relies on the measurable interaction between a very sharp cantilever tip and a surface of interest. This allows force measurements to be performed in similar fashion to using a SFB. It is therefore informative to examine differences and similarities between SFB and AFM.

Two factors limit the use of AFM compared to SFB. The first arises in particular when measuring surface forces across liquids. For example, it is difficult to probe forces that arise at a large distance between the tip and the surface. This is due to the small radius of curvature of the tip: interaction forces are averaged over only a small number of molecules. To overcome this limitation, a colloid with a larger radius may be attached to the tip. However, such colloidal probes are generally rough and thus sacrifice force resolution at smaller distances (i.e. present asperities with sizes on the order of the distances probed when at small surface separations).

Another limitation of scanning probe techniques is that only the relative distance between the tip and the surface is measured. When probing the structure of a liquid near a surface, the presence of the interface causes the liquid to obtain an ordered structure [23]. However, from the data obtained using AFM it is not evident whether the forces probed arise due to the structure of the first, second or a layer further from the surface. In other words, the absolute position of the surface is unknown [24]. Finally, measurement

of the radius of curvature of the AFM cantilever tip is difficult and has to be performed *ex situ*.

1.4 The Graphene Surface Force Balance

Although some approaches towards the experimental realization of a symmetrically polarizable SFB setup exist [21, 25], they come with inherent drawbacks and have not seen implementation within the wider SFB community. This thesis proposes, demonstrates and critically appraises the use of an alternative setup: the Graphene Surface Force Balance (gSFB).

Graphene, formally a one-atom-thick infinite sheet of sp^2-hybridized carbon, is a transparent conductor that can be atomically smooth. Since it is only one atom thick and of finite stiffness, it presents a molecularly smooth surface when placed on a sufficiently smooth substrate [14]. As such, it has the potential to meet the criteria for use in a successful symmetrically polarizable SFB: conductivity, a molecularly smooth surface, and optical transparency.

Figure 1.2 shows a schematic of the gSFB setup. The interferometer is bounded by two gold mirrors. The graphene inside the interferometer is glued down onto epoxy. Both the radius of curvature ($\mathbf{R}$) and the diameter of the lenses are $\sim 1\,\mathrm{cm}$. Production of graphene large enough to cover cm^2 areas will be discussed in Chapter 2: *Graphene Growth*.

Measurements of interfacial properties of electrolytes, such as interfacial structure or Debye screening length require force measurements on the length scale of $\mathbf{D} = 20\,\mathrm{nm}$ down to contact [10]. This in turn requires the surfaces to be extremely smooth. Further, the surface geometry, arising from $\mathbf{R}$ and thickness deviations of the epoxy layers ($\mathbf{Z}_{1,2}$), needs to be controlled to be able to correctly interpret the effective radius of curvature. The fabrication of graphene surfaces which are smooth over large areas, supported by epoxy

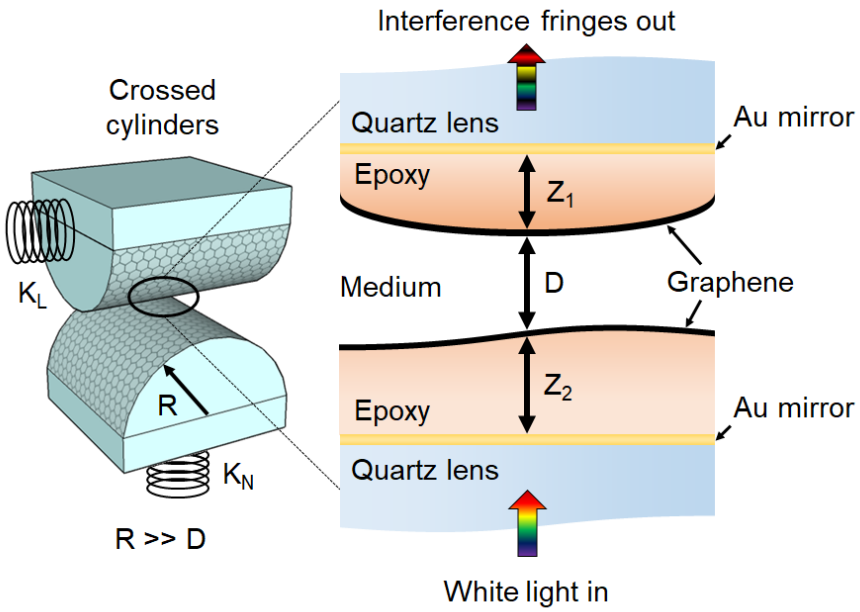


Figure 1.2: *Schematics showing the Graphene Surface Force Balance. The cylindrical quartz lenses are coated with a gold mirror. A layer of epoxy is applied to the gold surface. The graphene is glued down and held by the epoxy layer. Between the mirrors, light that constructively interferes over* $\boldsymbol{Z_1 + Z_2 + D}$ *passes through the interferometer. Due to the use of epoxy the values of* $\boldsymbol{Z_{1,2}}$ *changes across the lens and* $\boldsymbol{Z_1 \neq Z_2}$.

layers of well-defined geometry and thickness will be discussed in Chapter 3: *Graphene Transfer and Fabrication of Graphene SFB Lenses.*

To interpret experimental data and compare measured values to those reported in literature, $\mathbf{D}$, $\mathbf{Z}_{1,2}$, and $\mathbf{R}$ all need to be accurately determined. Chapter 4: *Analysis of the interference spectra*, will discuss the interpretation of the obtained interferometric data and describes methods to determine these values. A method for determination of $\mathbf{Z}_{1,2}$ for the case in which the surfaces cannot be brought into contact as is conventionally done, is also be presented.

Results obtained using the gSFB will be discussed in Chapter 5: *Measurements using the Graphene Surface Force Balance.* This chapter extensively describes measurements of the surface energy of graphene and briefly discusses the outlook for future experiments using the gSFB setup.

Chapter 6: *The improved 3-mirror Au setup: new fabrication methods and optics for*

an old problem, revisits the three-mirror setup proposed by Levins and Vanderlick [20]. It applies the methods developed in this thesis to enable its practical implementation and discussed optimal parameters for the use of this setup.

The thesis will conclude by summarizing the results and describing the exciting potential for future experiments.

Chapter 2

Graphene growth

This chapter describes the growth of graphene for use in the gSFB. First, the choice of graphene production method, chemical vapor deposition (CVD), will be discussed and the literature on the CVD growth of graphene will be reviewed. This will be followed by a short discussion on methods to analyze graphene, with a focus on the methods used for the work presented in this thesis. The second part of this chapter describes the graphene synthesis procedures employed in this work and discusses the adequacy of the obtained graphene films for use in the gSFB.

2.1 Graphene growth via chemical vapor deposition

2.1.1 Introduction

Since the publication of its high carrier mobility in 2004 [26], graphene has received significant attention from the scientific community. In these original experiments, graphene, formally an infinite sheet of sp^2-carbon, was tape-cleaved from highly oriented pyrolytic graphite (HOPG) yielding highly crystalline flakes with diameters up to tens of microns.

SFB experiments require much larger sample sizes (cm^2 rather than μm^2), so a different approach to producing graphene is needed. One method of producing graphene in

large quantities is via the exfoliation of graphite ("top down") via solvo-mechanical or oxidative/reductive treatments. This yields suspensions consisting of a mixture of single and "few-layer" graphene flakes of different size, which may be cast into films. However, the nature of the treatments required for exfoliation, causes intrinsic molecular contamination, roughness and (chemical/physical) heterogeneity to films produced via these methods.

"Bottom up" approaches for producing graphene have also been developed. Between the methods available, the production of graphene through chemical vapor deposition (CVD) on metal substrates is affordable and allows for the production of graphene crystals of cm^2 in size [27], providing smooth films that are both chemically and physically homogeneous.

2.1.2 The production of graphene via chemical vapor deposition

In heterogeneous catalysis, preventing the formation of deactivating carbonaceous layers on metal catalysts has been a long-standing challenge. Conversely, using this process to form few layer graphene (graphite) was proposed as early as 1896 [28] and demonstrated on Ni in 1966 [29].

Catalytically active dehydrogenation catalysts, such as Fe, Ni and Co, allow for growth of graphitic layers at temperatures as low as 600 °C [28]. However, due to the temperature dependent carbon solubility in these metals, the layer thickness of the graphene on these substrates is difficult to control: multiple graphitic layers tend to precipitate during cooling. Addressing this issue, the Ruoff group demonstrated the use of copper (Cu), a catalytically active substrate with a low carbon solubility to grow large areas of single layer graphene via chemical vapor deposition (CVD) in 2009, providing a relatively "simple", cost effective method to grow graphene [27]. This approach ensures that after the first graphene crystals nucleate on the Cu surface and grow together forming a film, no further graphitic layers form, since the graphene serves as an effective gas barrier [67].

This first publication motivated many research groups to investigate graphene production via CVD on copper. The following section will summarize the factors that have been found to be of import for successfully growing single crystal graphene, dealing mainly with the prevention (control) of forming additional graphene layers (bi- or multi-layer) during the growth process.

Due to the variability between CVD systems and complexity of forming a 0.33 nm thick single layer graphene crystal of up to multiple millimeters in diameter, the larger body of literature studies is empirical in nature. The following discussion therefore presents useful guidelines, but does not go into detail with respect to the reaction kinetics involved in the CVD growth of graphene.

2.1.3 Parameters important for CVD graphene growth

Gas composition

CVD growth of graphene on Cu generally involves the use of hydrogen and methane as precursor gasses, and argon as inert carrier gas. The partial pressure of methane directly influences the concentration of carbon on the surface. After physisorption onto the surface, multiple de-hydrogenation steps occur, along with the formation of intermediate C_x-species [30, 31]. When the surface concentration of C reaches a critical concentration, graphene may nucleate. The nucleation of graphene and concomitant consumption of C-species by the graphene nuclei lowers the concentration of other surface C-species to a steady state value [32]. If the steady state concentration is below the concentration required for new nucleation, the graphene flakes can grow without any secondary nucleation occurring.

Hydrogen competes with methane for surface sites and shifts the chemical equilibrium between the formation of graphene or reformation of methane and reaction intermediates. Initially it was thought to influence graphene growth by serving as activator of surface

C-species and etch the graphene flakes. Later it was found impurities are responsible for the etching/activating behavior [33, 34].

Argon is used as non-reactive carrier gas and influences the surface concentration by diluting both reactive gasses. Dilution of the reactive gasses increases control over surface reactions, since the chemical equilibria may be changed without increasing the absolute concentration of carbon on the surface [35].

Modifying the ratio between methane, hydrogen and argon thus allows for control over: whether graphene nucleation occurs; the growth rate and crystallinity (diffusion or reaction limited growth); and secondary nucleation of graphene flakes.

Oxygen was initially neglected as an important reactive gas in the CVD-based growth of graphene. However, many groups have shown that the presence of trace amounts of oxygen can increase growth rates and reduce nucleation by passivating nucleation sites and lowering the activation barrier for attachment of C at the graphene edges [36]. Controlling the presence of oxygen is not trivial and rather than controlling the presence of ppm-levels of O_2, using the copper foil or a supporting substrate as oxygen reservoir has emerged as a strategy for growing large (mm-size) crystals of single layer graphene [37, 38].

Temperature

Growth temperatures are generally in the range of 1000 °C < T < 1080 °C, close to the melting point of copper (1084 °C) [39]. Temperature influences growth rate, nucleation density and dependence of graphene orientation on the crystallographic orientation of the underlying copper. As expected, increasing temperature increases reaction rates and thus increases the growth rate of graphene. However, both the grain-dependent diffusion rates and adsorption/desorption rates of pre-cursor gasses, surface species and byproducts increase as well. This causes the nucleation density to decrease (i.e. surface diffusion becomes slower than adsorption/desorption and species effectively spend “less time on

the surface") and decouples the shape of the growing graphene crystal from that of the underlying copper lattice (growth is no longer limited by the grain-dependent diffusion of C-species, but the incorporation of C-species in the graphene lattice becomes the rate determining step in the growth process) [40, 41, 32].

Temperature also affects the copper surface and bulk, by increasing mobility of grains, impurities and surface atoms.

The growth substrate: topology & surface composition

Surface topography directly influences graphene nucleation density, i.e. a rougher surface will have a higher nucleation density. This may be caused by an increase in local concentration due to boundary layer effects such as turbulent flow arising from the roughness profile of the surface, or a higher prevalence of defects and step edges which lower the energy barrier for graphene nucleation. [42, 43, 44, 45].

Surface composition influences graphene growth by lowering/increasing carbon solubility and diffusion rates. Furthermore, at elevated temperatures increased mobility of impurities in the copper may result in surface segregation of contamination particles. Such particles are often found to increase nucleation rate, possibly due to boundary layer or activation energy lowering effects [46].

The lattice orientation of the copper surface is important as well. Reactivity and diffusion of carbon species depend on crystallographic surface orientation and thus different orientations show different growth rates. Further, as a graphene flake nucleates its orientation is largely determined by the underlying copper lattice. Therefore, graphene crystals grown on polycrystalline copper will have different individual orientations, resulting in a large number of grain boundaries as the individual crystals merge into a film [47].

To circumvent the formation of grain boundaries graphene may be grown on single crystals, such as sputtered copper[111]. However, due to the availability and cost of single

crystal substrates, this approach has not seen wide application. Liquid metals, such as molten copper supported by a solid tungsten substrate, present an alternative method towards the reduction of grain boundaries. However, handling such substrates is difficult due to the strain induced by the re-solidification of liquid on the support, which limits sample size [48, 49].

Surface morphology and composition are the most difficult experimental factors to control (as opposed to gas composition and temperature). Several strategies have been proposed that target either or both:

- Chemical treatment such as electropolishing or immersion in acids or bases: cleaning of impurities, etching of surface layers (which may contain the largest number of impurities due to manufacturing processes) changes to topology due to etching, possible preferential etching of certain lattice orientations [42].

- Heating, for example in H_2 or air: change in surface roughness due to grain growth and surface restructuring or oxidation, removal of impurities due to grain movement, altering species dissolved in copper foil via diffusion [37].

- Mechanical treatment, such as by polishing: decreases surface roughness, but may introduce unwanted contamination [43].

The growth substrate: bulk composition

Whilst surface based reactions comprise the bulk of investigations, the copper bulk influences the growth as well. Primarily, copper was chosen as substrate for graphene growth due to its low carbon solubility, which prevents carbon surface segregation upon cooling. However, during the reaction the copper bulk may act as source/sink for oxygen, hydrogen and carbon. This may cause secondary nucleation of graphene flakes, resulting in the

growth of multiple graphene layers on top of one another when the copper bulk saturates and the carbon concentration at the surface increases [50].

A convenient guide and global picture of the importance of the bulk metal catalyst was provided by the Hofmann group [51]. Their work has highlighted the important difference between bulk composition at the start and the end of the synthesis and its influence on the growth of single layer graphene. By studying the temporal evolution of the concentration of carbon in the metal growth substrate with respect to the temperature dependent solubility of carbon in the substrate, the following important considerations for the growth of single layer graphene were made:

- Precursor pressure needs to be a balance between the accumulation of carbon at the surface, diffusion into the substrate bulk, and its removal through desorption.
- If not enough of the bulk catalyst substrate is present to buffer the excess of carbon at the surface, small inhomogeneities in carbon concentration at the surface will lead to the formation of secondary layers of graphene.
- Long growth times will lead to saturation of the catalyst bulk and leads to formation of secondary layers of graphene.
- The carbon solubility of metal catalyst substrates is generally lower at low temperature. Rapid cooling of the substrates at the end of CVD growth process prevents precipitation of secondary graphitic layers by preventing C diffusion.

2.1.4 Analysis methods

It is important to characterize the produced graphene, since chemical or physical heterogeneities are expected to impact its performance as surface at the solid/liquid interface in gSFB experiments. For example, impurities, incomplete surface coverage or the presence of multiple layers of graphene may impact the surface chemistry or optical analysis of the obtained interferometric data.

To study the properties of graphene, a wide range of analytical surface science techniques has been used. In this work, Raman spectroscopy, scanning electron microscopy (SEM) and optical microscopy (OM) were employed to qualitatively assess the quality of produced graphene, the morphology and presence of single- or multi-layer graphene, and the surface coverage of the graphene film on the Cu growth substrate respectively.

Many other techniques have been used to study graphene. For example, the measurement of electronic properties such as charge carrier density (and mobility) have been used to quantify the electronic quality (density of scattering impurities) [26, 52]. However, such measurements are out of the scope of this work as graphene is simply utilized as flat, transparent conductor.

The use of Raman spectroscopy, SEM and OM as used in this work is outlined below.

Raman spectroscopy

Raman spectroscopy is the study of the energy loss/gain (Stokes shift/anti-Stokes shift) by photons after being scattered by lattice vibrations. For characterizing graphene, attention has focused on the so-called D, G and 2D bands at $\sim$ 1350 cm^{-1}, 1580 cm^{-1} and 2700 cm^{-1} respectively [53]. There are additional bands, for example at 42 cm^{-1}, sensitive to layer number, but often not accessible due to instrumental limitations [54]. The D-band corresponds to the fully symmetric A_{1g} mode and is activated by the presence of defects.

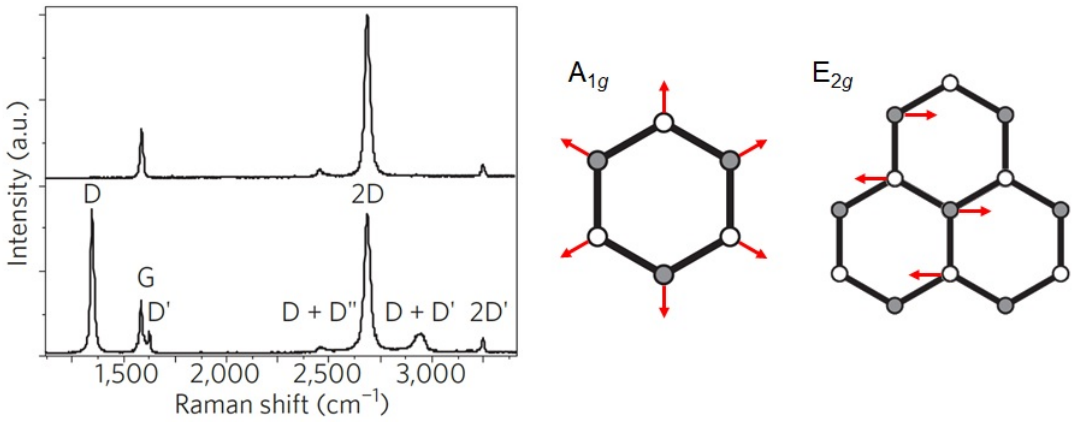


Figure 2.1: *Raman spectrum of pristine (top) and defective (bottom) single layer graphene. The main peaks are labeled. Shown on the right are the A_{1g} and E_{2g} vibrational modes. Figure adapted with permission from Ferrari & Basko, Nature Nanotechnology 2013, 8, 235-246 ([53]). Copyright (2017) Springer Nature.*

The 2D-band is a D-band overtone but requires no defects for its activation. The G-band corresponds to the doubly degenerate E_{2g} mode (see Figure 2.1).

The 2D-band changes significantly from a single Lorenzian to a multi-component peak as the number of graphene layers is increased from single- to multiple layers [55]. Due to the sensitivity to layer number, the ratio between the intensity of the 2D-band (I(2D)) and G-band (I(G)) is commonly used to assess graphene thickness. For turbostratic multilayer graphene – multilayer graphene in which there is little inter-layer interaction due to layer misalignment such as graphene grown using CVD – the 2D-peak is an intense, single Lorentzian as well. However, the width of this peak at half of its height (full width half maximum, FWHM) doubles from ~ 24 cm^{-1} to 45 – 60 cm^{-1} and is upshifted in position by ~ 20 cm^{-1} (when excited at 514 nm) [56]. Excitation wavelength and substrate may also influence the I(2D)/I(G) ratio [57, 58, 59].

The D-band is representative of the number of defects [60] and can even allow for determination of the average distance between defects [57]. In practice, it is used as indicator for the electronic quality of graphene. Ideally the ratio of intensities between the D-band (I(D)) and G-band is on the order of $0.05 < \text{I(D)/I(G)} < 0.3$ [61].

At ~ 2450 cm^{-1} the D+D" band is visible. This band originates from a two-phonon process and is sensitive to layer number [62]. However, due to its low intensity it is often neglected in the analysis of Raman spectra of graphene [63].

Scanning electron microscopy

SEM is used to characterize the shape, layer number and coverage of graphene and serves as a fully complementary technique to the Raman spectroscopy of graphene samples. In SEM, an electron beam is focused onto a surface and scanned in a raster like fashion. The interaction of impinging electrons on the surface produces various signals: secondary electrons (SE) are ejected from the surface due to ionization by the incident beam and are sensitive to the surface; back-scattered electrons (BSE) emerge from deeper in the sample and are sensitive to composition; X-rays emerge because of the relaxation of outer shell electrons to inner shell vacancies and are characteristic of composition. The detection of these X-rays is referred to as energy dispersive x-ray spectroscopy (EDX).

For characterizing graphene, SEM provides a rapid, non-destructive method to identifying the number of layers due to their strong influence on the SE and BSE signals, when operated at low voltage [64, 65]. It can further be used to show the presence of wrinkles and determine the topology of the underlying substrate (e.g. copper). In the case of graphene grown on metal substrates, it also provides qualitative information on the copper grain size, since impinging electrons have a lower scattering cross-section with metal grains which have their main crystallographic axis aligned with the electron beam [66].

Optical microscopy

OM can be used as a quick inspection tool to assess the coverage of graphene on the copper growth substrate. Since graphene prevents the permeation of gasses into the underlying

metal substrate [67], graphene coverage can be assessed by heating the copper substrate: area's that are not covered by graphene will oxidize and cause a change in color of the copper, which is visible using OM and reveals the coverage of the graphene on the copper.

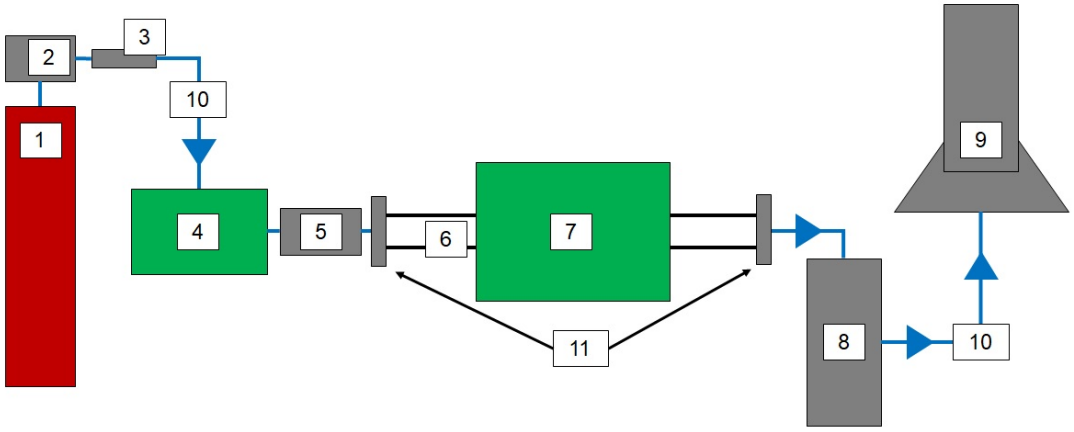


Figure 2.2: *Diagram of the CVD setup: (1) Inlet gas, (2) Flow regulator (to match MFC pressure tolerance), (3) Flashback arrester (in case of flammable gasses), (4) Mass flow controller (MFC), (5) Manual flow control switch, (6) Quartz tube, (7) Tube furnace heating element and thermocouple, (8) Bubbler filled with water, (9) Gas outlet, (10) Stainless steel tubing, (11) Stainless steel flange with o-ring.*

2.2 Materials & Methods

CVD Setup

All graphene films were grown using the same copper substrates (25 μm thick, 99.8% pure, copper foils supplied by Alfa Aesar). Growth was performed inside a quartz tube held in place within a tube furnace. Figure 2.2 shows a diagram representing the CVD-setups used, and shows the gas flow from the gas cylinder (1) (e.g. argon, methane or hydrogen) to the exhaust (9). The quartz tubes were cleaned prior to graphene growth by heating in air at $\geq$ 800 °C. Gas lines were purged with the gasses intended to be used during the synthesis. Sample temperature was controlled by adjusting furnace temperature and sample position. Electrical components (green) are controlled externally via a computer. To move the sample in/out of the hotzone either the quartz tube (6) or the tube furnace (7) can be moved. Arrows indicate direction of gas flow.

Cleaning methods

To clean the Cu foils, they were first degreased, followed by one of the cleaning treatments listed in table 2.1. All listed methods with the exception of electropolishing were performed in a clean glass beaker.

Table 2.1: Overview of Cleaning Methods.

Chemistry	**Procedure**	**Aim**
IPA / acetone	Ultrasonication, 5 min	Degreasing of foil to optimize aqueous follow-up treatment
AcH	Ultrasonication, 5 min	Removal surface contaminants
HNO_3(1:10 v/v with DI)	Immerse, 5 min	Removal of surface species and particulates via surface etching/bubble formation
2M KOH 2M HCl	Immerse, 5 min	Removal surface contaminants particularly CaO, SiO_2, Al_2O_3
Electropolish 1 (EP1): DI, H_3PO_4, EtOH, IPA (10/5/5/1 v/v), urea (1g/210 mL)	4.5 V for 1 min	Removal of surface species via etching, smoothing of surface
Electropolish 2 (EP2): H_3PO_4, urea ($\sim$ 0.5g/100 mL)	1.8 V until current stabilizes to dI/dt $<$ 0.1 A/min	Removal of surface species via etching, smoothing of surface

For electropolishing two procedures were used. The first procedure (EP1) is the same as the one used by Yan et al. [41] and was performed in a glass beaker using a power supply, the Cu growth substrate as cathode and another Cu foil as counter electrode at a potential of 4.5 V. However, whilst appropriate for small foils ($\sim$ 1 x 3 cm^2), this method failed to produce homogeneous surface topography on larger foils ($\sim$ 5 x 10 cm^2). Therefore, for larger foils a different method (EP2) was used, using H_3PO_4 and urea ($\sim$ 0.5 g / 100 mL). For EP2, the copper cathode (growth substrate) and anode were held 1 cm apart, whilst keeping the potential at 1,8 V.

Analysis

During optimization of the graphene synthesis procedure, each graphene-covered Cu foil was carefully characterized using Raman spectroscopy (Raman) and scanning electron microscopy (SEM). However, once a growth protocol was established it was found unnecessary to characterize every sample due to good reproducibility. Therefore, foils were assessed globally using optical microscopy (OM) and SEM and Raman were only performed occasionally.

Raman spectroscopy was performed using a JY Horiba LabRAM ARAMIS imaging confocal Raman microscope using a 532 nm laser. SEM was performed using a JEOL JSM-6500F scanning electron microscope, using a low voltage field emission gun operated between 5-10 kV. OM was performed using a Yenway CX40M metallurgical microscope.

2.2.1 Materials

Tables 2.2, 2.3 and 2.4 list the materials, suppliers and chemicals used.

Table 2.2: Gasses

Name	**Abbreviation**	**Supplier**	**Purity (%)**
Methane	Me	BOC	99.5
Hydrogen	H_2	BOC	99.995
Argon	Ar	BOC	99.999
250 ppm Methane diluted in Argon	Me/Ar	BOC	99.995/99.999
2.5 % Hydrogen in Argon	H_2/Ar	BOC	99.995/99.999

Table 2.3: Liquids

Name	**Abbreviation**	**Supplier**	**Purity (%)**
Ultrapure water	Water	Arium Pro Ultrapure	18.2 MΩ.cm, TOC <2 ppb
Deionized water	DI		
Ethanol*	EtOH	Fischer Scientific UK	Analytical reagent grade
2-Propanol*	IPA	Sigma Aldrich	ACS reagent ≥99.8%
Acetone*	Acetone	Sigma Aldrich	≥99.5%
Chloroform*	$CHCl_3$	Sigma Aldrich	≥99.8%

Continued on next page

Table 2.3 – *Continued from previous page*

Name	**Abbreviation**	**Supplier**	**Purity (%)**
Toluene*	Tol	Sigma Aldrich	≥99.5%
Ortho-phosphoric acid*	H_3PO_4	Sigma Aldrich	ACS reagent
Hydrochloric acid*	HCl	Sigma Aldrich	ACS reagent
Hydrofluoric acid	HF	Microchem Systems	
Acetic acid*	AcH	Sigma Aldrich	≥99%
Nitric acid*	HNO_3	Sigma Aldrich	ACS reagent

*Listed purity or similar used.

Table 2.4: Solids

Name	**Abbreviation**	**Supplier**	**Purity**
Copper foil, 25 μm	Cu foil	Alfa Aesar	99.8%
Tungsten foil, 25 μm	W foil	Alfa Aesar	99.98%
Urea	Urea	Sigma Aldrich	≥ 99%
Potassium hydroxide	KOH	Sigma Aldrich	Reagent grade 90%

2.3 Results & Discussion

The aim of graphene growth for SFB is to produce transparent, smooth, conductive films with as little heterogeneity as possible. At the start of the project, an existing synthesis procedure to produce few layer graphene (FLG) was used. FLG consists of different size crystallites stacked on top of one another, presenting physical (layer number) and chemical (edge v/s basal plane) heterogeneities. In attempt to reduce these, graphene growth was attempted on liquid copper. Later, Vitaliy Babenko, working in the group of Prof. Nicole Grobert, developed a procedure to grow single layer graphene (SLG) with an average grain size of up to 100 μm. Finally, to further increase the grain size, I developed a procedure for the growth of SLG with grain sizes of $\geq$ 1 mm (mmSLG). The effectiveness of different cleaning treatments on the removal of impurities in the copper growth substrate and the effect of these treatments on graphene growth was also investigated.

2.3.1 Few Layer Graphene

The original procedure for FLG growth was developed by Jude Britton in the group of Prof. Nicole Grobert. Minor modifications were made to optimize growth time by adjusting temperature and gas composition.

FLG growth was performed in a quartz tube with an inner diameter of 20 mm on copper foils of 12 x 50 mm^2. Film cleaning was performed using IPA and AcH (initially) or HNO_3. Growth conditions are listed in Table 2.5.

Table 2.5: FLG growth conditions.

		Gas flow (sccm)			
T(°C)	**t(min)**	**Ar**	**Me**	**H_2**	**Step**
RT	10	500			Chamber purge after sample loading
1060	30			300	Annealing of copper foil
1060	45		4.25 – 4.75	300	Graphene growth
RT	10		4.25 – 4.75	300	Sample cooling
RT	10	500			Chamber purge before sample removal

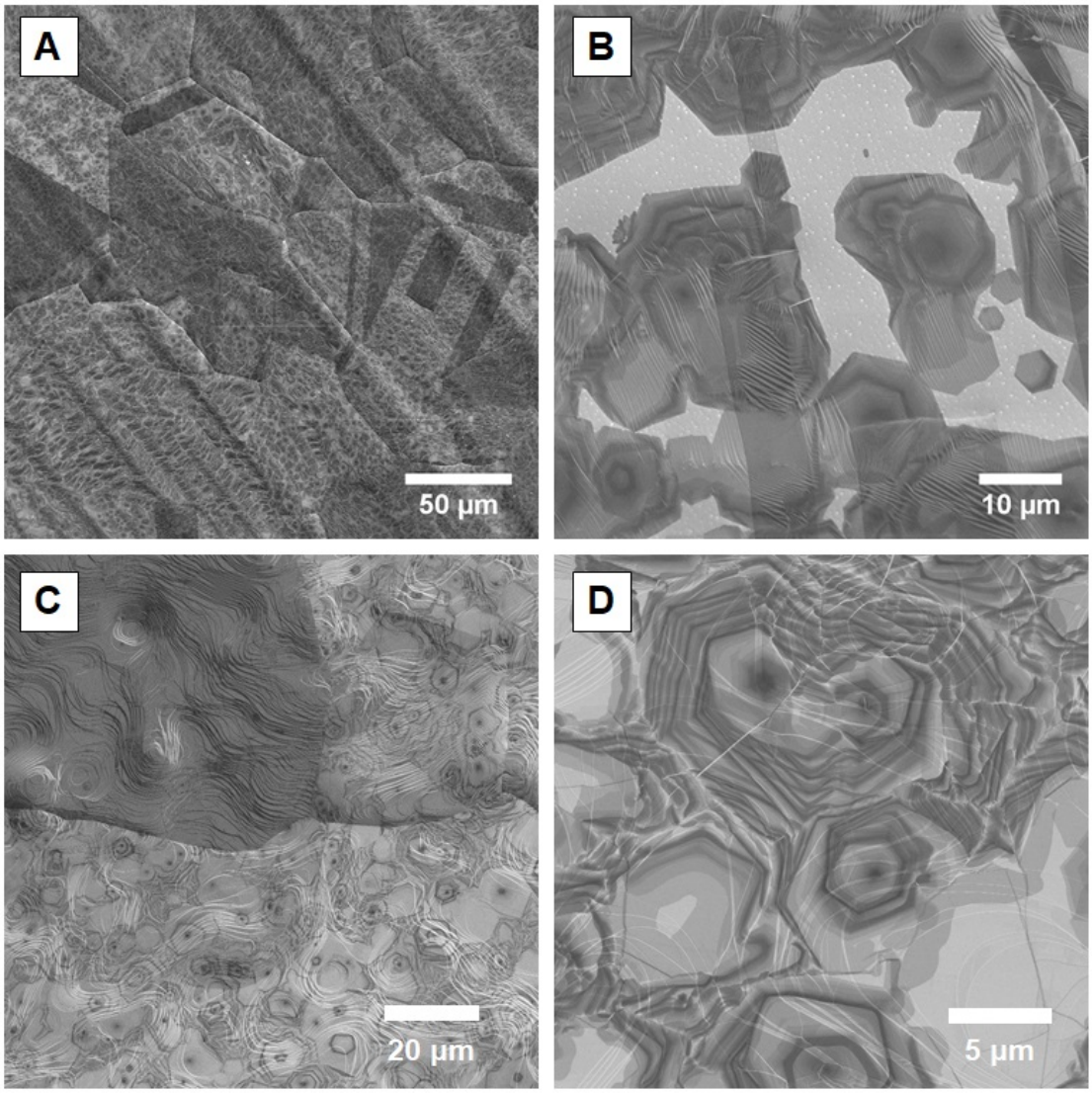


Figure 2.3: *SEM images of few layer graphene on the copper growth substrate prepared according to the procedures described in section 2.3.1. (A) Low magnification image of FLG grown on foils treated with AcH. Diagonal lines, resulting from rolling of the foil during manufacturing are visible. The copper grains are visible as due to the grain dependent contrast of the SE signal. (B) Higher magnification image showing an area not fully covered by graphene. The lighter area corresponds to the bare copper surface. The copper grains and some particles on the copper surface are also visible. Steps in the copper surface are visible underneath the graphene. (C,D) High resulution SEM images of graphene grown on copper foils treated with HNO_3. (C) Due to etching by the HNO_3 the copper underneath the graphene shows pits rather than rolling lines. Copper steps that form underneath the graphene during cooling are also visible. (D) High contrast SE image showing strong layer-dependent contrast of the FLG.*

Figure 2.3-A shows a typical low magnification SEM image of FLG grown on Cu-foil cleaned using the AcH treatment. It shows diagonal lines resulting from rolling during the manufacturing of the Cu-foil, the grain structure of the underlying Cu-foil, and different

thicknesses of graphene as patches. The copper grains are visible due to the difference in interaction of secondary electrons with different orientations of the crystalline copper surface [66]. A similar effect allows an approximate distinction to be made between graphene layers of different thickness [64, 65]. Figure 2.3-B shows an SEM image at higher magnification, in an area where the graphene grains have not fully grown together. The absence of graphene is immediately evident due to the large contrast difference between the graphene-covered and bare Cu surface. Small particulates are visible on the copper surface and underneath the graphene.

Figure 2.3-C,D show SEM images taken by Vitaliy Babenko on the high resolution Zeiss Merlin - Analytical SEM. Figure 2.3-C shows a typical low magnification SEM image of FLG grown on Cu-foil cleaned using the HNO_3 treatment. Due to etching of the substrate, the surface shows pits rather than rolling lines. HNO_3 was used to remove a surface layer and reduce the presence of particulates, whilst maintaining a rough surface required for the growth of FLG. Figure 2.3-D shows a higher magnification image taken using a (in lens) SE detector, providing greatly enhanced contrast. No particulates are visible.

Figure 2.4 shows Raman spectra of graphene on the copper growth substrate (2.4-A) and after transfer to a SiO_2/Si substrate (2.4-B), taken on 5 different locations each. For all spectra, the small I(D)/I(G) ratio is indicative of graphene with a small number of defects [61]. The 2D peak indicates the presence of multiple layers. The variance of the 2D peak shape, further indicates that the FLG at all locations are of different thickness and/or relative inter-flake orientation [55]. The strong background signal on copper is due to scattering of the incident beam by plasmons and reduces the accuracy of the measurement. However, due to the strong signal and clear correspondence of spectral features on both substrates, Raman spectra of FLG on copper provide a reliable screening method to assess graphene quality.

Since graphene needs to fully cover the SFB lens, SEM provides a useful tool to verify

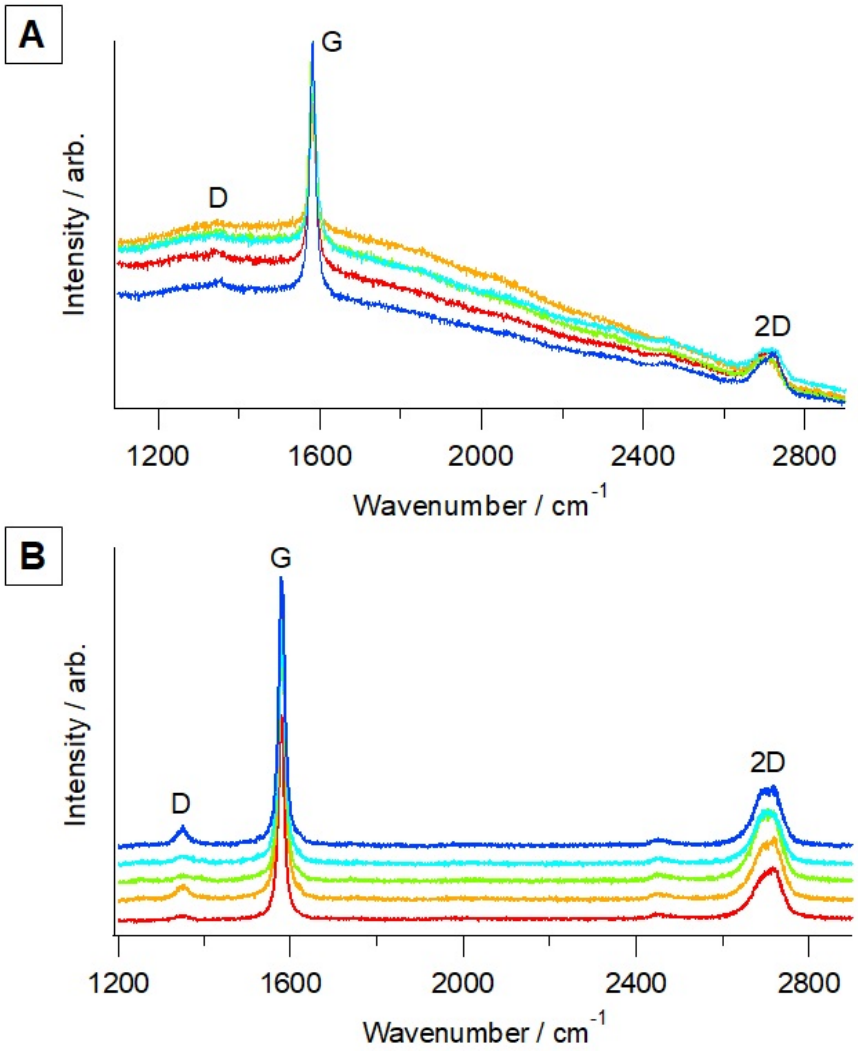


Figure 2.4: *Raman spectra of FLG: (A) taken at 5 different locations on the copper growth substrate; (B) taken at 5 different locations after transfer to SiO_2/Si. The letters D, G, and 2D denote the graphene's characteristic Raman bands.*

coverage on the Cu growth substrate. It also shows that the film is very heterogeneous in thickness. This is caused by a combination of factors, mainly surface roughness and synthesis gas composition. The rough surface enables high density nucleation of graphene crystals (indeed on smoother Cu foils surface coverage is lower and larger areas of SLG sit between islands of FLG). Second, the low H_2:Me partial pressure ratio (relatively high amount of CH_4) causes saturation of the Cu surface with C-species, resulting in rapid growth (full coverage is achieved in $\leq$ 45 min) and nucleation of secondary layers on top or underneath the first graphene nucleus.

Secondary nuclei imply heterogeneity of the gSFB lens surface which would be expected to strongly influence SFB experiments. For example, if the secondary (smaller) graphenes sit on top of a primary continuous layer, this exposes many step edges – higher energy sites liable to peeling or adsorption [68, 69]. For low pressure CVD growth of graphene on Cu, Raman spectroscopy and C-isotope labeling show secondary nucleation either underneath [70, 71] or on top [34] of the first graphene crystal. However, the secondary graphene layers in the latter study are of much lower crystallinity, i.e. having no well-defined shape, than in the other studies. For atmospheric pressure CVD secondary layers on top and bottom have been observed using phase contrast AFM [38]. Secondary nucleation of graphene layers in these studies occurs almost exclusively in the center of the first graphene crystal. Here, either the layers nucleate simultaneously, or nucleate after diffusion of C-species underneath the first layer [72].

For the FLG grown for the work presented in this thesis, it is likely that a significant portion of the secondary layers form underneath the first. This may be problematic for SFB-experiments, since during the transfer (described in Chapter 3) the graphene is oriented "upside down" with respect to its orientation on the Cu growth substrate. Further, the thickness inhomogeneity of the FLG also presents optical inhomogeneities that influence the accuracy with which the interferometric data obtained in SFB-experiments can be interpreted. As such, it is advantageous to use SLG for SFB-experiments.

Due to graphene's impermeability to gasses [67], heating the graphene-covered copper growth substrate causes oxidation of copper areas not covered with graphene. This provides an efficient measure of surface coverage when used in combination with optical microscopy (see figure 2.5). Graphene (SLG or FLG) used in SFB experiments was therefore analyzed as follows: foils were always heated (200 °C for 2 minutes) to verify the coverage of graphene on the surface using OM; Raman spectroscopy was performed

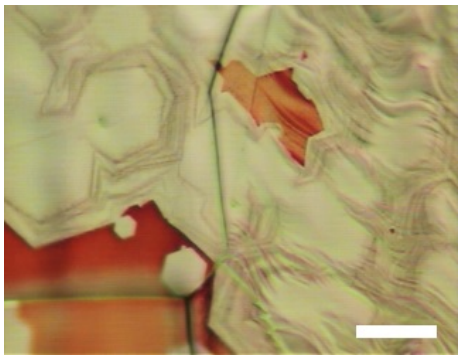


Figure 2.5: *Optical microscope image of few layer graphene partially covering the copper growth substrate. The (oxidized) copper is visible in orange, whereas the graphene covered areas in the image look white. The characteristic hexagonal shape of the graphene is visible. Also visible in the image are copper grain boundaries, steps and the outline of FLG layers. Scale bar is 30 μm.*

as quality control to verify defect density; SEM was performed only occasionally to verify the observations made using OM.

2.3.2 Single Layer Graphene

The original procedure for SLG growth was developed by Vitaliy Babenko in the group of Prof. Nicole Grobert. I assisted in developing the cleaning procedure.

Film cleaning was performed using IPA, followed by electropolishing using the EP2 recipe listed in table 2.1. SLG growth was performed in a quartz tube with an inner diameter of 100 mm on foils of 40 x 100 mm^2 placed on a fused SiO_2 or Al_2O_3 plate. Growth conditions are listed in table 2.6. The partial pressure of Me was increased slowly during the growth stage as this was found to be beneficial for CVD growth of graphene on large substrates [73].

Figure 2.6 shows SEM images of SLG on the Cu growth substrate. The contrast indicates no FLG was formed during the growth process. As graphene crystals nucleate and grow, they eventually coalesce forming a continuous film. By halting the growth prior to coalescence, the average SLG grain size can be estimated. Figure 2.6-A show the SLG crystal size is $\sim$ 50 - 100 μm. If the Cu-foil is fully covered with SLG, no contrast (other

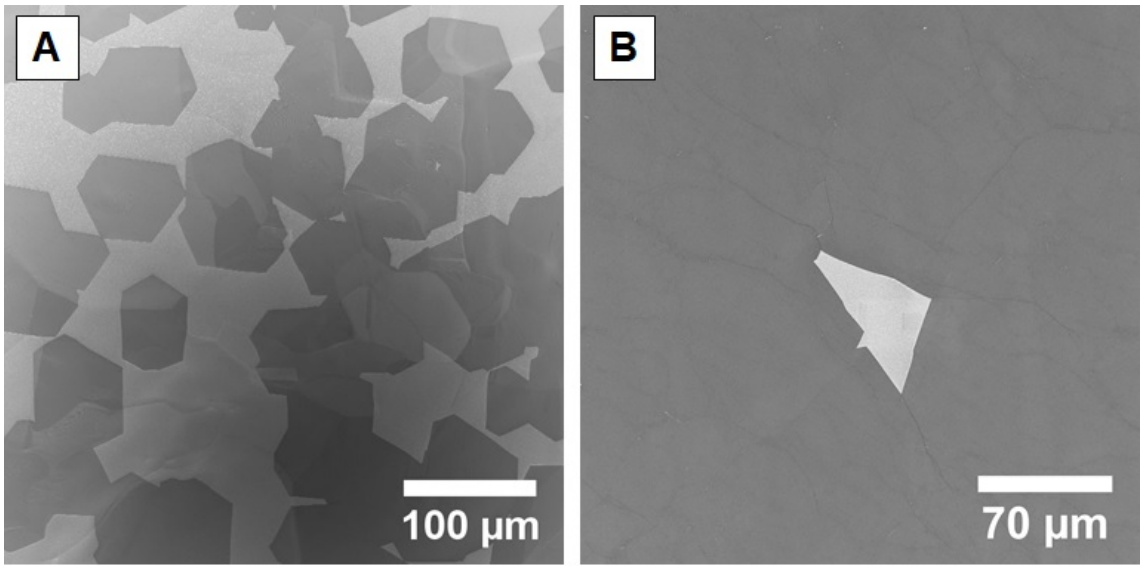


Figure 2.6: *SEM images of SLG: (A) Image of graphene crystals on Cu foil when growth was halted prior to the crystals coalescing to form a full film. The average crystal size is 50 - 100 µm. The grains of the underlying copper growth substrate are also visible; (B) Image showing a small hole in the graphene film at the end of a full graphene synthesis. The homogeneous contrast is indicative of SLG. Wrinkles are visible as dark lines.*

than wrinkles and the underlying Cu grains) can be observed. Figure 2.6-B shows a SEM image of such a film, with a small opening showing the underlying Cu for reference.

After using SEM and OM (after heating) to verify the Cu foil was fully covered with graphene, the graphene was transfered to Si/SiO_2 (see chapter 3 for more details on the transfer procedure) and a Raman spectrum was recorded to further characterize the SLG. This transfer was necessary, since on Cu the background signal is too high to obtain a good Raman signal. The I(G)/I(2D) ratio, I(D)/I(G) ratio and FWHM of the 2D peak

Table 2.6: SLG growth conditions.

		Gas flow (sccm)			
T(°C)	**t(min)**	**Ar**	**Me/Ar**	**H_2/Ar**	**Step**
RT	10	500			Chamber purge after sample loading
1060	60	500			Annealing of copper foil
1060	30		20	500	Graphene growth
1060	30		20.8	500	Graphene growth
1060	30		21.6	500	Graphene growth
1060	30		22.4	500	Graphene growth
1060	30		23.2	500	Graphene growth
1060	30		25	500	Graphene growth
RT	10			500	Sample cooling
RT	10	500			Chamber purge before sample removal

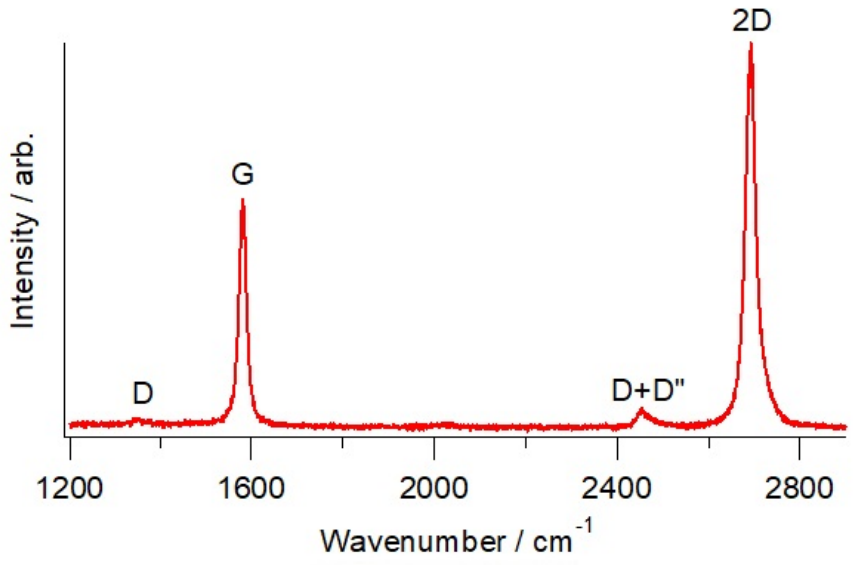


Figure 2.7: *Example Raman spectrum of SLG prepared using the procedure outlined in section 2.3.2: The I(G)/I(2D) ratio, I(D)/I(G) ratio and FWHM of the 2D peak (26 cm^{-1}) are indicative of high quality SLG. The shape of the low intensity D+D" band further indicates the presence of SLG.*

(26 cm^{-1} using a Lorentzian fit) in the Raman spectrum (Figure 2.7) are indicative of high quality SLG. The shape of the D+D" band provides further evidence for the presence of SLG [62].

Compared to FLG, the SLG film consists of much larger graphene crystals (grains). The larger grain size and absence of multi-layer graphene in the SLG samples arises mainly from reduced substrate roughness (electropolishing rather than AcH treatment) and the highly reduced Me partial pressure (i.e. H_2/Me = 65 and 2250 for FLG and SLG respectively). The absence of bi- multi-layers and a lower number of grain boundaries contribute to a much more homogeneous graphene film, which was expected to be advantageous for subsequent gSFB-experiments.

2.3.3 Liquid Copper

The growth of graphene on liquid Cu was briefly investigated, motivated by the reported reduction in number of contamination particles underneath the graphene on the Cu surface [74]. Cu foil and W foil were separately cleaned using IPA and AcH, dried with N_2. The

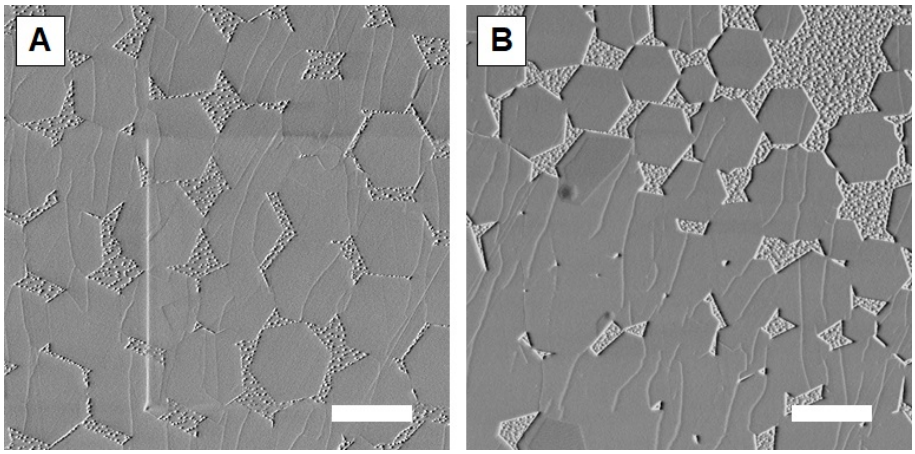


Figure 2.8: *SEM image of graphene grown on liquid Cu according to the procedure described in section 2.3.3. Individual graphene crystals are distinguishable due to their hexagonal shape. Wrinkles and the underlying Cu surface are visible as well. Scale bar is 10 µm.*

growth was performed in a 25 mm quartz tube in which the Cu foil was placed on top the W foil. Growth conditions are listed in table 2.7.

Table 2.7: Growth conditions for CVD growth of graphene on liquid copper.

		Gas flow (sccm)			
T(°C)	**t(min)**	**Ar**	**Me**	**H_2**	**Step**
RT	10	500			Chamber purge after sample loading
1100	30			300	Annealing of copper foil
1100	45		4.5	300	Graphene growth
RT	10		4.5	300	Sample cooling
RT	10	500			Chamber purge before sample removal

Figure 2.8 shows SEM images of graphene grown on liquid Cu. The high mobility of the Cu surface and high density of small graphene crystals can induce alignment between the graphenes (Figure 2.8-A) [49], but this is highly dependent on local growth conditions (Figure 2.8-B). The formation of "12-pointed" graphene flakes visible in Figure 2.8-B results from such locally different diffusion conditions [75].

Graphene growth on liquid copper allows for fast production of SLG and produces very smooth copper surfaces (advantageous in later steps of fabrication of graphene-covered gSFB lenses, see Chapter 3). However, growth on liquid copper requires the use of a supporting W substrate. The solidification of the Cu and differences in thermal expansion coefficient between Cu and W induce significant strain across the Cu/W stack, making the

substrates very brittle. This makes handling difficult and prohibits the growth of graphene on larger Cu/W substrates (although this could potentially be reduced by using a thin film of evaporated Cu, rather than a 25 μm foil). Further, the transfer of FLG/SLG was performed by etching the Cu substrate. The presence of the W complicated this process. Due to the difficulty in handling the substrates and transferring the graphene, no graphene grown using liquid Cu was used for gSFB experiments.

2.3.4 Expanding Single Layer Graphene Crystals to mm-Dimensions

In the previous section it was shown that large area samples of SLG can be synthesized as required for SFB experiments. However, due to the size of the individual grains it is highly likely that a number of grain boundaries exist within the contact area during a gSFB experiment. It would thus be desirable to increase the size of the individual crystals comprising the graphene film as this increases homogeneity and may increase mechanical strength [76]. Further, having a single grain (crystal) in the area of closest approach inside the gSFB may be important as it templates the molecular structure of the liquid of interest [77, 78].

I developed the procedure for growing mmSLG as an extension of the regular SLG growth procedure. As outlined in section 2.1.3, increasing the average grain size requires a reduction in nucleation density whilst preventing the formation of secondary graphene crystals. In order to achieve this, the Cu foils were treated prior to the CVD growth graphene as follows [37, 50].

Cu foils were degreased with IPA, then etched according to EP2, rinsed with H_2O and EtOH, dried with N_2 and oxidized using different oxidative treatments: Oxidation on a hotplate in air (inside a LFH) at $T_{plate} = 200\,^{\circ}C$; oxidation at $T_{plate} = 100\,^{\circ}C$ in a solution of hydrogen peroxide [50]; or oxidation inside the quartz tube using residual air (i.e. after

flushing the tube with Ar for 5 min.) at $\sim 1060\,^{\circ}C$.

Table 2.8: mmSLG growth conditions.

		Gas flow (sccm)			
T(°C)	**t(min)**	**Ar**	**Me/Ar**	**H_2/Ar**	**Step**
RT	5	500			Chamber purge after sample loading
1060	60	500			Annealing of copper foil
1060	30		20	500	Graphene growth
1060	30		20.8	500	Graphene growth
1060	30		21.6	500	Graphene growth
1060	30		22.4	500	Graphene growth
1060	30		23.2	500	Graphene growth
1060	30		25	500	Graphene growth
1060	60		25.5	500	Graphene growth
1060	60		26	500	Graphene growth
1060	60		26.5	500	Graphene growth
RT	10			500	Sample cooling
RT	10	500			Chamber purge before sample removal

Different growth conditions were tested as well. Two parameters were investigated: (1) The effect of the partial pressure of the methane/argon mixture throughout the synthesis; (2) The effect of diluting the synthesis gas mixture at the start of the synthesis by increasing the amount of argon (providing an argon "pulse") [37]. The growth was performed in 25 mm and 100 mm diameter quartz tubes. Growth parameters during the investigation were similar to those used for SLG mentioned in section 2.3.2. Final growth parameters (40 x 100 mm^2 Cu foils, using a 100 mm diameter quartz tube) are listed in Table 2.8.

Figure 2.9-A,B shows optical images of a graphene covered foil for which the graphene growth was stopped after 2h. The Cu foils were oxidized in air prior to the synthesis. The diameter of individual graphene crystals has increased by an order of magnitude compared to SLG growth performed without oxidation (see Figure 2.6), with grain sizes reaching 1 - 2 mm.

Figure 2.9-C shows a Raman spectrum of mmSLG transfered to SiO_2/Si. The I(G)/I(2D)

ratio, I(D)/I(G) ratio and FWHM of the 2D peak (27 cm^{-1} using a Lorentzian fit) are indicative of high quality graphene.

Figure 2.9-D shows an SEM-image of an exceptionally large graphene crystal of ∼5 mm in diameter, grown using the conditions given in table 2.8. It also shows the presence of much smaller bi-layer regions.

No significant difference was found between either the use of different oxidation methods or an Ar pulse. However, it was found that the synthesis was difficult to re-produce. Figure 2.9-F and 2.9-G, show two graphene-covered Cu foils produced using (apparently) the same foil pre-treatment and synthesis conditions. Inspection of different Cu foils after oxidation (either in air or H_2O_2) showed significant differences in color between the foils, despite originating from the same batch (Figure 2.9-E). Since this color arises from the reflection and interference of light at the Cu/CuO_x interface, it provides an estimate to the extend of oxidation of the foils. Therefore, difference in color indicates that between the Cu foils, the uptake of O_2 is quite different.

Due to the poor reproducibility of the oxidation step, a different approach was taken. Rather than oxidizing the foils at low temperature, the foils were oxidized at the growth temperature using residual O_2 present in the quartz tube after loading the sample. Due to the high temperatures, diffusion of O_2 in the Cu foils is likely to be more uniform (i.e. less dependent on surface grain orientation or the presence of grain boundaries). Using this approach, production of graphene films with grains of ∼1 mm could be reproducibly performed.

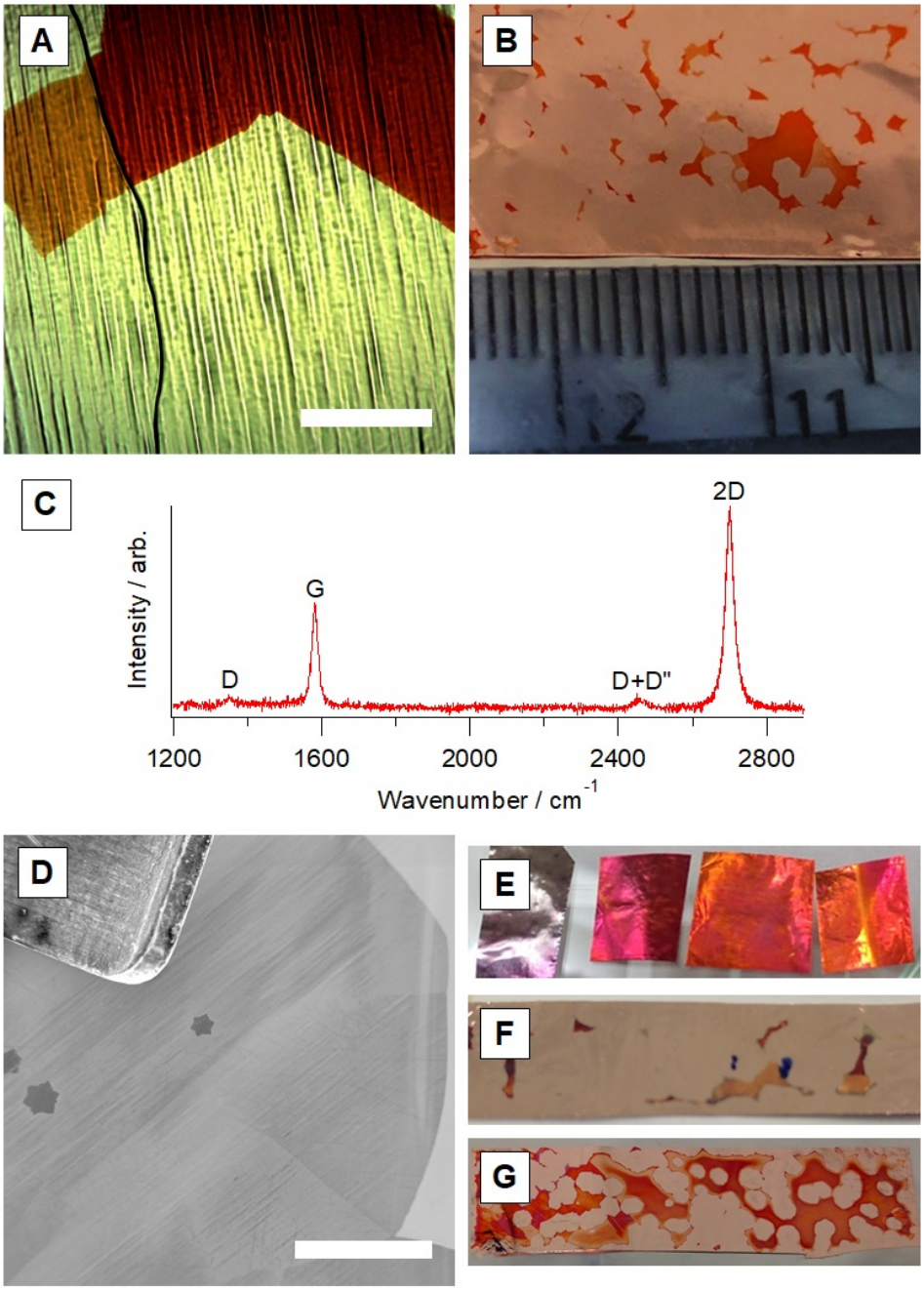


Figure 2.9: *Characterisation of mm-size SLG and optical images of oxidized Cu foils: (A) OM image of graphene-covered Cu foil after post-synthesis oxidation. The shape of the graphene (yellow) can be distinguished from the underlying Cu (orange, red). Two different Cu grains and a grain boundary are visible. Scale bar is 0.5 mm. (B) Photograph of same foil next to a ruler. The divisions on the ruler correspond to 1 mm. (C) Raman spectrum of mmSLG: The I(G)/I(2D) ratio, I(D)/I(G) ratio and FWHM of the 2D peak (27 cm^{-1}) are indicative of high quality graphene. (D) SEM image of 5 mm diameter graphene crystal. Three small bilayer regions are visible as darker stars. The sample holder clip is visible in the top left corner. Scale bar is 1 mm. (E) Photograph of different Cu foils oxidized using the same conditions. The width of the foils/strips is ∼ 1.5 cm. (F,G) Photograph of graphene-covered Cu foils after post-synthesis oxidation. Both samples were grown according to the same protocol.*

2.3.5 Targeted removal of copper foil surface impurities for improved synthesis of CVD graphene

This section describes results from a study performed together with Dr. Adrian Murdock on the origin and removal of contamination particles from the graphene covered Cu foils. In view of the scope of the thesis, this section provides only a brief summary.

The measurement of small surface forces across liquids, such as those arising from repulsion between electrochemical double-layers or from the interfacial structure of the liquid, require the use of clean, smooth surfaces. These must be free of asperities, such as nanoparticles, which may dominate forces measured during an SFB experiment [79]. In SEM-images of graphene grown on Cu foil, such particles are often observed (see Figure 2.3). Since the graphene-covered Cu foil is starting point for the fabrication of the surfaces used inside the gSFB, it is important to minimize the presence of these particulates.

Contaminant particles have been strongly associated with growth dynamics of graphene. They have been found at the same location as the center of graphene crystals and have thus been proposed to serve as nucleation centers [80, 81, 82]. It has been suggested they form on top of the graphene after the formation of graphene [74], or deposit due to high temperature reactions of sublimated Cu with the quartz tube [83]. An *in situ* study using environmental SEM has indicated that contamination particles precipitate during heating of the Cu foil [84]. Various particle compositions have been reported, such as: Cu/CuO_x [82]; Si, Ca, Ru, Pt, Ce [85]; Si, Fe, Al, Ca, O, C [74]; or Si [84, 83]. The presence of contamination particles can be reduced or avoided using high H_2 (low Me) partial pressure or by growing graphene on liquid Cu [74].

Figure 2.10 shows SEM images of graphene grown using the conditions listed for FLG with a shortened growth period (30 min) on Cu foils (same purity/supplier/batch) cleaned using different treatments. It is clear that on foils that have not been cleaned prior to

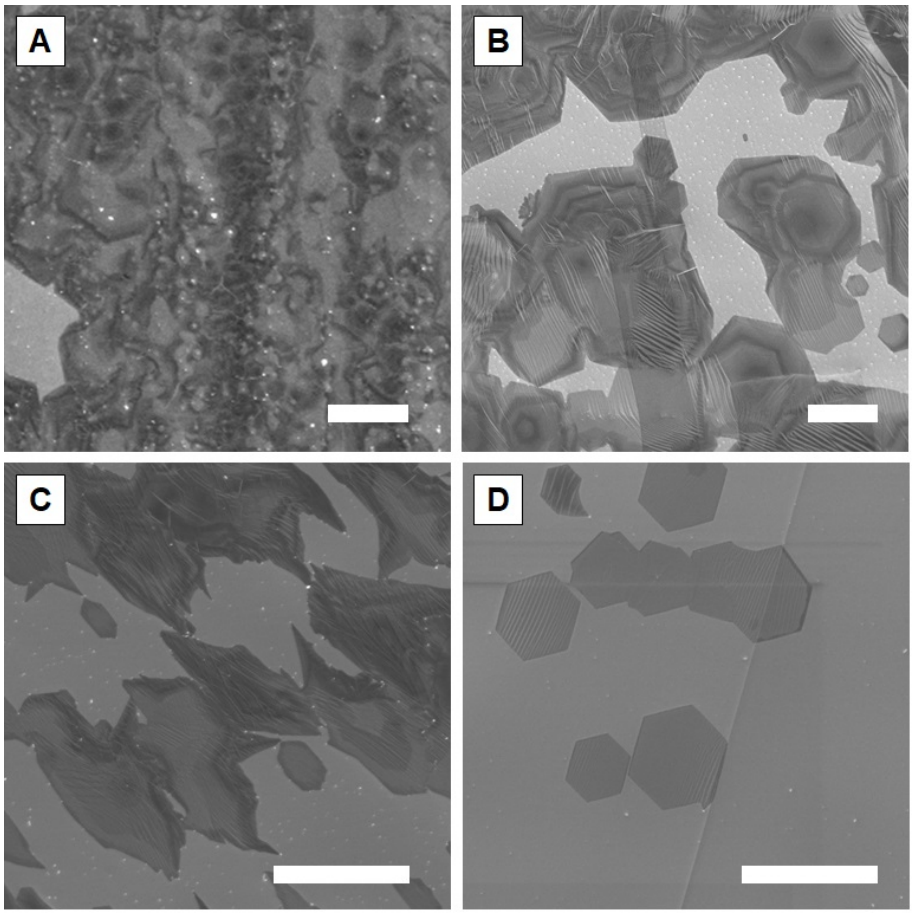


Figure 2.10: *SEM-images showing the effect of different pre-synthesis Cu foil treatments on the prevalence of particulate contamination: (A) No treatment. (B) Cleaning with AcH. (C) Cleaning with HNO_3. (D) Cleaning with HNO_3 and 2M KOH. Scale bars all 10 μm.*

performing the synthesis, a large number of particulates covers the surface (Figure 2.10-A). The number of contamination particles is significantly reduced when performing the synthesis after cleaning in AcH (Figure 2.10-B). Cleaning the surface via etching in HNO_3 (Figure 2.10-C) (as suggeted by Kim et al. [85]) or HNO_3 followed by 2M KOH (Figure 2.10-D) reduces the presence of particulates even further. Figure 2.10-C also provides an example of the effect some contamination particles can have on the growth of graphene, in which graphene growth seems to be accelerated in the direction of the contamination particles (although this is a localized phenomenon not found across the entire foil).

We tested Cu foils from different suppliers and different (bulk) purities. We found no significant differences between the level of contaminants at the surface and found contamination particles to consists mainly of C, O, Ca, Si and Al [46]. We therefore tested

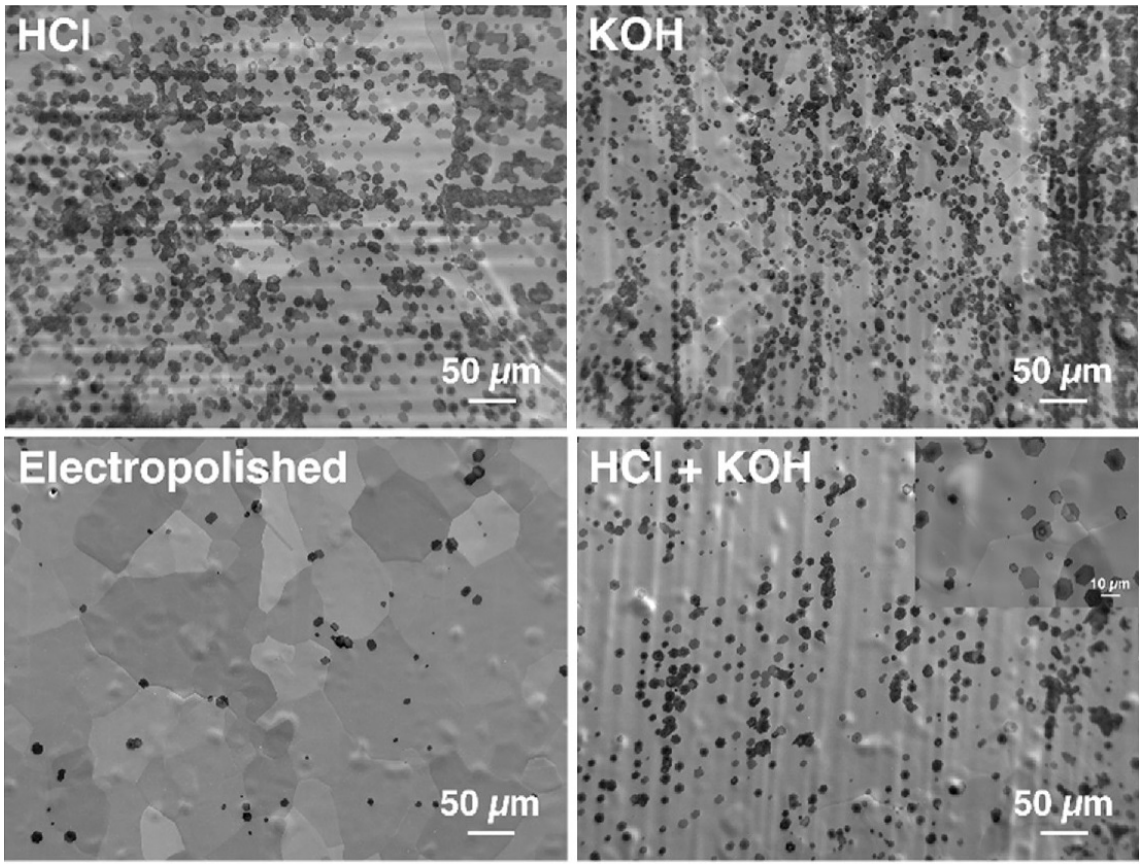


Figure 2.11: *SEM images of graphene grown on Cu foils (same purity, supplier and batch), treated with different methods: 2M HCl; 2M KOH; 2M HCl, followed by 2M KOH; Electropolished according to EP1.* Adapted from A.T. Murdock, C.D. van Engers *et al.*, Carbon 2017, 122, 207-216 [46].

cleaning approaches that specifically target the listed impurities and developed an economical (i.e. aimed at minimizing the loss of Cu whilst still being effective and simple) cleaning procedure to specifically target the impurities found. KOH is known to etch aluminum and silicon oxides, whilst HCl is known to etch aluminum and calcium oxides, however, neither HCl nor KOH etch Cu. This is advantageous with respect to etching with HNO_3 [85] or electropolishing [42, 41] since it prevents loss of Cu. Since a reduction in the presence of contamination particles occurs concomitant with a reduction in nucleation density (see also Figure 2.10), the nucleation density was used as a qualitative probe to assess remaining particulate contamination.

Figure 2.11 shows SEM images of graphene on different Cu foils (same purity/supplier/batch) treated with the different cleaning methods (2M HCl, 2M KOH, 2M HCl followed by 2M

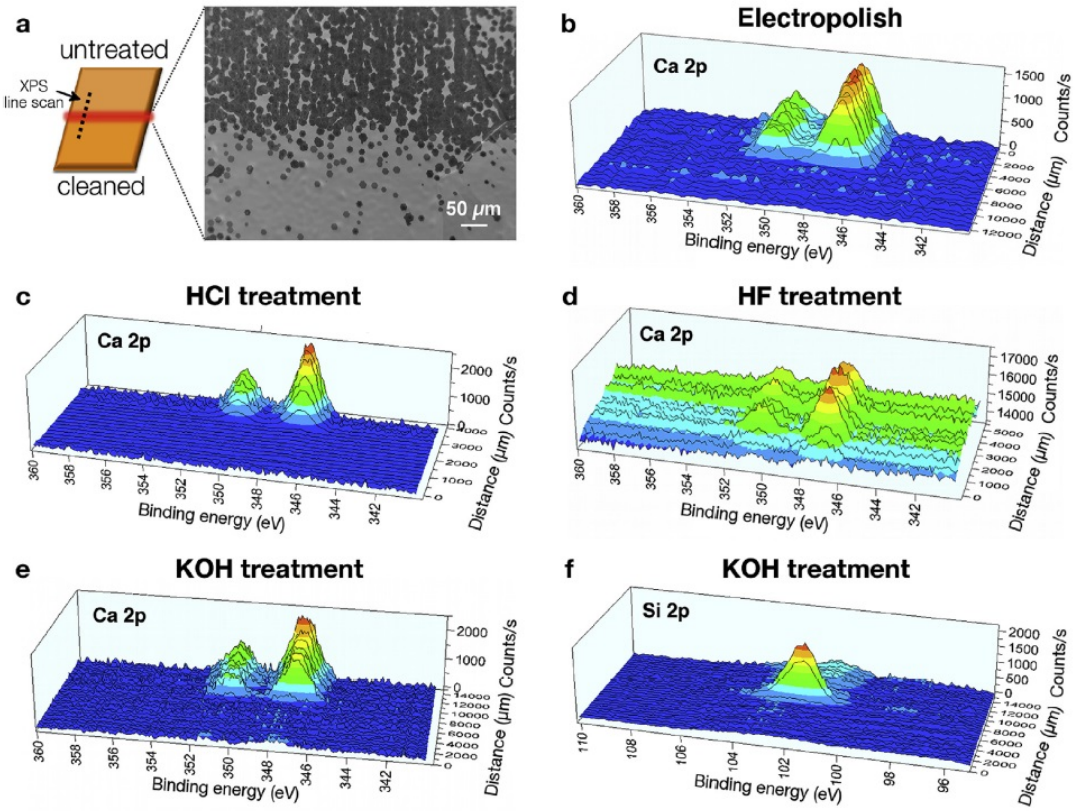


Figure 2.12: *Effect of targeted chemical treatments on concentration of contamination particles on Cu foils. (a) Schematic of Cu foil with untreated, cleaned, and boundary region (red line) labelled, alongside SEM demonstrating variation of CVD growth of graphene over such an electropolished boundary. (b) Detailed XPS Ca 2p line scan across electropolished boundary. (c) Detailed XPS Ca 2p line scan across HCl treatment boundary. (d) Detailed XPS Ca 2p line scan across HF treatment boundary. (e) Detailed XPS Ca 2p line scan over KOH treatment boundary. (f) Detailed XPS Si 2p line scan over KOH treatment boundary.* Adapted from A.T. Murdock, C.D. van Engers *et al.*, Carbon 2017, 122, 207-216 [46].

KOH respectively), grown using the conditions listed for FLG with a shortened growth period (30 min). A foil electropolished using EP1 is shown for reference. Treatment of the Cu foils by immersion in 2M HCl or 2M KOH results in a reduction of the nucleation density of the graphene crystals. This is further reduced by using HCl, followed by KOH. Cleaning using EP1 shows further reduction of nucleation density. This arises from a combination of the removal of the surface layer (removing surface contaminants), and smoothing of the surface (lowering surface roughness).

XPS-line scans were performed on foils that were only partly immersed in cleaning solution (Figure 2.12). The resulting XPS-spectra confirm the effectiveness of the treat-

ments in removing the targeted impurities [46]. It further confirms that the contamination particles precipitate from the (removable/treatable) surface layer and do not reflect the purity of the bulk Cu foil.

The Cu foils used for the growth of FLG, SLG and mmSLG used for gSFB, were treated using AcH, HNO_3 (FLG) and EP2 (SLG, mmSLG) respectively. The removal of a surface layer and/or use of a high H_2 partial pressure reduces the number of contamination particles on the surface (Figure 2.3, 2.6 and 2.9) [85, 74, 46]. This corroborates with observations made on the gSFB lens surface (see Chapter 3, Figure 3.12 and 3.14) and suggests that the cleaning treatments and/or growth conditions are appropriate for growing graphene for use in the gSFB.

Chapter 3

Graphene Transfer and Fabrication of Graphene SFB Lenses

The method for fabricating smooth graphene coated lenses for gSFB experiments was proposed in 2013, through a collaboration between Dr. Nico Cousens (Department of Chemistry) and Dr. Jude Britton (Department of Materials). The work was published in proof-of-principle form in 2014 [86]. Throughout almost the entire duration of this thesis work, the procedure has been modified and improved upon to enable contamination free gSFB experiments on smooth surfaces, for which the interferometric data can be readily analyzed. The schematic in Figure 3.1 gives an overview of the final procedure.

The gSFB lens fabrication method can divided into three stages (Figure 3.1). Accordingly, the different sections within this chapter correspond to the these different stages. The first section, 3.1 Polymer-Assisted Graphene Transfer, describes transferring the graphene from the Cu growth substrate onto a thin, freshly cleaved single crystal

of muscovite mica. An overview of the steps involved in this stage of the fabrication is given in the red panel in Figure 3.1.

To be able to analyze the interferometric data obtained in experiment, the graphene-supporting epoxy layer needs to be of uniform thickness. Different approaches to obtaining such a layer are discussed in section 3.2 Fabrication of epoxy layers of uniform thickness. The final procedure is shown schematically in the green panel in Figure 3.1.

The final section of this chapter, 3.3 Template stripping of graphene from mica, discusses factors of import to the final "template stripping" step, in which the mica is separated from the graphene/epoxy/lens assembly (blue panel in Figure 3.1).

The measurement of surface forces requires clean surfaces, free of particulate or molecular contaminants. To verify that none of the fabrication steps or system components introduced any molecular contamination on the graphenes, surface energy measurements were performed. These give a qualitative estimate of cleanliness, since contaminants adsorb to lower the surface free energy [87]. The measurement of surface (interfacial) energy on graphene will be extensively discussed in Chapter 5. However, measured values will be used for reference. A general description of clean procedures and practices can be found in Appendix A: Clean Handling & Practices.

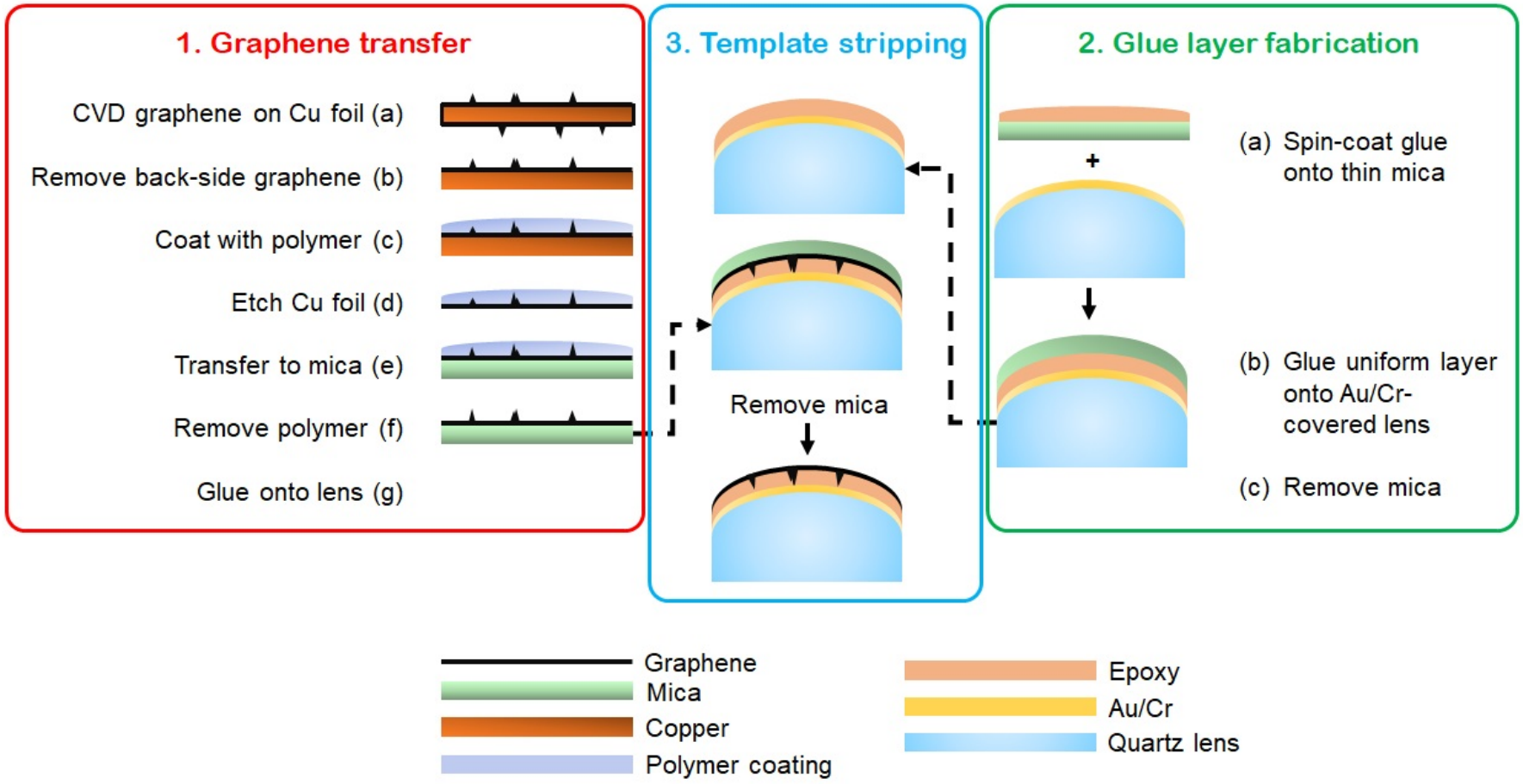


Figure 3.1: *Schematic showing different steps involved in the fabrication of gSFB lenses. The procedure can be divided into three separate stages: (1) graphene transfer (red panel); (2) glue layer fabrication (green panel); and (3) template stripping (blue panel). Stage 1 involves transfer of the graphene film from the copper growth substrate to a single crystalline piece of muscovite mica supported on a thick mica base sheet (not shown). Individual steps are highlighted with the letters a-g. The last step of stage 1 (g) involves gluing the mica/graphene stack onto a epoxy layer of uniform thickness fabricated in a separate set of steps (stage 2). In the final step of the entire procedure, during stage 3, the mica is carefully peeled away from the graphene/epoxy/lens assembly, exposing a clean and smooth graphene surface.*

3.1 Polymer-Assisted Graphene Transfer

3.1.1 Introduction

CVD on catalytic metal (Cu) foils can be used to grow uniform, high quality, large area graphene. This makes it an ideal method for producing graphene for gSFB. However, after growth the graphene remains attached to the Cu growth substrate. In order to be able to use graphene in applications, a transfer from the growth substrate is required.

Several strategies for transferring graphene from the Cu growth substrate have been proposed. The most prominent transfer method uses a solution cast polymer as intermediate substrate (between the Cu growth substrate and the target substrate, e.g. SiO_2 or mica) [88]. Other methods and their applicability to transfers for gSFB can be summarized as follows:

- Transfers using metal supports [89]. Not suitable due to need for aqueous etchants. Water causes lift-off of mica from the underlying base-sheet.
- Transfers using molecular supports that can be removed via sublimation [90, 91]. This could be a viable approach, but has not been tested. Concerns are the mechanical stability of the molecular film.
- "Direct" transfers that rely on statics [92] or pressure and heat [93, 94] to directly transfer the graphene onto a (flexible) target substrate. The handling steps involved are likely to cause contamination and/or mechanical damage to the mica template.
- Transfers using no support [95, 96]. Although promising, the graphene tends to break in absence of a supporting substrate.

For the work in this thesis, polymer-based transfers were used. Polymer-based transfer methods are the most applicable to gSFB and most widely investigated. Studies have mainly focused on the use of Poly(methyl methacrylate) (PMMA), a thermoplastic known

for its use in lithography, used in some of the first reports on the transfer of CVD graphene [27].

An overview of the general workflow of a polymer-based transfer is given in figure 3.2 and can be briefly described as follows: After growing the graphene on Cu and removing the backside graphene with O_2 plasma, the graphene is coated with polymer (step 1). The Cu is removed by etching and the graphene/polymer stack is rinsed to remove etchant (step 2). The stack is then placed onto the target substrate (step 3). This is generally done whilst wet, but may also be done after drying. The polymer/graphene/substrate stack is then heated to its softening point (glass transition temperature, T_g) to increase contact area (conformity) between the polymer/graphene and the substrate (step 4). Finally, the polymer is removed (step 5).

In transfer studies, graphene is often transfered to Si with a layer of thermally grown SiO_2. This substrate is chosen since the thermal oxide allows for visualization of the graphene layer due to optical interference [97, 98].

Optimizing Conformal Contact

The contact mechanics of placing a polymer-supported graphene film onto a hard substrate such as mica or SiO_2/Si is analogous to the case of placing a thin film onto a substrate (see Figure 3.2). The substrate is smooth and hard (non-compliant), and the film has finite roughness and flexibility. The roughness arises from the surface profile of the graphene-covered Cu growth substrate, the flexibility of the film arises from the film's thickness and elastic modulus. The latter depends on the polymer's molecular structure and chain length (although thermal history can be important as well) [99, 100]. When brought into contact the conformity by which the film covers the substrate is governed by the flexibility and roughness of the film, and the interfacial energy between the film and the substrate [101]. When the polymer film is dissolved, the parts of the graphene film that are not in

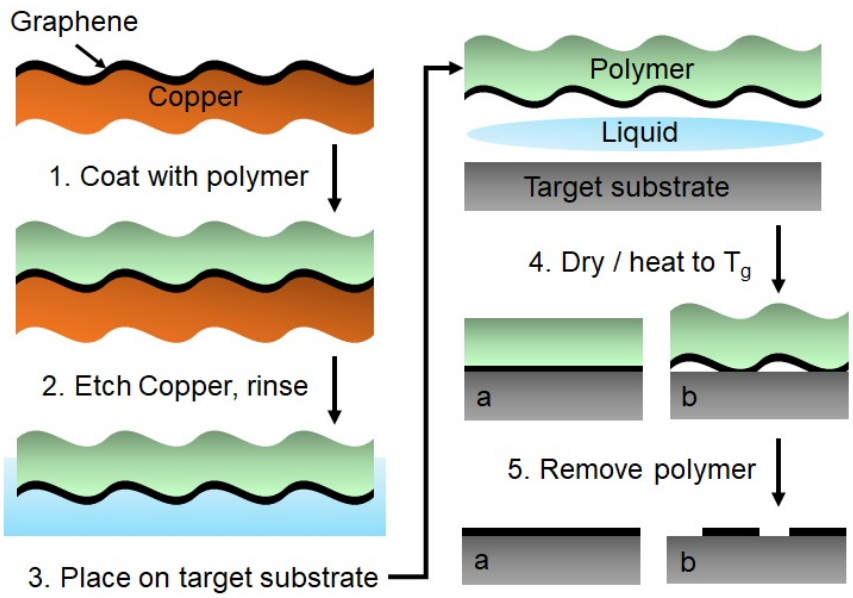


Figure 3.2: *Overview of general workflow for polymer-based transfers of graphene from a Cu growth substrate to a flat target substrate. In steps 4 and 5, situations a and b indicate the importance of optimizing conformal contact between the polymer-supported graphene film and the substrate. When the film is in not in full contact with the substrate (situation b), there will be holes in the graphene at locations where it was not in contact with the substrate.*

contact with the substrate will break, resulting in holes in the film (Figure 3.2 step 4,5-b). When the film is not flexible enough to conform to the substrate, its flexibility may be increased by heating to the polymer's T_g.

For studies on polymer-assisted transfers in the graphene community, the flexibility of the (PMMA) polymer support was increased by reducing its thickness, going from the use of dropcast films [27], to spincast films [102], to very thin spincast films with an additional secondary support [103]. If the polymer/graphene is placed directly from the rinsing solution onto the target substrate, conformity can be increased if the liquid completely wets the substrate (i.e. when the surface tension of the liquid is lower than the interfacial energy between the liquid and the substrate) [104]. After the polymer/graphene stack has been placed onto the substrate, conformity can be further increased by increasing flexibility of the polymer film by swelling of the polymer film [105] or heating the polymer above its T_g [106].

These developments occurred concomitantly with the realization that for the growth of SLG, it is beneficial for the Cu growth substrate to be as smooth as possible (see Section 2.1.3). This reduction in roughness has also led to increases in conformity and a reduction in damage to the graphene during the transfer. For transfer from/to rough substrates, the use of semi-crystalline rubbery polymers such as ethylene-vinyl acetate rather than hard, amorphous polymers such as PMMA has been suggested [107].

Minimizing polymer residue

The dissolution and removal of the polymer film from the graphene is not always complete. Since the presence of polymer residue (PMMA) may influence graphene's electronic properties [108], ensuring complete removal of the transfer-polymer has become a topic of its own. For gSFB, removal of the polymer films is important as well, as it affects the refractive index profile within the interferometer.

Polymer removal is governed by the properties of the polymer. These are intrinsic properties such as molecular structure (interfacial energy with graphene) and chain length, but also concern thermal history. For example, increasing chain length, thermal treatment and solvent choice (annealing to reduce residual solvent and relax the structure) have been shown to influence the dissolution rate of PMMA [109, 110, 111, 112, 113].

The removal of PMMA has been studied with respect to its application in lithography, but due to the desire to obtain PMMA-residue-free graphene, many of these parameters were revisited. It was found that using lower molecular weight PMMA resulted in more effective removal [114, 115]. The use of different solvents [108, 116, 117], and heating treatments after placement of the polymer-supported graphene on SiO_2/Si target substrate (i.e. solvent removal by annealing below T_g and increasing conformity by heating above T_g) were also reported to affect the removal of PMMA [106, 118, 119]. The removal of interfacial PMMA residues, present after dissolution of the bulk of the film with solvents,

using vacuum and thermal treatments was tested as well [108, 116]. Finally, polymers other than PMMA, such as polycarbonate (PC), were investigated and can be used to avoid polymer-residue [120].

3.1.2 Materials & Methods

Polymer-assisted transfer of graphene to flat substrates

Graphene was transfered from the Cu growth substrate to SiO_2/Si according to the following protocol (see also Figure 3.2) [27, 86, 103, 120]:

1. Removal of back-side graphene. The graphene was removed from one side of the Cu foil by either:

   A. Inductively couple plasma etching using O_2 (Oxford Instruments Plasmalab 80, 25 W, 1 minute, 100 mTorr, 80 sccm O_2). During etching the graphene-covered Cu growth substrate was placed on Al_2O_3 foil. The sides were covered with clean glass slides.

   B. Plasma etching (isotropic) using O_2 (Bio-Rad PT7125 Barrel, 160 W, 2 minutes, 0.18 mbar). Due to the isotropic nature of the plasma, the graphene-covered Cu growth substrate was spin-coated with PC (0.4 g PC / 10 ml $CHCl_3$ at 3000 rpm for 30 seconds) prior to, and after the etching step.

2. Polymer coating. The graphene-covered side of the Cu growth substrate was coated with polymer by either:

   A. Drop coating with PMMA (1 g PMMA / 5 ml Bz-Cl)

   B. Spin coating with PS (0.75 g PS / 10 ml Tol at 3000 rpm for 30 seconds)

   C. Spin coating with PC or PMMA (0.75 g PC / 10 ml $CHCl_3$ or 1 g PMMA / 10 ml $CHCl_3$ at 3000 rpm for 30 seconds)

D. Spin coating with PC (0.4 g PC / 10 ml $CHCl_3$ at 3000 rpm for 30 seconds)

Very thin films were supported by an additional PDMS stamp (D). The stamps were fabricated by mixing the 2-components of the PDMS, removing air bubbles under vacuum or by centrifugation, casting the solution into a clean PS petri dish and curing overnight at 80 °C. After curing the PDMS was cut into pieces, sonicated 3 times in heptane and dried overnight in vacuum [121].

3. Copper etching & rinsing. The Cu was etched by floating the foils on degassed 0.1 M APS (aq) or 0.1 M $FeCl_3$ (aq). Subsequently samples with a thick polymer layer or additional PDMS support were carefully picked up using a piranha-cleaned glass slide or PTFE foil and floated on water. The rinsing step was repeated three times.

4. Placement on target substrate. The samples were either scooped up with the target substrate (in the case of SiO_2/Si) or carefully placed onto the substrate (in the case of mica) with a thin film of water in between.

5. Annealing & heating to T_g. Samples were air dried and subsequently heated to $\geq$ T_g for 15 minutes (PMMA), 0 minutes (PS) or 2 minutes (PC).

6. Polymer removal. The polymer film was removed using either AcH (PMMA), Tol (PS) or $CHCl_3$ (PC), by submerging the film in solvent. The rinsing step was repeated three times.

Materials

Table 3.1 and 3.2 list the materials, supplier and chemicals used. Grade 1 muscovite mica (mica) was obtained from S&J Trading, Inc. (obtained as: ruby mica V-2/V-1 mixed ASTM Grade 1 Optical Grade).

Table 3.1: Liquids

Name	**Abbreviation**	**Supplier**	**Purity**
Ultrapure water	Water	Arium Pro Ultrapure	18.2 MΩ.cm, TOC <2 ppb
Chloroform*	$CHCl_3$	Sigma Aldrich	≥99.8%
Toluene*	Tol	Sigma Aldrich	≥99.5%
Acetic acid*	AcH	Sigma Aldrich	≥99%
2-Propanol*	IPA	Sigma Aldrich	ACS reagent ≥99.8%
Heptane	Heptane	Sigma Aldrich	≥99.8%
Chlorobenzene	Bz-Cl	Sigma Aldrich	≥99.5%

*Listed purity or similar used.

Table 3.2: Solids

Name	**Abbreviation**	**Supplier**	**Purity**
Poly(methyl methacrylate) average Mw ∼350,000	PMMA	Sigma Aldrich	Not listed
Polystyrene average Mw ∼200,000	PS	Sigma Aldrich	Not listed
Poly(Bisphenol A carbonate) average Mw ∼45,000	PC	Sigma Aldrich	Not listed
Sylgard® 184	PDMS stamp	Sigma Aldrich	Not listed
Ammonium Persulphate	APS	Sigma Aldrich	≥98%
Iron(III) chloride hexahydrate	$FeCl_3$	Sigma Aldrich	≥99%

Analysis

OM was performed using a Yenway CX40M metallurgical microscope. Atomic force microscopy was performed using a NanoScope MultiMode AFM operated in tapping mode (TM-AFM).

3.1.3 Results & Discussion

Figure 3.3 shows optical images of transfers of different graphenes to SiO_2/Si. Figures 3.3-A,B show a transfer of FLG from Cu growth substrates of similar roughness, using a drop cast film of PMMA (in A), and a spin cast PS film (in B). Due to the lack of flexibility the relatively thick PMMA film cannot fully conform to the substrate, resulting in large holes, whereas the thinner PS film is more flexible, resulting in a transfered graphene film

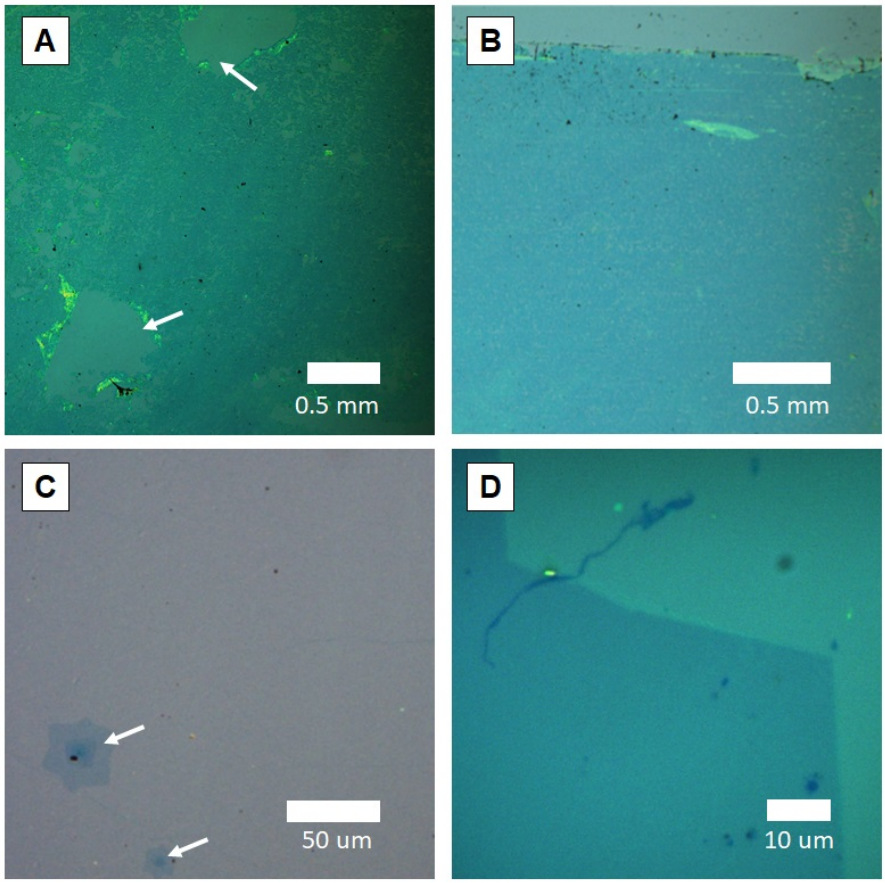


Figure 3.3: *Optical microscopy images of graphene transfered to SiO_2/Si using different polymer supports: (A) FLG transfered using a dropcast film of PMMA. The arrows indicate large holes, formed due to incomplete contact between the PMMA-supported graphene film and the SiO_2/Si target substrate. (B) FLG transferred using a spincast film of PS. No holes are visible. The underlying SiO_2/Si substrate is visible at the top of the image. (C) mmSLG transferred using a spin cast film of PC, supported by a PDMS stamp. The arrows indicate small islands of multi-layer graphene. (D) mmSLG transferred using a spin cast film of PC, supported by a PDMS stamp. The image shows a clear, clean edge of a graphene flake.*

free of holes. However, the PS could not be completely dissolved and left behind a visible residue (similar to the inset shown in Figure 3.4-C).

The graphene is turned upside-down during the transfer procedure for the fabrication of gSFB lenses (Figure 3.1). Due to this change in orientation the polymer is never in contact with the graphene side of interest, which is protected by the mica template [86]. Polymer residue does therefore not result in particulate or molecular contamination that may prevent measurement of surface forces. However, the presence of polymer residue

may influence the precise interpretation of interferometric data (see Chapter 4). It is thus desirable to be able to remove all remaining polymer residue.

Figure 3.3-C,D, shows optical images of a transfer of mmSLG performed using a spin-cast PC film supported by a PDMS stamp. The images show the PC-transfered mmSLG is free of damage and residues, giving well-defined interfaces between graphene and the SiO_2/Si substrate (3.3-D).

The use of the PMDS stamps was necessary due to the tendency of the thin PC film to either break or adhere to itself during handling. Although PDMS stamps offer mechanical support, their presence may contaminate the surface of the graphene covered gSFB lens due to leaching of unreacted components or oligomers [122, 121]. Using surface energy measurements (see Chapter 5), it was found that it was necessary to clean the stamps by ultra-sonication in heptane to remove these contaminants. Without this cleaning treatment, the use of PDMS stamps during transfer resulted in a substantial decrease in measured surface energy to 22±10 mJ/m^2 (rinsing the stamp in IPA was found insufficient, yielding 48±10 mJ/m^2).

Figure 3.4 shows TM-AFM height maps of mmSLG transfered to SiO_2/Si using spin-cast PC films supported by a PDMS stamp. The maps indicate the transfered graphene is smooth and free of polymer contamination. Wrinkles resulting from the mismatch between the Cu growth substrate and the graphene that develop during cooling form high protrusions of 20-30 nm (Figure 3.4-A). In addition, wrinkles that form due to the transfer process form a distinct pattern with protrusions of up to 5 nm (3.4-D,E). The underlying SiO_2/Si looks flat and featureless (Figure 3.4-B). When using Tol rather than $CHCl_3$ to remove the PC film, the surface shows a rough topography and a visible film is left behind even where the graphene is not present (Figure 3.4-C and inset), indicating the PC is not completely removed and showing the importance of choosing the right solvent for polymer removal.

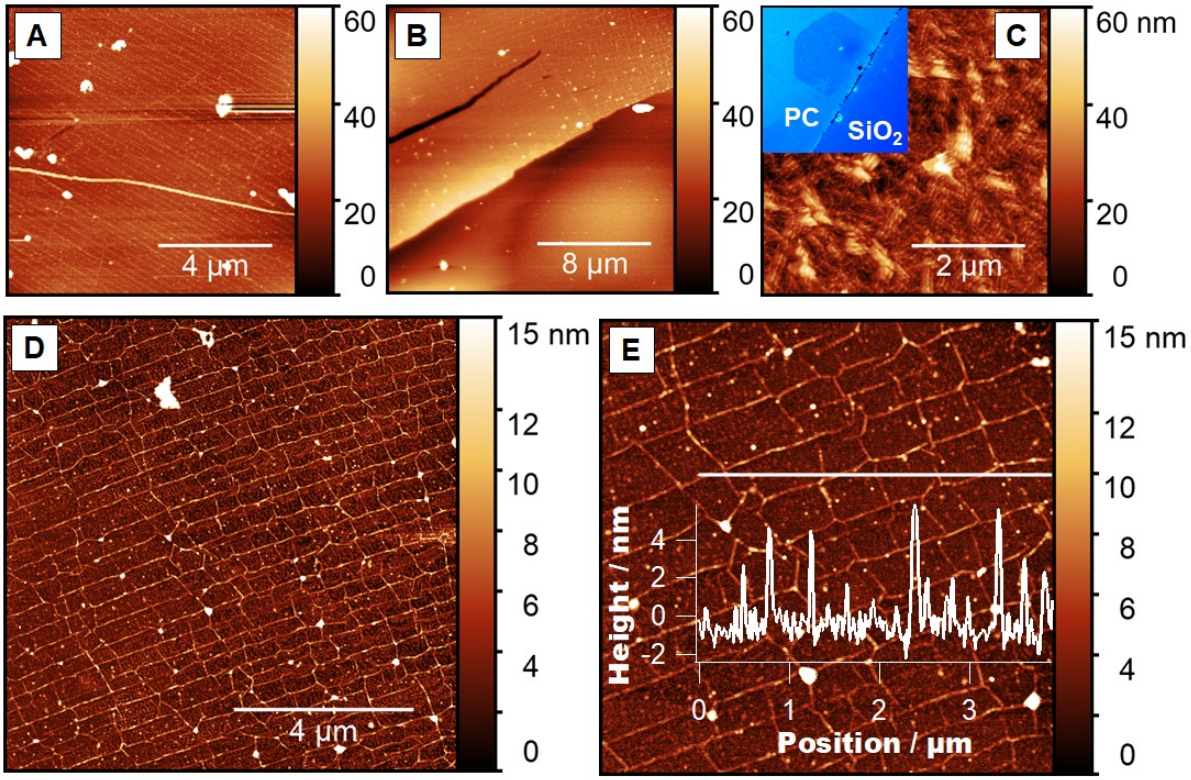


Figure 3.4: *TM-AFM height maps of mmSLG transfered to SiO_2/Si using spin-cast PC films supported by a PDMS stamp. (A) 10 x 10 μm^2 map showing a clean transfer with a prominent wrinkle with a height of 27 nm. Some particles are visible. (B) 20 x 20 μm^2 map showing a clear, clean edge between graphene and the underlying SiO_2/Si. A crack in the graphene is visible as dark stripe. Due the size of the image and the use of TM-AFM, the step-edge height does not correspond to the expected 0.34 nm. (C) 5 x 5 μm^2 Height map of transfer in which the PC-film was subjected to Tol rather than $CHCl_3$. The inset shows an optical image, in which the PC film is still visible on the underlying SiO_2/Si, even at locations where graphene is not present. (D) 10 x 10 μm^2 map showing mmSLG on SiO_2/Si. The transfer induces a pattern of wrinkles in the graphene. Small particles are visible. (E) 5 x 5 μm^2 map showing mmSLG on SiO_2/Si . The inset shows the line profile corresponding to the line in this image, indicating the wrinkles are 3-5 nm in height.*

3.2 Fabrication of epoxy layers of uniform thickness

3.2.1 Introduction

During the polymer-assisted transfer, the graphene is placed onto a thin mica sheet, supported by a thick mica plate. Subsequently the polymer film is removed, and the graphene/mica stack is glued onto a cylindrical quartz lens with an epoxy coating (Figure 3.1, panel 2). The epoxy serves both as a glue to keep the graphene in place, and as an optical spacer: the use of white light interferometry requires a minimal spacing between the mirrors equal or larger than the diffraction limit of the light used (in optical distance). The use of mica as a template imparts smoothness onto the graphene at the nanoscale [86]. However, due to the deformable nature of the epoxy resin, it does not ensure a smooth surface at the macroscale.

Figure 3.5-A shows a schematic of ideally fabricated gSFB lenses in cross-cylinder configuration. The graphene-supporting epoxy layer is of uniform thickness and the optical point of closest approach between the (Au) mirrors (yellow dashed line) is equal to the actual point of closest approach (solid black line). Figure 3.5-B shows the effect of having a (macroscopically) rough, corrugated graphene-supporting epoxy layer. The optical point of closest approach is no longer equal to the actual point of closest approach, and - in the case of very large oscillations in epoxy thickness - there are multiple points of contact (solid red).

The existence of a small offset between the optical and actual point of closest approach can be partially accounted for by detailed analysis of the interferometric data. However, in order to unambiguously interpret the data it is highly desirable to have a glue layer of uniform thickness. This chapter discusses several strategies for the fabrication of such surfaces. An extensive discussion of the optics inside the SFB can be found in Chapter 4.

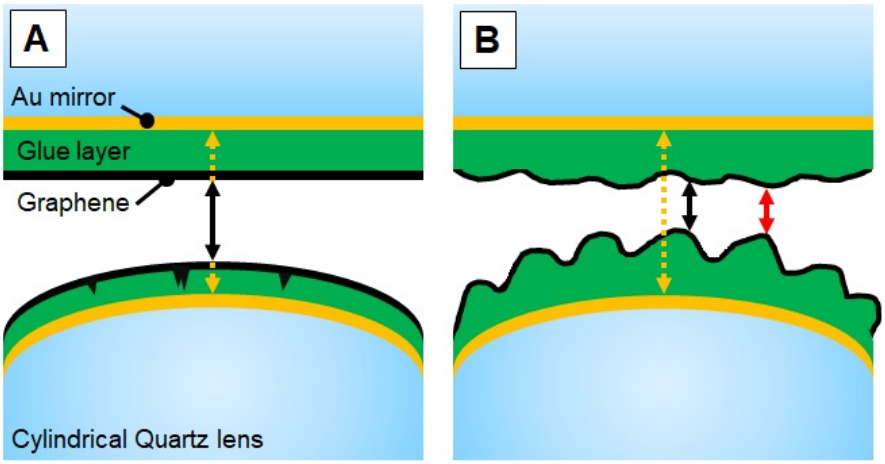


Figure 3.5: *Schematic showing the difference between having a graphene-supporting epoxy layer of uniform (A) and non-uniform (B) thickness in experimental, crossed cylinder configuration. The dashed yellow arrows indicates the optical point of closest approach. The black arrows indicate the actual point of closest approach. The red arrow indicates a second point of contact between the gSFB lenses.*

3.2.2 Materials & Methods

Various methods were used to fabricate glue layers. An overview is given in Figure 3.6.

Method 1: Drop-coating

EPON was drop cast from either $CHCl_3$, DCB or MIBK solution (0.2 g EPON / 6 mL solvent) (Figure 3.6-Method 1). After drop casting from $CHCl_3$, the samples were dried in air and heated to 180 °C, after which the mica/graphene stack was glued on top. They were then cooled to room temperature. For drop casting from MIBK or DCB, the samples were placed on a glass slide on top of a 1 cm high glass dish, on top of a hot plated heated to 70 °C (MIBK) or 100 °C (DCB) and covered with a large 8 cm high dish. Subsequently a drop of EPON/MIBK solution was placed on the lens. The solvent was then allowed to slowly evaporate for 30 min.

Method 2: Direct spin-casting

EpoThin or EPON was direcly spin cast onto the mirror-coated cylindrical SFB lens (Figure 3.6-Method 2). EpoThin was diluted with EtOH (1:2 v/v) and spin coated using a Laurel WS650 Mz-23NPP/LITE spin coater. The following spin cycle was used: accelerate at 100 rpm/s for 5 seconds, then accelerate to 3000 rpm at 300 rpm/s for 30 seconds. The spin coater was situated in ambient air. EPON was spin cast from acetone (1 g EPON / 3 ml acetone) at 3000 rpm for 30 seconds using a Osilla E441 spin coater. The spin coater was situated in a laminar flow hood.

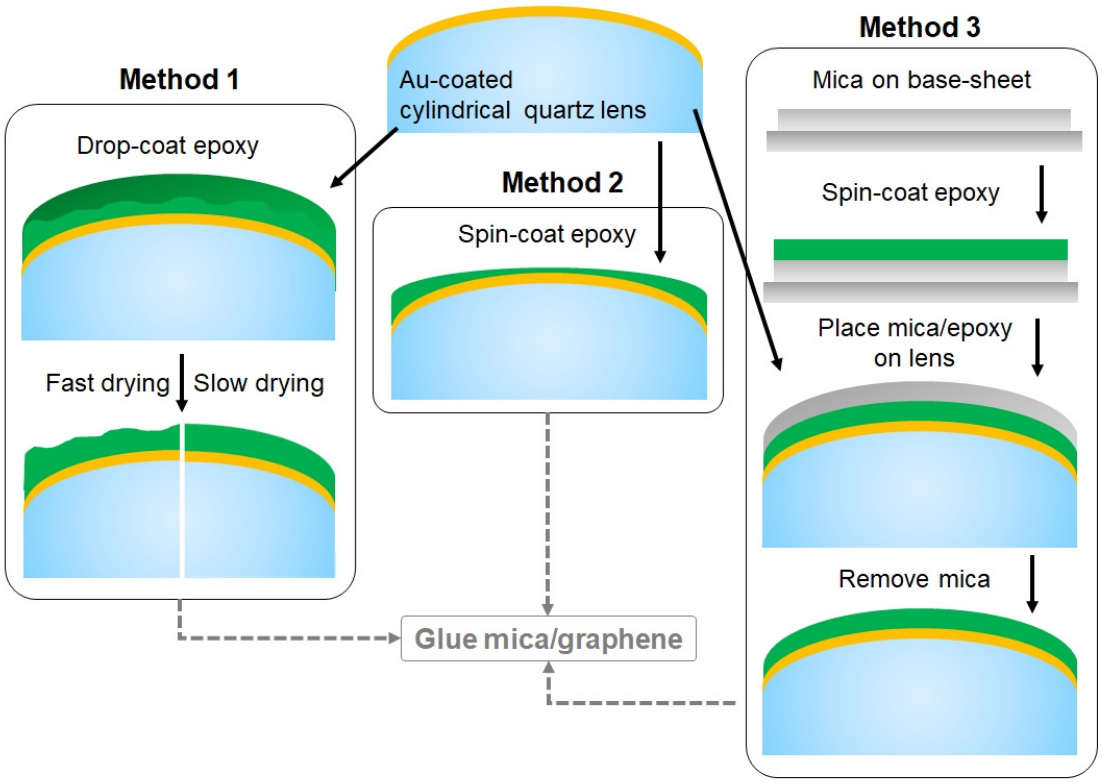


Figure 3.6: *Schematic showing three different methods for fabricating the epoxy layer on top of the mirror coated cylindrical quartz lenses. After fabrication of the epoxy layer, the graphene/mica stack was glued on top.*

Method 3: Indirect spin-casting

Indirect spin casting involves first forming a film by coating a planar substrate, and then transferring the film onto the cylindrical lens.

Silicon chips were cleaned with piranha solution, followed by sonication for 45 minutes at 60 °C in (100:20:8 v/v/v water:H_2O_2:NH_4OH). These treatments effectively remove organic contamination and particulates from the surface [123]. Mica was cleaved to obtain pieces with a thickness of $\sim$ 6 μm (flexible, but to be easily picked up from the silicon chip without damaging) having a single facet of $\geq$ 2 cm^2 (larger in each dimension than the 1 cm diameter cylindrical SFB lens) (Figure 3.6-Method 2). After cleaving, the mica was placed onto the silicon chip.

EPON was spin cast from acetone or EtAc (1 g EPON / 3.4 mL acetone or EtAc, 45 μL) at 3000 rpm for 30 seconds using a Osilla E441 spin coater. The spin coater was

situated in a laminar flow hood. The EPON/mica/silicon stack was then placed on a hotplate heated to 150 °C. Subsequently, the EPON/mica stack was carefully picked up and placed onto a gold-coated cylindrical SFB lens. After placement onto the lens, the EPON/mica folds over the lens, due to the flexibility of the mica and the capillary force from the EPON acting at the Au-EPON-mica interace. The mica/EPON/lens stack was cooled down and the mica was carefully peeled off in water.

Analysis

Analysis was performed using OM and by analysis of the interferometric data recording using the (g)SFB. OM was performed using a Brunel SP55D optical microscope in combination with a 25 mm diameter mounted red bandpass filter with a center wavelength of 650 nm and FWHM of 10 nm (Edmund Optics).

Materials

Grade 1 muscovite mica (mica) was obtained from S&J Trading, Inc. (obtained as: ruby mica V-2/V-1 mixed ASTM Grade 1 Optical Grade). Table 3.4 and 3.3 list the materials, supplier and chemicals used.

Table 3.3: Solids

Name	**Abbreviation**	**Supplier**
EpoThin 2 Resin	EpoThin	Buehler
Polystyrene, average Mw ∼200,000	PS	Sigma Aldrich
EPON™ Resin 1004F	EPON	

Table 3.4: Liquids

Name	**Abbreviation**	**Supplier**	**Purity**
Ultrapure water	Water	Arium Pro Ultrapure	18.2 MΩ.cm, TOC <2 ppb
Chloroform*	$CHCl_3$	Sigma Aldrich	≥99.8%
1,2-Dichlorobenzene	DCB	Sigma Aldrich	≥99%
4-Methyl-2-pentanone	MIBK	Sigma Aldrich	≥99%
Acetone	Acetone	Sigma Aldrich	≥99.9%
Ethyl acetate	EtAc	Sigma Aldrich	≥99.8%
Sulfuric acid	H_2SO_4	Sigma Aldrich	95-98%
Ammonium hydroxide solution ≥25% NH_3 in H_2O	NH_4OH	Sigma Aldrich	ACS reagent
Hydrogen peroxide 30% w/w in H_2O (contains no stabilizer)	H_2O_2	Fischer Scientific	

*Listed purity or similar used.

3.2.3 Results & Discussion

Method 1: Drop casting

Figure 3.7 shows a set of photographs of epoxy layers prepared by drop casting from $CHCl_3$ (Figure 3.7-A) and MIBK (Figure 3.7-B). The MIBK-cast epoxy shows much greater homogeneity across the lens. This is due to the lower evaporation rate of the MIBK, which has both a lower vapor pressure (P_{vap} = 2.64 kPa at 25 °C) and lower boiling point (B_p = 116 °C) than $CHCl_3$ (P_{vap} = 26.2 kPa at 25 °C, B_p = 61.2 °C). DCB evaporated too slowly, resulting in the epoxy creeping along the sides to the bottom of the lens (P_{vap} = 0.18 kPa, B_p = 174 °C).

Despite forming a homogeneously thick epoxy layer after drop-casting from MIBK, the gluing of the graphene/mica stack onto the epoxy layer induced thickness inhomogeneity. This occurred since the epoxy layer was too thick. Attempts to reduce this thickness were not successful. Deposited droplets must be fluid enough to be spread over the lens surface, but require some viscosity to prevent the epoxy solution from creeping along the edges

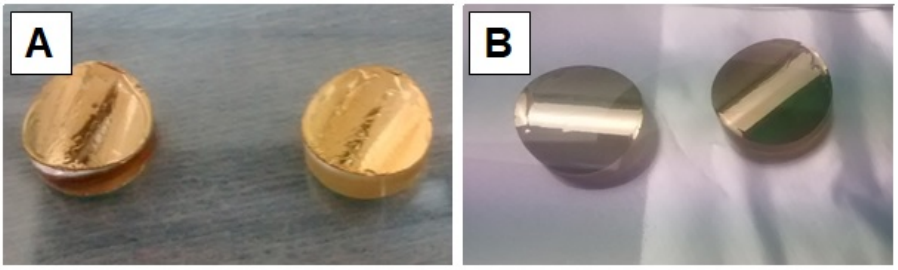


Figure 3.7: *Photographs of cylindrical quartz SFB lenses covered with a layer of epoxy fabricated by: (A) Drop casting from $CHCl_3$. The surface corrugation is visible; (B) Drop casting from MIBK. The slower drying of the epoxy/MIBK solution (melt) results in a much smoother surface.*

and depositing underneath the lens (due to pinning at the lens edge). Balancing both these factors made it difficult to obtain an appropriate thickness.

Method 2 & 3: Direct vs indirect spin casting

Spin casting is often used to create thin layers of homogeneous thickness on planar substrates. On substrates with a different shape the formation of films of homogeneous thickness becomes less straightforward. On the cylindrical lenses, spin coating with very fluid films at high speeds may result in thin center regions and an accumulation of material at the edges. Using more viscous solutions and spinning lower speeds may facilitate obtaining a more uniform film. However, due to lens curvature, the apex still represents a region of high instability at which small fluctuations result in inhomogeneity in film thickness. Therefore, next to spin casting directly onto the cylindrical lens, a different approach where the epoxy was first cast onto a planar substrate (a thin, flexible piece of mica) and subsequently transfered onto the lens was developed.

Figure 3.8 shows optical images of mirror-coated cylindrical lenses with an epoxy layer on top, viewed through a bandpass filter centered at 650 nm. The filter allows only 650 $\pm$ 10 nm light to pass. The Au mirror coating and epoxy/air interface on either side of

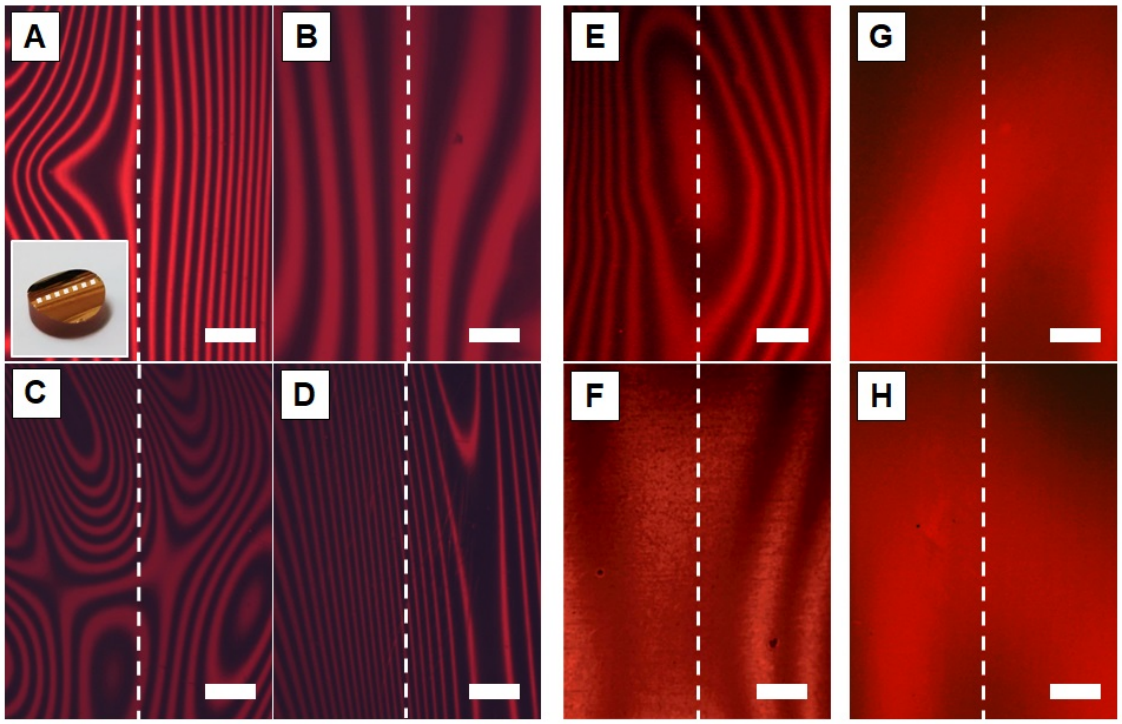


Figure 3.8: *Optical images taken through a 650 nm bandpass filter showing glue surfaces fabricated by direct spin coating (A-D) and indirect spin coating from acetone (E,F) and EtAc (G,H). The dashed lines correspond to the approximate position of the apex of the lens as indicated in the inset of A. Scale bars are all 1 mm.*

the light path through the epoxy layer form an interferometer. Only 650 nm light that satisfies the interference condition:

$$Z = m \cdot (\frac{\lambda}{2n \cdot cos(\theta)}) \tag{3.1}$$

can pass through the interferometer. Here, Z and n are the thickness and refractive index of the epoxy, λ is the wavelength, θ is the angle of incident light and m is an integer that defines the fringe order. The bright (red) and dark regions observed correspond to regions of constructive and destructive interference and are known as Newton's rings. Assuming the incident light is perpendicular to the surface and taking $n_{epoxy} = 1.593$, the height difference between two consecutive fringe orders (rings of constructive interference) is:

$$\Delta Z = \Delta m \cdot (\frac{\lambda}{2n}) \simeq \frac{650\,nm}{2 \cdot 1.593} \sim 200\,nm \tag{3.2}$$

This analysis allows for direct interpretation of the thickness homogeneity of the epoxy layer. Using the direct spin coating method can result in epoxy that has a very homogeneous thickness parallel to the apex of the lens, but is much more inhomogeneous across the apex: a direct result of the directional instability of the thinning film during spin-coating (Figure 3.8-A,B,C,D). Using the indirect spin coating method results in a much more homogeneous layer. Here, the directional inhomogeneity (being more homogeneous parallel the apex of the lens) results from the flexibility of the epoxy-supporting mica which is bent over the lens during gluing: the mica is more flexible in the bending direction (Figure 3.8-E,F). The indirect spin-coating method was further improved by casting from EtAc rather than acetone, due to the higher solubility of EPON in EtAc (3.8-G,H).

Using these methods, epoxy layers that were relatively homogeneous in thickness could be fabricated. However, the reproducibility of the spin coating process and thickness uniformity across the lens were not high enough to allow for *ex situ* calibration of the epoxy thicknesses. This is likely due to the thickness of the epoxy film, which was a few micrometers, rather than tens of nanometers as is more common for spin cast films. Using such thin films is not possible since the epoxy spacer thickness needs to be larger than the wavelength of light (see Chapters 1 and 4). Therefore, the thickness of the epoxy was determined *in situ* as described in Chapter 4.

Figure 3.9 shows several experimental interferograms of gSFB lenses with epoxy layers fabricated using different methods. For comparison Figure 3.9-A shows the interferogram recorded using a single crystal facet of mica, rather than glue. Such a mica piece exhibits a completely uniform thickness and is a good reference for comparing results obtained using the fabricated glue layers. Figure 3.9-B,C show interferograms obtained in experiments where the epoxy layers were prepared via drop casting from $CHCl_3$ (3.9-B) and MIBK (3.9-C).

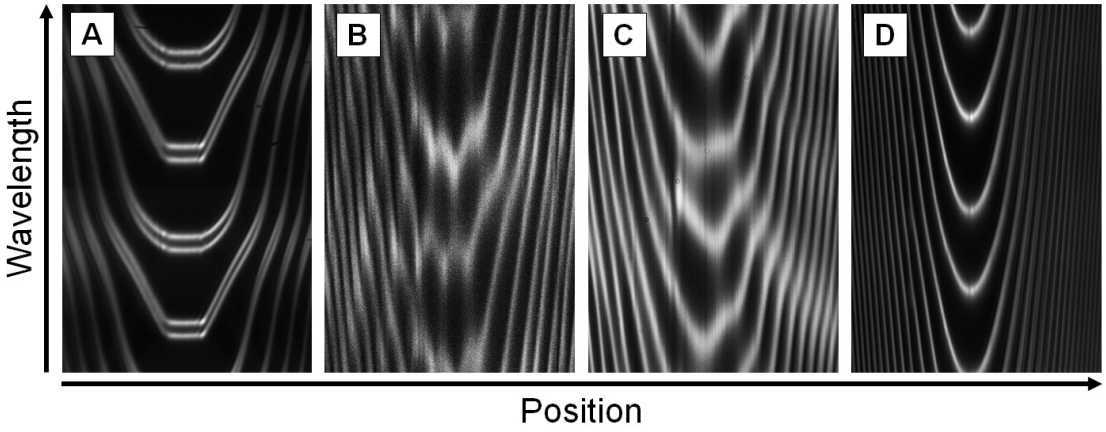


Figure 3.9: *Interferograms recorded during SFB experiments showing fringes of equal chromatic order. (A) Interferogram of fringes recorded in a classic mica SFB experiment, where mica is used instead of epoxy. The mica sheets originate from a single crystal facet and are of uniform thickness. The interference fringes have a well-defined shape. (B-D) Interferogram of fringes recorded in a gSFB experiment. In B and C The epoxy layers were prepared by drop casting from $CHCl_3$ and MIBK, respectively. The thickness inhomogeneity of the epoxy layers causes significant distortion of the fringes. In D the epoxy layer was prepared using the indirect spin casting method. The fringes are well-defined allowing for unambiguous interpretation and analysis.*

The inhomogeneity in epoxy thickness results in a highly distorted fringe pattern, which would be very challenging to analyze. Figure 3.9-D shows an interferogram of a gSFB experiment in which the surfaces were prepared using the indirect spin casting method. Here the fringes appear well-defined and can be readily analyzed.

The differences in fringe shape between Figures 3.9-A and 3.9-D arises both from the optical properties of mica and the differences in setup between the conventional mica SFB and gSFB. Due to mica's birefringence, the FECO is split and the fringes show as doublets. Further, the fringes are flat at the apex. This flattening occurs since the (rigid) silver mirror and mica spacer rest on top of a layer of deformable epoxy. When brought into contact the epoxy deforms which translates to a shorter distance between the silver mirrors, allowing the contact flattening to be observed in the FECO. This is not the case for the gSFB, where gold mirrors sit on top the un-deformable quartz lenses. A detailed explanation of the SFB interferometry can be found in Chapter 4.

3.3 Template stripping of graphene from mica

3.3.1 Introduction

Template stripping generally involves the deposition of a material on a substrate with a specific morphology as a means to impart this morphology onto the deposited material. Within the surface science community this technique is used to fabricate smooth surfaces. For example, by depositing C, Pt, or Au onto muscovite mica, and subsequently removing the mica template, it is possible to obtain smooth surfaces (RMS roughness of 0.04 nm [124], 0.1 nm [125] and 0.2 nm [126] respectively), up to an order of magnitude smoother than when obtained without using the template. The technique often involves the physical vapor deposition of noble metals onto oxide templates (i.e. mica and single crystal Si), since the adhesion between noble metals and oxides is poor. However, it can be extended to the deposition of more reactive metals by using an anti-adhesion layer (generally a self-assembled monolayer exposing alkyl chains) or via depletion of oxidizing species in the evaporation chamber [127, 128].

In 2014 Jude Britton and Nico Cousens proposed a method to template strip CVD graphene using mica as a template [86]. This method was proposed as a means to simultaneously circumvent roughness induced by graphene wrinkles and polymer-contamination that may be introduced during the transfer process. Wrinkles arise due to the difference in thermal expansion coefficient between graphene and the Cu growth substrate and may be induced during the polymer-assisted transfer from the growth substrate. The use of template stripping resulting in a reduction of the RMS roughness from 4.43 nm to 0.44 nm, when measured on a 5x5 μm^2 area [86]. The method ensures no material protrudes from the resulting graphene surface - detrimental to the measurement of forces at small distances in SFB experiments. The resulting surface is still much rougher than the mica template (0.034 nm RMS roughness), a single ($\sim \mu$m^2 size) exfoliated graphene flake de-

posited on mica (0.024 nm RMS roughness) or a single crystal graphite terrace (0.022 nm RMS) [14].

3.3.2 Materials & Methods

Epoxy-covered SFB lenses were prepared according to the procedures outlined in the previous sections. After preparation of the glue surface the mica-supported graphene (FLG, SLG or mmSLG) was carefully placed on top of the epoxy surface heated to 150 °C. The capillary force at the advancing front at the glue-graphene/mica interface pulled the graphene/mica stack across the lens, ensuring conformal contact whilst retaining (part of) the surface topology.

After gluing the graphene/mica stack, the mica was removed by careful peeling in water. In some cases the graphene/mica/lens assembly was stored in a home-built humidity chamber prior to template stripping, as follows. The assembly was put on a small stage in a larger 500 mL beaker, covered with aluminum foil filled at the bottom with a small amount of water and kept at 40 °C.

Raman spectroscopy was performed using a JY Horiba LabRAM ARAMIS imaging confocal Raman microscope using a 532 nm laser. OM was performed using a Yenway CX40M metallurgical microscope. Conductance across the graphene-covered gSFB lenses was measured using a multi-meter.

3.3.3 Results & Discussion

First the epoxy surfaces resulting from template stripping in absence of graphene will be discussed to establish a baseline, followed by verification of the presence of graphene on the surface. Then a detailed investigation of the template stripping of graphene from mica will be presented.

Figure 3.10 shows AFM height maps of template stripped epoxy surfaces. For EPON,

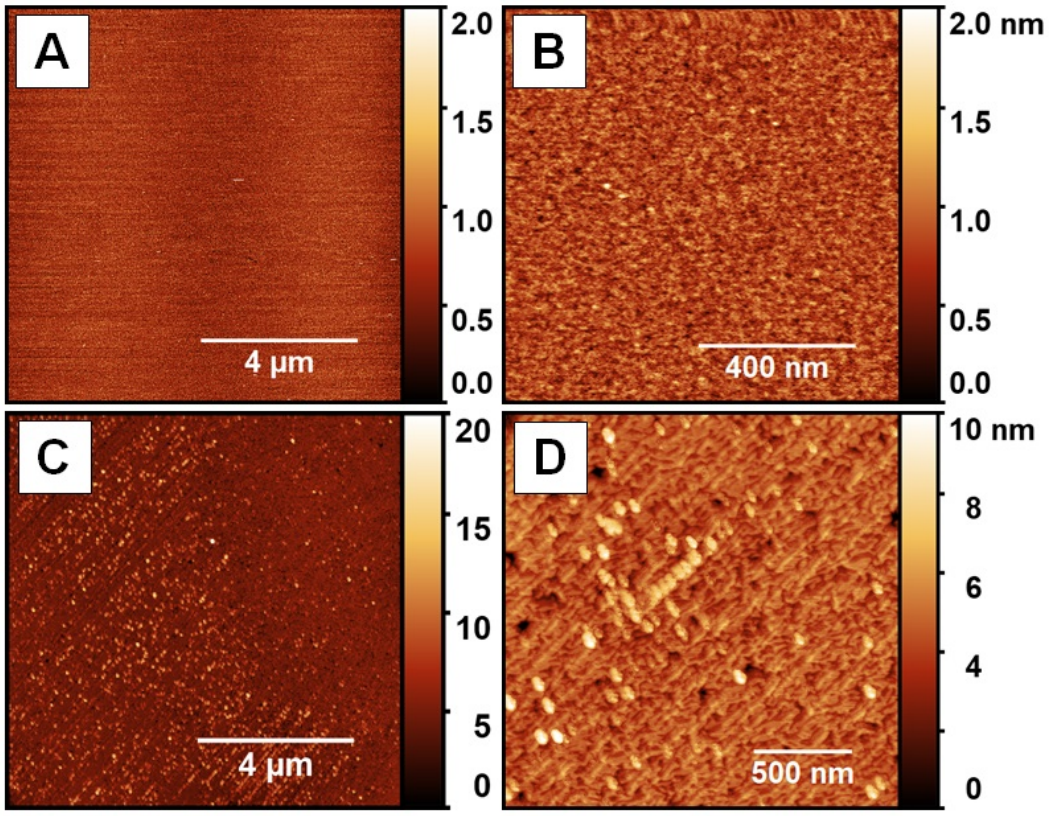


Figure 3.10: *TM-AFM height maps of epoxy surfaces. (A,B) 10 x 10 and 1 x 1 μm^2 map of the EPON surface after template stripping from mica. The surface is smooth and featureless. The measured RMS roughnesses are 0.177 nm and 0.184 nm respectively. (C,D) 10 x 10 and 1 x 1 μm^2 map of the PS surface after template stripping from mica. The surface has a clear structure, resulting in measured RMS roughnesses of 1.44 nm and 1.38 nm respectively.*

a $\sim 1715\,\mathrm{g\,mol^{-1}}$ epoxy derived from bisphenol-A and epichlorohydrin [129], the surface is smooth and featureless with an RMS roughness of 0.177 nm on a 10 x 10 μm^2 and 0.184 nm for 1 x 1 μm^2 area (Figure 3.10-A,B). The surface of template stripped polystyrene (PS) with an average molecular weight of $35\,000\,\mathrm{g\,mol^{-1}}$ has a clear structure with RMS roughnesses of 1.44 nm on 10 x 10 μm^2 and 1.38 nm for 1 x 1 μm^2 (Figure 3.10-C,D). The higher roughness of the PS may be due to its much longer chains, which interdigitate and cause the material to store mechanical stress [130, 100]. The difference in surface topography indicates that EPON is a more suitable epoxy for obtaining smooth graphene surfaces than PS.

The presence of graphene on the surface was verified using multiple methods. First,

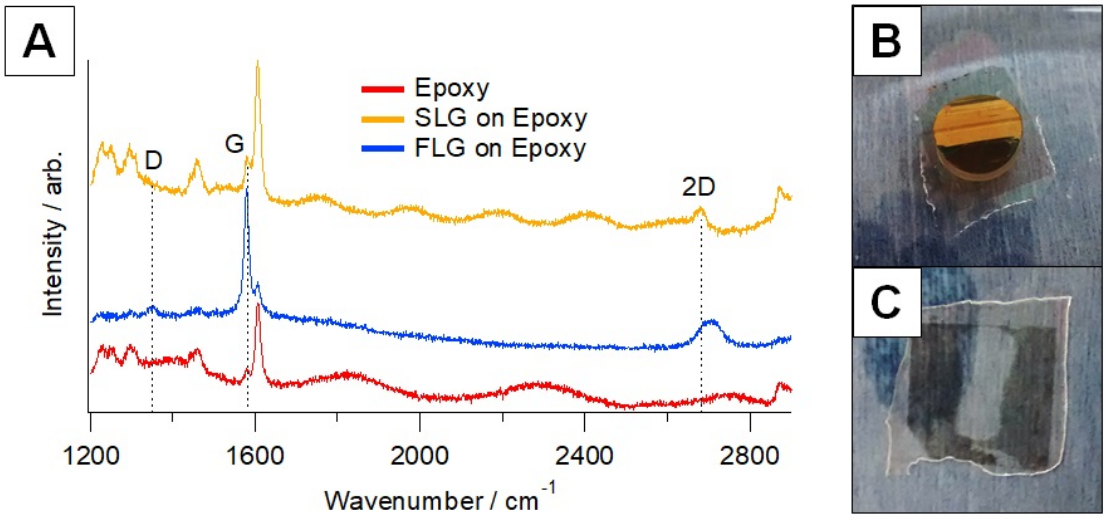


Figure 3.11: *Raman spectra and photographs showing evidence for the presence of graphene on the epoxy. (A) Raman spectra of SLG, FLG on epoxy. For FLG (blue) the spectral features are distinguishable. For SLG (yellow), the characteristic Raman spectrum is largely obscured by the spectrum of the underlying epoxy (red). (B,C) Photograph of FLG-supporting mica before and after stripping of the epoxy-covered cylindrical lenses. The area where graphene has been transferred from the mica onto the lens is visible.*

Raman spectroscopy was used to reveal the characteristic Raman spectrum of the epoxy-supported graphene. Figure 3.11-A shows several Raman spectra of SLG and FLG after gluing onto an EPON-covered lens. For FLG, the Raman signature is clearly visible. For SLG, the Raman signature can just be distinguished from the signal of the underlying EPON. Second, the presence of a conducting graphene layer on the insulating epoxies was verified by measuring the resistance across the surfaces, using a multimeter. Third, due to the optical absorption of graphene, the presence of both FLG and (mm)SLG could also be assessed by inspection of the mica template as follows. Figure 3.11-B,C, shows a photograph of a FLG-supporting mica template on top of a cylindrical lens before (B), and after (C) template stripping. The transfered area can be distinguished due to its darker color (note that the same is observed for (mm)SLG, but more difficult to image). Further, the presence of a single interference color of the single crystal mica terrace indicates that the mica remains intact (i.e. was not cleaved during template stripping) and only the

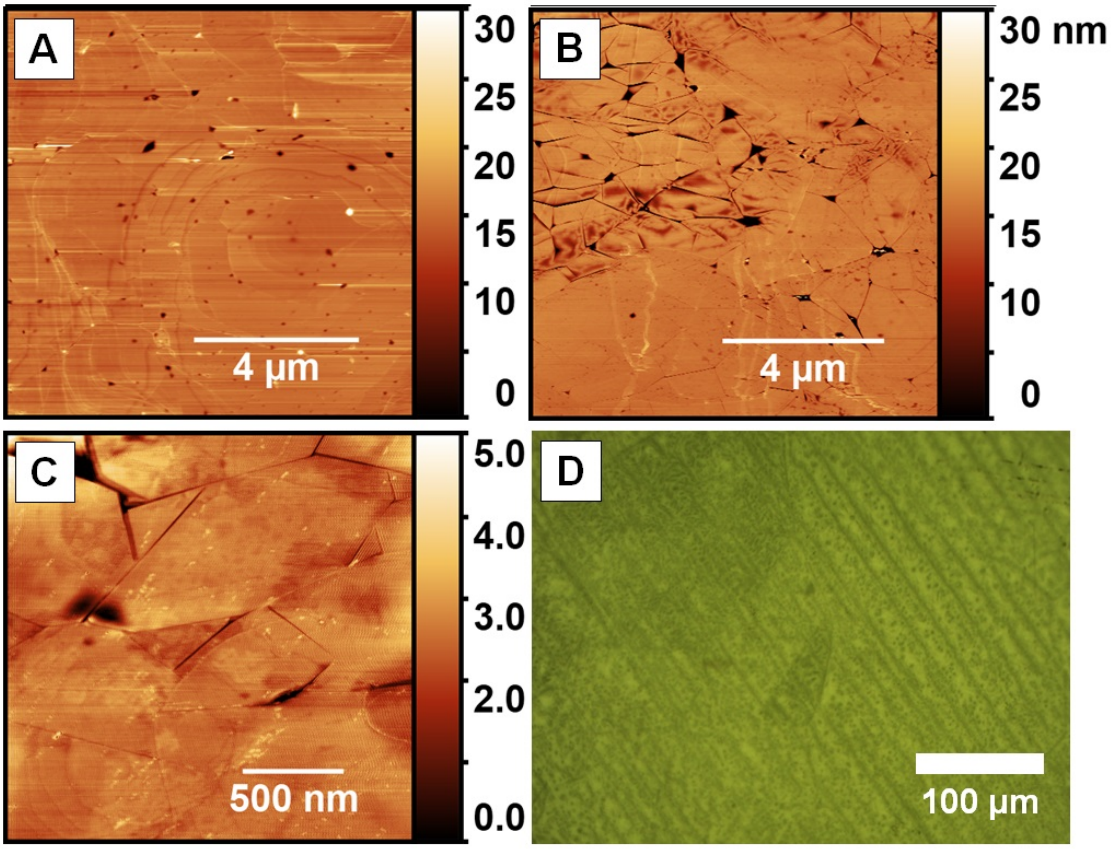


Figure 3.12: *Characterisation of FLG-covered gSFB lenses. (A) 10 x 10 μm^2 C-AFM height map. The RMS roughness is 1.16 nm. The FLG was grown after cleaning the Cu growth substrate with AcH. (B,C) TM-AFM height maps of 10 x 10 μm^2 and 2 x 2 μm^2 areas, with a measured RMS roughness of 2.9 nm (<1 nm in the region without holes) and 0.489 nm respectively. The FLG was grown after cleaning the substrate with HNO_3. (D) OM image of the FLG-covered gSFB lens surface.*

graphene remains glued down on the epoxy surface. Altogether, this combination of evidences strongly indicates that the graphene is successfully transferred onto the lens.

Figure 3.12 shows C-AFM and TM-AFM height maps and an optical image of FLG-covered gSFB lenses. The height map in Figure 3.12-A shows a C-AFM surface of FLG grown after cleaning the Cu growth substrate with AcH. Some particles are visible. The particles are absent in Figure 3.12-B, showing a TM-AFM height map of graphene grown on FLG after cleaning the Cu substrate with HNO_3. The AFM images confirm the absence of large protruding features, such as wrinkles. Instead, they show a smooth surface with an RMS roughness of 1.16 nm (3.12-A) and 2.9 nm (3.12-B, <1 nm in areas without holes) on a 10 x 10 μm^2 area, with only negative protrusions (holes). These most likely arise

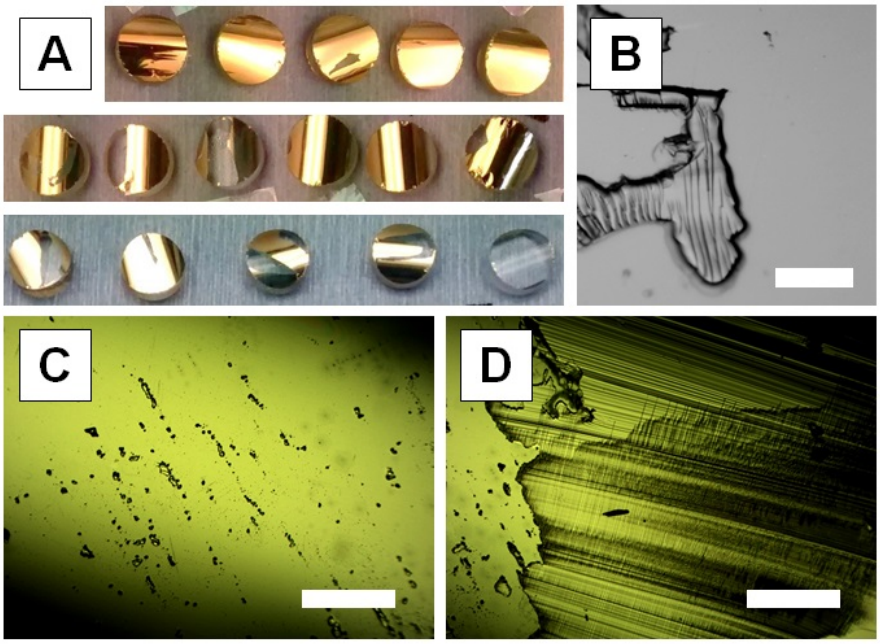


Figure 3.13: *Photographs (A) and OM images taken with a transmission (B) and confocal (C,D) microscope. (A) shows photographs of gSFB lenses after template stripping in absence of a Cr adhesion layer between the cylindrical quartz lens and the gold mirror, using: thin mica/thick glue and FLG (top row); thick mica/thin glue and FLG (middle row); thin mica/thick glue and SLG (bottom row). (B) OM image of glue rips in SLG-covered gSFB lens. Scale bar is 20 µm (C,D) OM image of glue rips in mmSLG-covered gSFB lens. Scale bar is 0.5 cm.*

due to incommensurability between polymer-supported graphene and the mica substrate during transfer. On the smaller, 2 x 2 μm^2 area shown in 3.12-C, the RMS roughness is 0.489 nm.

The OM image (3.12-D) shows a defect free surface similar to what is observed using SEM (Figure 2.3). In low voltage SEM the secondary electrons emerging from the sample are strongly influenced by graphene layer number. The absorbance of visible light by graphene follows a similar layer dependence.

The initial experiments (such as for the results published in 2014) used gold-coated cylidrical quartz lenses. On top of these the epoxy and graphene/mica were placed. The resulting stack contained quartz/gold/epoxy/graphene/mica. Upon removal of the mica template in water, the plane of separation would occasionally be at the quartz/gold interface, rather than the graphene/mica. Template stripping of FLG from mica was performed

in water, since it facilitates the removal by lowering the interfacial energies of graphene and the (super) hydrophilic mica template [86]. The location of cleavage plane was found to be dependent on both the epoxy and mica thicknesses, with thicker epoxy and thinner mica giving a higher chance of separating at the graphene/mica interface. Figure 3.13-A shows the result of template stripping with thin (top row) and thick (middle row) mica.

The use of SLG greatly reduced the chance of cleavage occurring at the graphene/mica interface (Figure 3.13-A, bottom row). To prevent cleavage at the Au/quartz interface, a layer of Cr was used as adhesion layer between the quartz and the Au. This ensured cleavage occurred at the interface between graphene and mica. However it also resulted in the occasional observation of rips in the epoxy (Figure 3.13-B). Thus, it is likely that due to the high adhesion between graphene and mica, the mechanically weakest component in the quartz/Cr/Au/epoxy/graphene/mica stack is either the epoxy or the graphene/mica interface. Damage to the epoxy layer was even more profound when mmSLG was used. In this case rips were always observed on some location of the lens (Figure 3.13-C,D). When PS rather EPON was used as epoxy, mmSLG could be template stripped from mica without any damage to the surface.

When the epoxy layer breaks during template stripping, particulates may be released into the liquid (water). Further, if such damage occurs at the apex of the lens, it prevents the damaged area from being used during the experiment.

Figure 3.14 shows a TM-AFM images of different graphene-covered lenses. Figure 3.14-A,B shows a 10x10 μm^2 and 5x5 μm^2 image of a SLG-lens surface. The measured RMS roughnesses are 1.29 and 0.561 nm respectively. Figure 3.14-C,D shows two 10x10 μm^2 images of the mmSLG surface. The RMS roughness measures 0.678 and 0.479 nm respectively (0.214 and 0.245 nm when an area without holes is selected). Figure 3.14-E,F shows two 2x2 μm^2 areas on mmSLG with an RMS roughness of 0.296 and 0.226 nm. Next to holes, a fractal pattern seems visible on the surface. Figure 3.14-G,H shows a 10x10

μm^2 and 1x1 μm^2 of mmSLG supported by PS rather than EPON. The RMS roughnesses measure 1.40 and 2.0 nm respectively.

The measured RMS roughnesses correlate with observations made during template stripping. For FLG-covered gSFB lenses, which present the roughest surface, cleavage occurred at the mica/graphene interface. For the smoother SLG- and even smoother mmSLG-covered surfaces, an increase in surface damage is observed. When PS rather than EPON was used for mmSLG, this resulting in a much rougher surface, concomitant with cleavage purely at the graphene/mica interface.

Adhesion between two materials is governed by the interfacial energy between them and the effective contact area. In the case of graphene and mica, the contact area increases with the appearance of damage to the surface. However, on all surfaces smooth areas can be observed and were imaged in absence of glue rips. Surface area alone may therefore not be the deciding factor. It is possible that separation of the graphene from the mica is facilitated by the presence of water between the graphene and the mica. After placing the graphene on the mica during the polymer-assisted transfer step, some residual water is present and facilitates the conformal contact between the mica template and the polymer-supported graphene film through capillary force. It is likely that after the bulk water dries, some interfacial water remains, as has been observed for graphene on both mica and SiO_2 [131, 132].

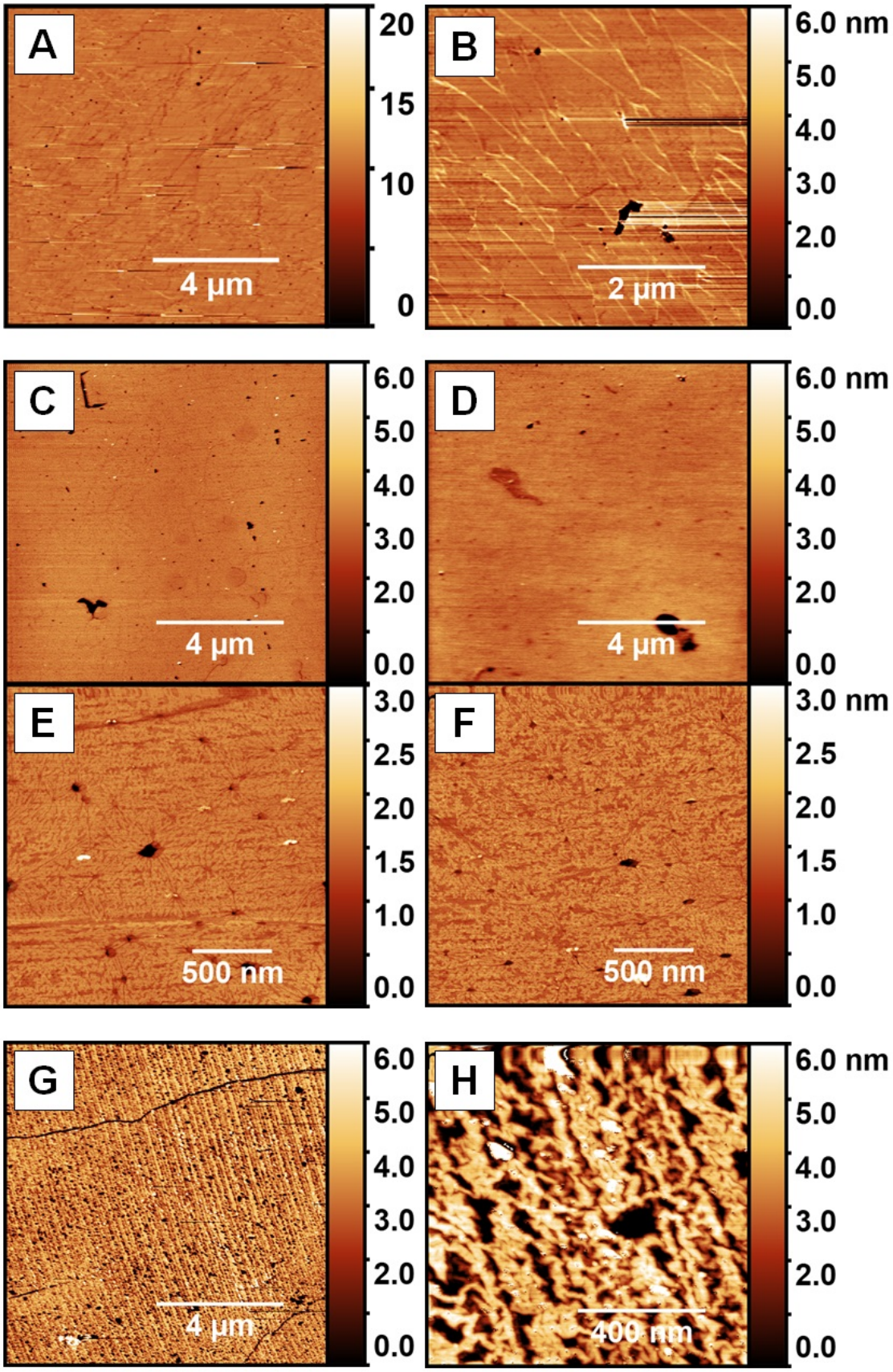


Figure 3.14: *TM-AFM height maps of template stripped graphene surfaces supported by different epoxies. (A,B) SLG on EPON. RMS roughnesses are 1.29 nm (A) and 0.561 nm (B). (C,D,E,F) mmSLG on EPON. RMS roughnesses are 0.678 nm (C), 0.479 nm (D), 0.296 nm (E), and 0.226 nm (F). (G,H) mmSLG on PS. The RMS roughnesses measure 1.40 nm (H) and 2.0 nm (G).*

During template stripping additional water diffuses in between the mica and graphene, facilitating separation. For the smoother graphene surfaces this process is expected to be much slower. This is supported by the observation that diffusion of water between mica and single layer graphene occurs at a slower rate than between mica and few layer graphene. This arises from the higher flexibility of the single layer graphene, which allows it to conform better to the underlying substrate [133]. Template stripping after having the mica/graphene/epoxy/lens assembly in water for 15 minutes or overnight storage in a home-built humidity chamber was therefore attempted, but did not prevent surface damage.

The high adhesion between mica and graphene thus seems to limit the surface smoothness that can be obtained. This is prohibitive for gSFB experiments, which require a surface that is as smooth as possible. For example, it is unlikely that a surface with features multiple times larger than the dimension of the molecules of a liquid studied, will allow for observation of any interfacial structure. Further, even if longer range forces are studied, such roughness would have to be accounted for in models describing observed behavior.

Finally, it should be noted that although gSFB lenses with clean and smooth surfaces can be fabricated, highly damaged or contaminated lenses have also been observed (Figure 3.15). Although the contamination seems to vary between lenses, rather than within one lens, it is likely that such areas exist on every lens, due to the large number of steps involved in the fabrication. The prevalence of such particles could potentially be reduced using etchants such as KOH or HCl. However, the use of strong bases or acids is hazardous and introduction of additional rinsing steps increases the chance of contaminating the system or damaging the polymer-supported graphene.

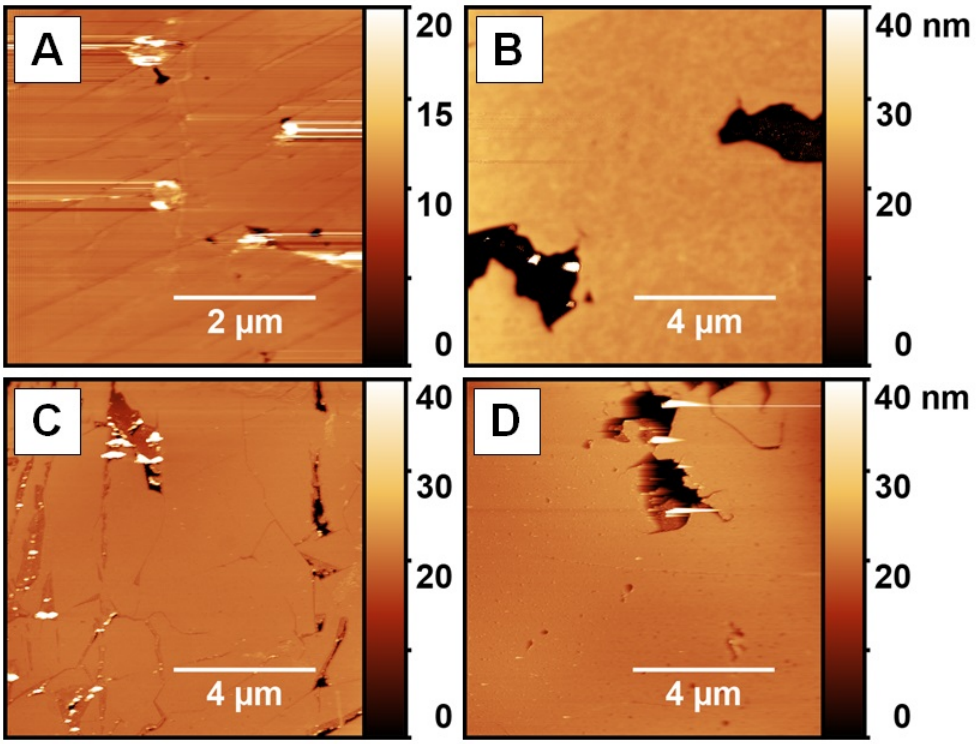


Figure 3.15: *TM-AFM height maps of gSFB lens surfaces with contamination or severe damage. (A) SLG lens covered with ∼30 nm particles. (B) mmSLG lens with large ∼50 nm pits. A ∼120 nm particle sits in one of the pits, sticking out 70 nm. (C) mmSLG surface where the graphene cracked during transfer. In the cracks ∼50 nm particles are visible. (D) mmSLG surface with large holes and particles. One of the particles sticks 100 nm above the surface.*

3.4 Conclusion

Graphene-covered gSFB lenses that are smooth on a nanoscopic and macroscopic scale were fabricated. Various methods, including drop-casting, direct-, and indirect spin-coating were attempted for the fabrication of the graphene-supporting epoxy layer. The use of indirect spin-coating of EPON™ Resin 1004F dissolved in Ethyl Acetate resulted in the formation of macroscopically uniform epoxy layers with thickness deviations of less than 200 nm over multiple millimeters across the gSFB lenses. Template stripping of various CVD-grown graphenes from mica templates was used to fabricate gSFB lenses with a nanoscopically smooth graphene surface. Using mmSLG, a graphene surface with a RMS roughness of 0.5 nm was achieved. However, due to the high adhesion between mica and smooth graphene films it was not possible to fabricate surfaces with RMS roughnesses that approach molecular dimensions.

Additional fabrication steps that reduce the adhesion between graphene and the template could be implemented to circumvent difficulties experienced when template stripping mmSLG from mica. For example, an alkyl-terminated self-assembled monolayer on mica could be used to lower adhesion. However, the introduction of additional fabrication steps increases the chance of introducing contaminants.

Chapter 4

Analysis of the interference spectra

The previous chapters have outlined methods by which to fabricate gSFB lenses. After their successful fabrication, these are mounted inside the SFB in crossed-cylindrical configuration and can then be used to perform an experiment. However, the analysis of the interferometric data obtained in a gSFB experiment is significantly more complicated than when using the conventional mica SFB. The non-uniformity in thickness of the epoxy layer may cause deviations in radius of curvature which need to be accounted for. Further, due to concerns regarding surface stability (see Chapter 5) it was not possible to perform a conventional distance calibration. Therefore, it was necessary to developed new analysis procedures that allow for the reliable interpretation of the FECO.

The first section of this chapter introduces the existing methods for analysis of interferometric data obtained with the conventional mica SFB and discusses the origins of the observed FECO. Section 4.2 will discuss how to use the interferometric data to account for changes to the radius of curvature due to the non-uniformity of the epoxy layer. The final section in this chapter details a numerical method for efficiently determining

the thicknesses of the graphene-supporting glue layers without bringing the surfaces into contact.

4.1 Introduction

4.1.1 The different approaches to analyzing FECO

In a conventional experiment, the mica surfaces are first brought into contact for a so-called "contact calibration". At the conception of the SFB as measurement technique, Isrealachvili derived a set of analytical equations to convert movement of the FECO into distance changes between the surfaces using this calibration as a reference for $\mathbf{D} = 0$ [3]. The use of these equations requires the use of a symmetric interferometer, which is the case when the micas originate from the same single crystal [134]. For asymmetric setups analytical equations for conversion of the FECO into distance exist, but have not found widespread use [135]. Alternatively the FECO may be matched numerically to spectra calculated using optical transfer matrixes.

The multilayer matrix method (MMM) as referred to by Clarkson [134], uses the characteristics of all the optical elements or layers in the light path, by assigning each layer a characteristic matrix M_i [136]. The transmitted spectrum is the matrix product M of these individual layers, so that:

$$M = \prod_{i}^{N} M_i \tag{4.1}$$

where

$$M_i = \begin{bmatrix} \cos q & -\frac{i}{p}\sin q \\ -ip\sin q & \cos q \end{bmatrix} \tag{4.2}$$

with

$$q = \frac{2\pi\,\tilde{n}\,z}{\lambda}\cos\theta \qquad \text{and} \qquad p = \sqrt{\frac{\epsilon}{\mu}}\cos\theta \tag{4.3}$$

Here, $\tilde{n}$ is the complex refractive index, z is the thickness of the layer, λ is the wavelength, θ is the angle between the incoming beam of light and the surface normal (for crossed cylinders with $\mathbf{D} \ll \mathbf{R}$ and $\cos\theta = 1$), and ϵ and μ are the dielectric constant (permittivity) and magnetic permeability. For non-magnetic materials, p effectively corresponds to the refractive index. The resulting transmission through a stack containing n individual layers has the form:

$$T = \frac{p_0}{p_{n+1}} \left| \frac{2p_0}{(m_{11} + m_{12}\, p_{n+1})\, p_0 + (m_{21} + m_{22}\, p_{n+1})} \right|^2 \tag{4.4}$$

where $m_{j,k}$ refers to the element with index j, k of the matrix M and p_0 and p_{n+1} are the values of p of the semi-infinte layers adjacent to the interferometer stack. The notation [*semi-infinite layer*|layer 1|layer 2...|layer n|*semi-infinite layer*] will be used when referring to the interferometer stack.

In the conventional mica setup, the thickness of the micas can be determined from a contact calibration by fitting the FECO to spectra calculated using the MMM. An efficient method for doing this was introduced by Heuberger [137].

The advantage of using the MMM lies in its versatility. For example, it can be used to account for differences in refractive indexes between literature and those in experiment [20], non-uniform refractive index profiles of adsorbed surface layers [138] or less conventional setups for which no analytical solution is available [139, 140].

4.1.2 The different FECO orders and their origins in the gSFB

To understand the interferograms obtained in gSFB experiments, it is important to gain a qualitative understanding of the different FECO patterns. At the origin of every FECO pattern lies a reflection between two surfaces. The reflectance of each of these surfaces

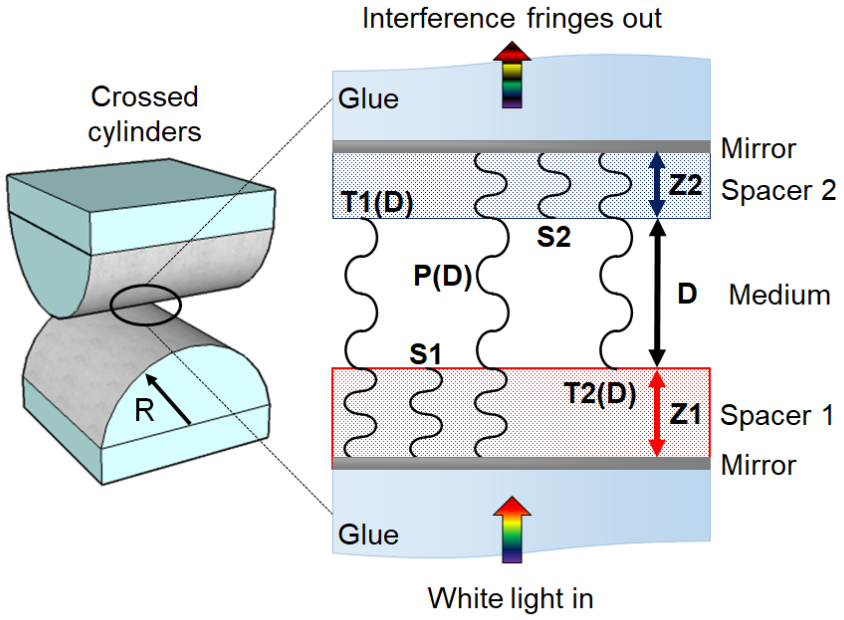


Figure 4.1: *Schematics showing a generalized SFB configuration. The two lenses are placed into crossed-cylinder configuration, equal to that of a sphere on a flat plane. The interferometer inside the SFB consist of two mirrors with a spacer on top. The spacers, for example mica or epoxy-supported graphene, are in contact with the medium of interest. Primary fringes* ***P(D)*** *result from reflections between the mirrors. Secondary fringes (****S1,S2****) result from reflections between the mirror and the closest spacer|medium interface. Tertiary fringes (****T1,T2****) result from reflections between the mirror and the opposing spacer|medium interface.*

arises from the refractive index mismatch at the interface. For non-absorbing materials with light incident perpendicular to the interface the reflectance R^* is [136]:

$$R^* = \left| \frac{n_1 - n_2}{n_1 + n_2} \right|^2 \tag{4.5}$$

where n_1 and n_2 correspond to the refractive indexes of the two interfacing materials. Table 4.1 provides an overview of approximate refractive indexes and reflectance values of materials commonly used in SFB experiments in the wavelength range of 540 nm – 580 nm.

Figure 4.1 shows the generalized configuration used for most SFB experiments, which corresponds to: [*glue*|mirror|spacer 1|medium|spacer 2|mirror|*glue*]. Primary fringes, denoted by **P(D)** arise from reflections between the mirror|spacer1 and spacer2|mirror in-

terfaces and depend on the distance **D** + **Z1** + **Z2** between them. Higher order fringes arise from reflections between the mirror|spacer and spacer|medium interfaces. Two sets of secondary fringes, **S1** and **S2** in Figure 4.1, depend only on the thickness of their respective spacer layers **Z1** and **Z2**. In the special case of a symmetric setup, **Z1** = **Z2** and only one set of secondary fringes is visible. Tertiary fringes (**T(D)**) depend both on **Z1,2** and on **D** [141].

Due to the high reflectance at the mirror|spacer interface compared to the spacer|medium interface, the relative intensity of the fringe orders is typically: $I_{P(D)} > I_S > I_{T(D)}$. The intensity of each set of fringes is divided over all fringe orders and depends on **D** for both **P(D)** and **T1(D)**, **T2(D)**. Therefore, at small surface separations, **P(D)** dominates the FECO. When the separation is large, **S1** and **S2** dominate.

Table 4.1: Approximate refractive indexes and reflectance values of common materials in the range 540 nm – 580 nm.

Material	**Refractive index (n)**	**Interface**	**Reflectance** (R^*)
Silver	≤ 0.1	mica or epoxy|silver	0.77
Gold	0.3	mica or epoxy|gold	0.45
Mica	1.6	mica or epoxy|air	0.05
Epoxy	1.55	mica or epoxy|water	0.01
Air	1.0		
Water	1.33		

Figure 4.2 shows several calculated interferograms for different SFB setups and serves as an illustration of several spectral features. The left column shows a schematic of the corresponding geometry. The middle column shows interferograms for which the surfaces are at a large serparation, **D** = 200 μm. The right column shows interferograms for which the surfaces are at much smaller separation, **D** = 1 μm. In all cases a two-dimensional slice through the crossed-cylinders, equal to a sphere on a flat plane, was calculated. This slice corresponds to the slice as selected by the spectrometer slit along y (also shown as x in Figure 1.1-B). The length of the slice is 200 μm. The interferograms shown on the

top in each panel represent data from such a slice as collected during a SFB experiment. Shown underneath each of these is the interference spectrum corresponding to the center distance (y = 0). To increase the visibility of the secondary fringes to the untrained eye, the refractive index of the spacer, was set to $n_{spacer} = 2$, and the refractive index of the medium was set to $n_{medium} = 1$. The optical constants of gold were used for the calculation of the mirror layer [142]. Due to its dispersion (i.e. $\tilde{n} = \tilde{n}(\lambda)$) the fringe intensity increases towards the red end of the spectrum.

In all cases, primary fringes are visible as bright arcs with their apex towards the blue end of the spectrum, since the spacing between a sphere and a flat always decreases towards the apex. This curvature directly reflects the curvature of the mirrors (1 cm). The importance of the presence of the spacer layer is immediately evident from examining the **D** = 1 μm case in Figure 4.2-A: even though **D** is larger than the diffraction limit of light in the chosen wavelength range, only part of a single FECO is visible.

For a symmetric setup with spacer thicknesses **Z1** = **Z2** = 5 μm, as shown in Figure 4.2-B, the full FECO is visible. Here, the secondary fringes are visible as vertical bands at large distance (middle), and as a peturbation to the primary fringes at small distance (right). In the line profile they appear as an elevated background underneath the primary fringes.

In Figure 4.2-C the thickness of one of the spacers was changed so that **Z1** = 6.5 μm (highlighted in red in the schematic). As a result the secondary fringe bands **S1** and **S2** only partially overlap, giving a bright band at $\sim$ 550 nm and weaker bands at longer wavelengths.

Figure 4.2-D shows the situation in which the thickness of **Z1** varies. The profile of **Z1** is that of an arc with a height of 1 μm on top of a rectangle with a height of 5.5 μm. Since the thickness of **Z1** increases towards the center, the resulting secondary fringes have their apex towards the red end of the spectrum.

Due to the use of a thermosetting epoxy to support the graphenes, rather than two single crystal mica sheets, the thickness of the epoxy spacers is not constant. Section 4.2 will discuss how to account for the resulting changes in the radius of curvature, **R**. Section 4.3 will discuss how to efficiently determine the thicknesses of **Z1** and **Z2** without performing a contact calibration.

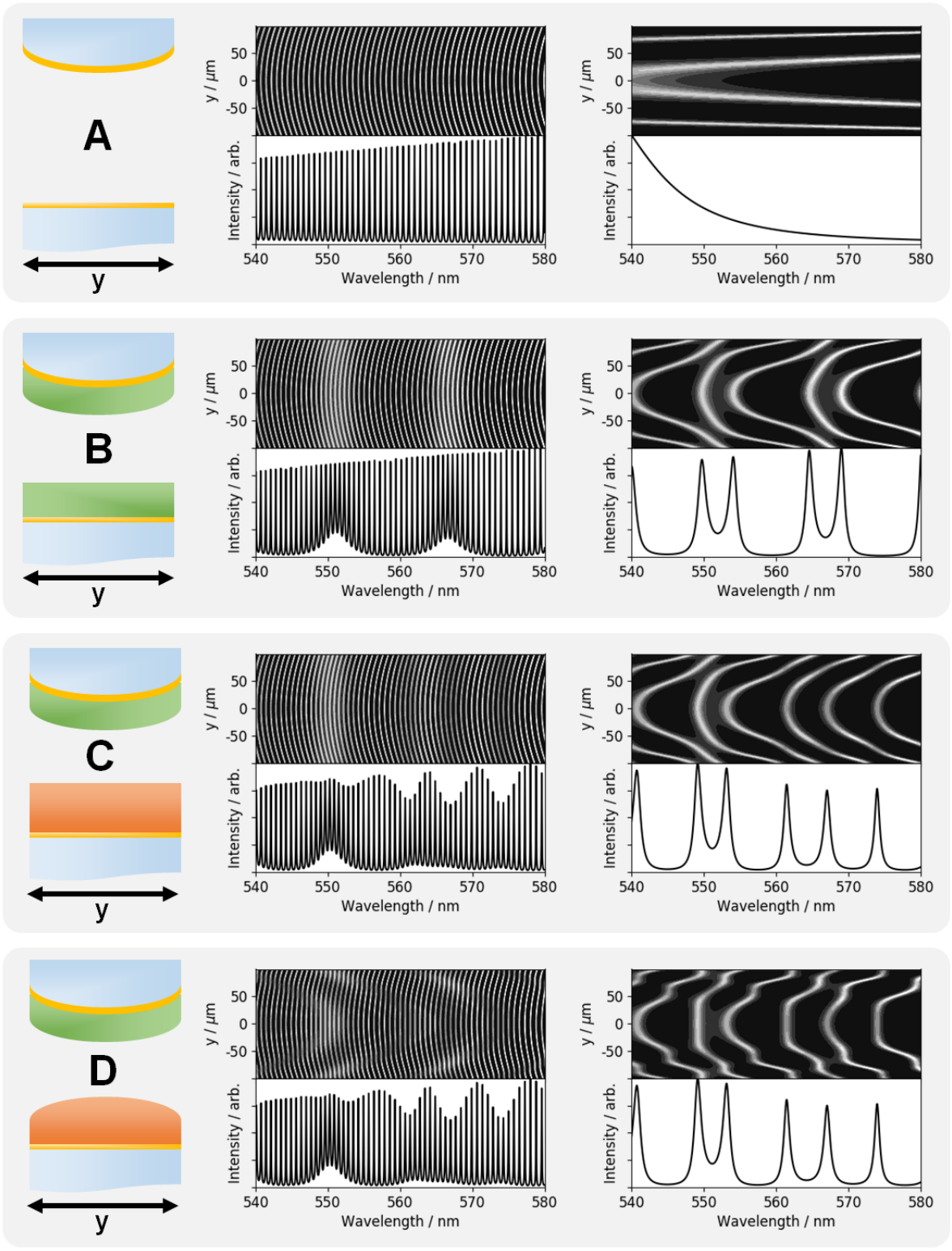


Figure 4.2: *Interferograms calculated for different SFB configurations. The left column shows a schematic of the configuration used. The middle and right column show interferograms at large (**D** = 200 µm) and small (**D** = 1 µm) distance respectively. Underneath each of the interferograms a line profile through the center of the top image is shown. (A) Shows the interferogram obtained in absence of spacer layers. In (B) **Z1** = **Z2** = 5 µm, whereas in (C) **Z1** = 6.5 µm and **Z2** = 5 µm. (D) Shows the calculated interferogram obtained when **Z1** has the shape of an arc with a height of 1 µm on top of a rectangle with a height of 5.5 µm.*

4.2 Radius of Curvature

An account of this work was accepted for publication in 2017 [143].

Correct determination of the radius of curvature **R** is important, since it allows force measurements to be normalized and compared to other reported literature values. In the conventional mica SFB, **R** may be determined directly from the curvature of the primary fringes: the mica is of uniform thickness and has a layer of evaporated silver on the back, so that curvature of the primary fringes corresponds to that of the mica surfaces. This is typically done by using an interferogram recorded *in situ*, when liquid is present between the surfaces, to minimize the perturbation of the primary fringes by the secondaries. The value of **R** is described by an arc according to:

$$R = \frac{\Delta y^2}{8\,\Delta f} + \frac{\Delta f}{2} \tag{4.6}$$

where Δy is the lateral distance and Δf corresponds to some distance between the fringe apex and the line Δy, as shown in the calculated interferogram in Figure 4.3-A (the distance between consecutive fringe orders was chosen for clarity). Note that in the images in Figure 4.3 realistic values for the refractive indexes were used.

Figure 4.3-B shows a calculated interferogram for which the thickness of the epoxy spacer is uniform. The red dashed line highlights the position of the secondary fringes. In this case the radius of curvature of the epoxy-supported graphene surface R_G, is equal to the radius of curvature of the lens R_L. When one of the epoxy spacers is thicker at the apex of the lens and the other is uniform in thickness, this results in the observation of one secondary fringe which curves with its apex towards the red, and one straight secondary fringe (Figure 4.3-C). In this case R_G is different from R_L. When the epoxy layer is thinner at the apex, the corresponding secondary fringes curve towards the blue (Figure 4.3-D).

Since the shape of the secondary fringes reflects the thickness profile of the epoxy spacer, the curvature of the secondary fringes R_S can be used to determine R_G.

Due to the fabrication method of the epoxy layer outlined in Section 3.2 and as is visible from the Newton's rings shown in Figure 3.8-E,F, the epoxy is generally uniform in thickness along the apex of the lens (y-axis of the bottom lens in Figure 4.4-A), and has some variation in height perpendicular to the apex of the lens (x-axis of the bottom lens in Figure 4.4-A). Hence, the surface curvature and secondary fringes arising from the thickness non-uniformity along the apex of the lens will be referred to as $R_{G\parallel}$ and $R_{S\parallel}$ respectively. The surface curvature and secondary fringes arising from the thickness non-uniformity perpendicular to the lens will be referred to as $R_{G\perp}$ and $R_{S\perp}$. When $R_{S\parallel}$ are straight or have a very large radius of curvature, $R_{S\parallel} \to \infty$ and thickness deviations of the epoxy spacer in this direction are negligible. Then, $R_{S\perp}$ can be used to determine the surface curvature $R_{G\perp}$ using a simple model.

Figure 4.4-B shows the schematic used to described the model. It describes the cylindrical lens as a circle with radius R_L with the epoxy-supported graphene surface as an overlaying circle with radius $R_{G\perp}$. The model's main assumptions are that the secondary fringes are aligned co-axially with the primary fringes (as in Figure 4.3-C,D). During a gSFB experiment a spot that meets these criteria is selected by inspecting the Newton's rings caused by the height variation of the epoxy layer *in situ*, and may be accessed moving by one of the gSFB lenses laterally. Whether an appropriate measurement spot is found can be verified by inspecting the interferogram.

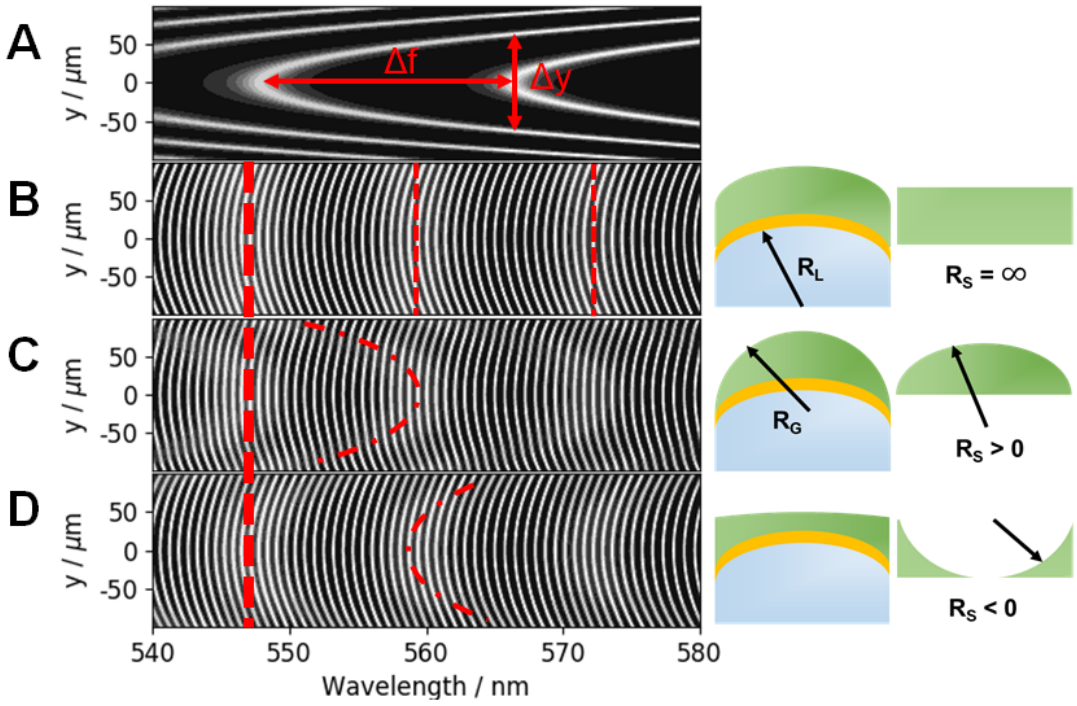


Figure 4.3: *Calculated interferograms showing secondary fringes resulting from different glue morphologies. (A) The radius of curvature is determined by measuring the width of a single FECO, Δy, and the distance between the apex of this fringe and Δy (Δf), and using these values in equation 4.6, which describes the relation between the width (Δy) and height (Δf) of an arc in relation to its radius of curvature. (B-D) Interferogram (left) and schematic of one of the gSFB lenses (right) showing: (B) two lenses with an epoxy spacer of uniform thickness; (C) one of the lenses with uniform epoxy thickness and the other with a thicker layer of epoxy at the center than at the edges; (D) one of the lenses with uniform epoxy thickness and the other with a thinner layer of epoxy at the center than at the edges. The dashed lines indicate the location of the secondary fringes from the uniform epoxy layer, the dash-dotted lines indicate the location of the secondary fringes from the non-uniform epoxy layer. Realistic refractive index values and thicknesses were used for the calculation.*

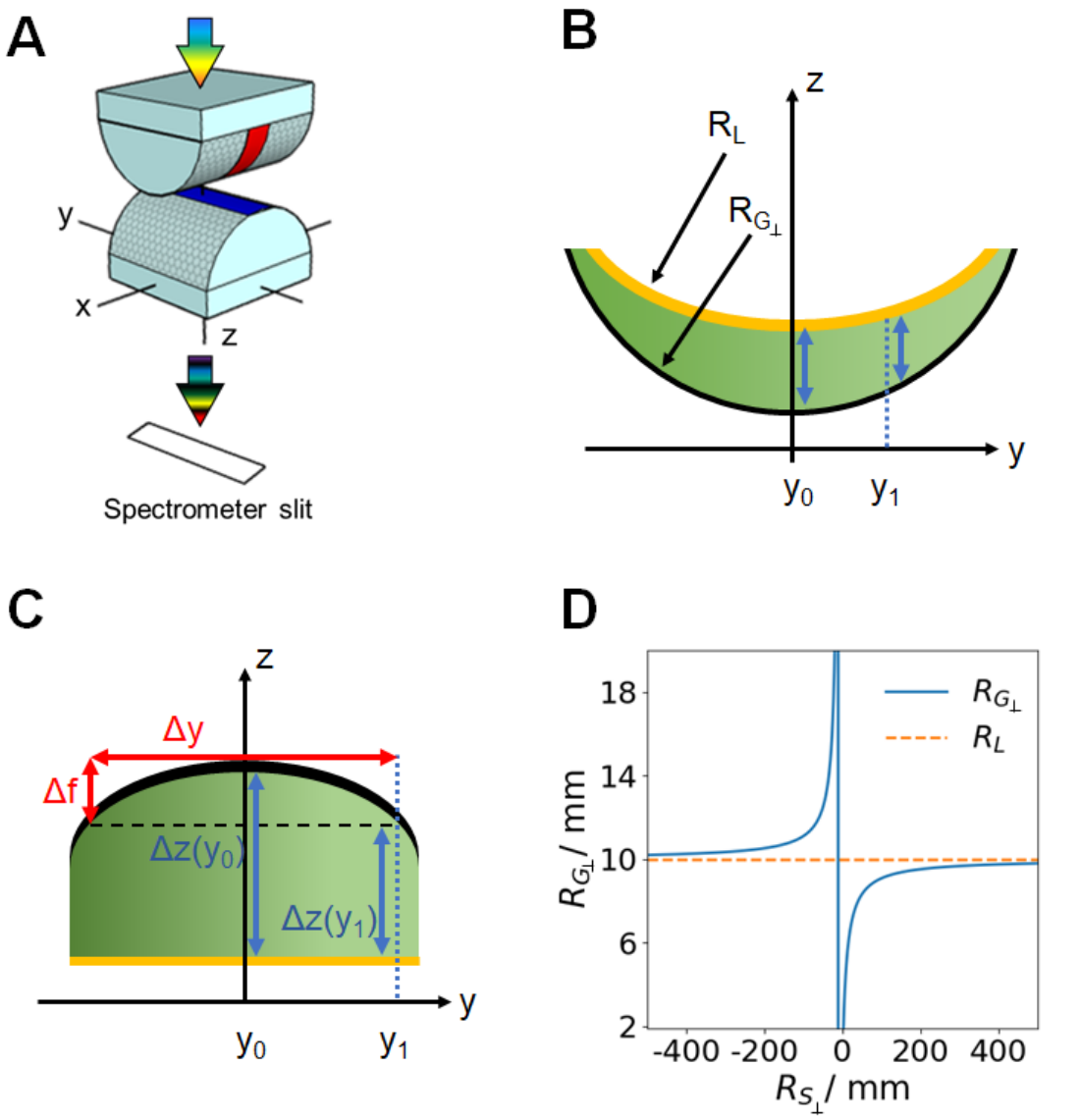


Figure 4.4: *The relationship between the secondary fringes and the surface radius of curvature R_G. (A) Orientation of the surfaces with respect to the spectrometer slit. Two distinct sets of secondary FECO are visible. In the orientation shown, one set of secondary fringes, $R_{S\|}$, shows as vertical lines in the interferogram (not shown) and corresponds to the negligible thickness non-uniformity of the epoxy layer on the lower lens highlighted in blue, parallel to the apex of the lens (y-axis). The other set of fringes, $R_{S\perp}$ corresponds to the thickness non-uniformity of the epoxy layer on the upper lens highlighted in red, perpendicular to the lens apex (x-axis). (B,C) Models used to account for the difference between the radius of curvature of the lens, R_L and radius of curvature of the top graphene surface in the orientation shown in A (red), $R_{G\perp}$. The height difference between the graphene surface (black line) and the gold mirror (yellow line) describes and arc with radius $R_{S\perp}$. (D) $R_{G\perp}$ as a function of $R_{S\perp}$, with $R_L = 10$ mm. For the large values of $R_{S\perp}$ used in experiments, $R_{S\perp} \to \infty$, and $R_{G\perp} = R_L$.*

An analytical expression relating $R_{S\perp}$ to $R_{G\perp}$ can be derived as follows. For two circles with radius R_L and R_G, with their centers at $(0, b_L)$ and $(0, b_G)$ (Figure 4.4-B):

$$z_L = \sqrt{R_L^2 - y^2} + b_L \tag{4.7}$$

$$z_{G\perp} = \sqrt{R_{G\perp}^2 - y^2} + b_{G\perp} \tag{4.8}$$

Since $(y_1 - y_0) = \Delta y \ll R_L$, a second order Taylor expansion around $(y_0 = 0)$ can be used to give:

$$z_L = R_L - \frac{y^2}{2\,R_L} + b_L \tag{4.9}$$

$$z_{G\perp} = R_{G\perp} - \frac{y^2}{2\,R_{G\perp}} + b_{G\perp} \tag{4.10}$$

Where the profile of the height variation giving rise to the secondary fringe is:

$$\Delta z = z_{G\perp} - z_L = \frac{y^2}{2}(\frac{1}{R_L} - \frac{1}{R_{G\perp}}) + (R_{G\perp} - R_L) + (b_{G\perp} - b_L) \tag{4.11}$$

To determine the radius of curvature $R_{S\perp}$ of the secondary fringe, the same method is used as for the primary fringe (see equation 4.6). Recognizing:

$$\Delta y = 2y_1 \tag{4.12}$$

$$\Delta f = (\Delta z(y_0) - \Delta z(y_1)) = \frac{y_1^2}{2}(\frac{1}{R_L} - \frac{1}{R_{G\perp}}) \tag{4.13}$$

and since y_1 (generally hundreds of microns) $\gg \Delta f$ (generally a few micron) the second term of equation 4.6 may be neglected to give:

$$R_{S\perp} = \frac{\Delta y_1^2}{8\,\Delta f} \tag{4.14}$$

$$R_{S\perp} = -\frac{(2y_1)^2}{8(\frac{y_1^2}{2}(\frac{1}{R_L} - \frac{1}{R_{G\perp}}))} \tag{4.15}$$

$$R_{S\perp} = -\frac{R_{G\perp}R_L}{R_{G\perp} - R_L} \tag{4.16}$$

So that $R_{G\perp}$ depends on the directly measurable values of $R_{S\perp}$ and R_L as:

$$R_{G\perp} = \frac{R_{S\perp}R_L}{R_L + R_{S\perp}} \tag{4.17}$$

Figure 4.4-C shows the relationship between $R_{G\perp}$ and $R_{S\perp}$. As expected, in the limit ($R_{S\perp} \to \pm\infty$), $R_{G\perp} = R_L$. Further, only for values of $-400\,mm < R_{S\perp} < 400\,mm$ does $R_{G\perp}$ significantly deviate from R_L.

Figure 4.5-A shows an experimental interferogram for an epoxy layer fabricated by indirect spin coating from acetone (section 3.2). $R_{S\|}$ is visible as a broad horizontal band. $R_{S\perp}$ is visible as two arcs that lie with their apex towards the blue end of the spectrum. The strong resemblance between the experimental interferogram and one calculated using the measured value for $R_{S\perp}$ (Figure 4.6-B) shows the accuracy of the model. Using the measured value for $R_{S\perp} \simeq$ -210 mm in equation 4.17 gives $R_{G\perp} = 10.5$ mm. For the surfaces used in this work $0.9 < R_L/R_{G\perp} < 1.1$.

After determination of $R_{G\perp,1}$ of one of the surfaces, the light entering the spectrometer slit was rotated by 90 degrees using a dove prism. This allows for determination of $R_{G\perp,2}$.

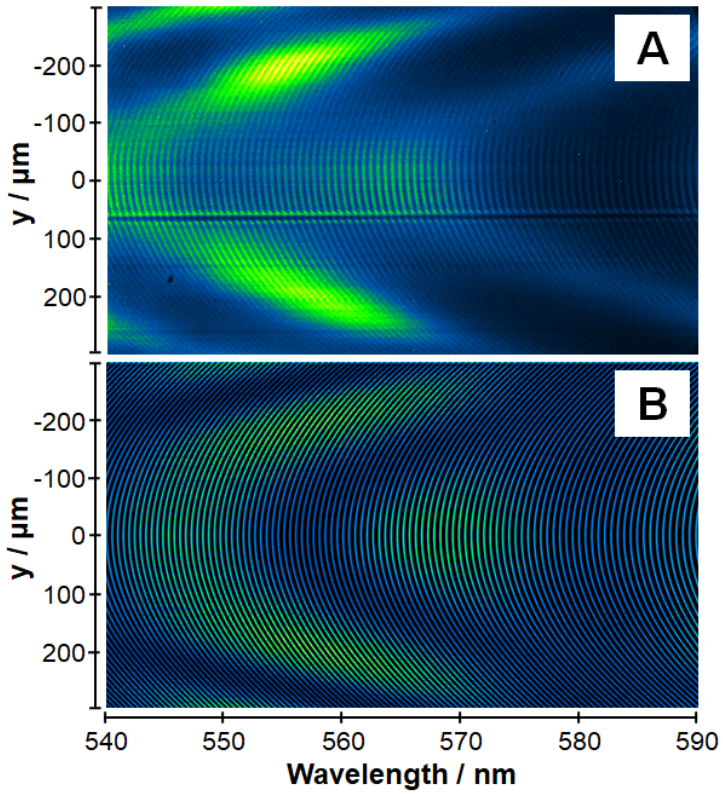


Figure 4.5: *(A) Experimental interferogram. The closely spaced curved lines correspond to the primary fringes. The thin dark horizontal line is produced by a speck of dust in the light path. The two large parabolic bands correspond to the secondary fringes used to determine* $R_{S\perp}$*. The horizontal band at 550 – 560 nm is the secondary fringe corresponding to* $R_{S\parallel}$*. (B) Interferogram calculated using the value for* $R_{S\perp}$ *measured from the experimental interferogram shown in (A).* Adapted with permission from C.D. van Engers *et al.*, Nano Letters 2017, 17, 3815–3821 [143]. Copyright (2017) American Chemical Society.

The effective radius of curvature R_G is the geometric mean of both values and reflects the curvature of the ellipsoid on flat ($R_{G\perp,1} \neq R_{G\perp,2}$) or sphere on flat ($R_{G\perp,1} = R_{G\perp,2}$) [12]:

$$R_{G\perp} = \sqrt{R_{G\perp,1}\, R_{G\perp,2}} \tag{4.18}$$

The determination of R_L is performed by inspection of the primary fringes in each of the slit configurations, and used for the determination of $R_G\perp$ separately. This is unlike the determination of $\mathbf{R}$ in conventional mica SFB experiments, where both measured values for the radius of curvature should be put into equation 4.18 (although the latter

procedure is often neglected in mica SFB experiments and is expected to introduce error, in particular when thin mica sheets are used!).

When the epoxy spacer is fabricated via indirect spin-coating from EtAc (section 3.2), the resulting layer is often so uniform in thickness, that determination of $R_{S\perp}$ is not possible. In this case $R_{G\perp} \simeq R_L$. Figure 4.6-A shows an interferogram with such a secondary fringe pattern, where $R_{S\perp} \simeq R_{S\parallel}$. To make the secondary fringe patterns clearer, Figure 4.6-B shows an interferogram during which the surfaces were moved whilst recording an image with long exposure time on the CCD camera. As was pointed out by Heuberger [141], this averages out the distance dependent primary fringes (**P(D)** in Figure 4.1) leaving only the secondary fringes. Figure 4.6-C shows another interferogram for which $R_{S\perp} \simeq R_{S\parallel}$. An interferogram recorded using the conventional mica SFB is shown for reference in Figure 4.6-D. It is thus clear that using the indirect spin-coating method outlined in section 3.2 results in uniform surfaces for which $R_{G\perp} \simeq R_L$ and the conventional method for the determination of **R** can be used.

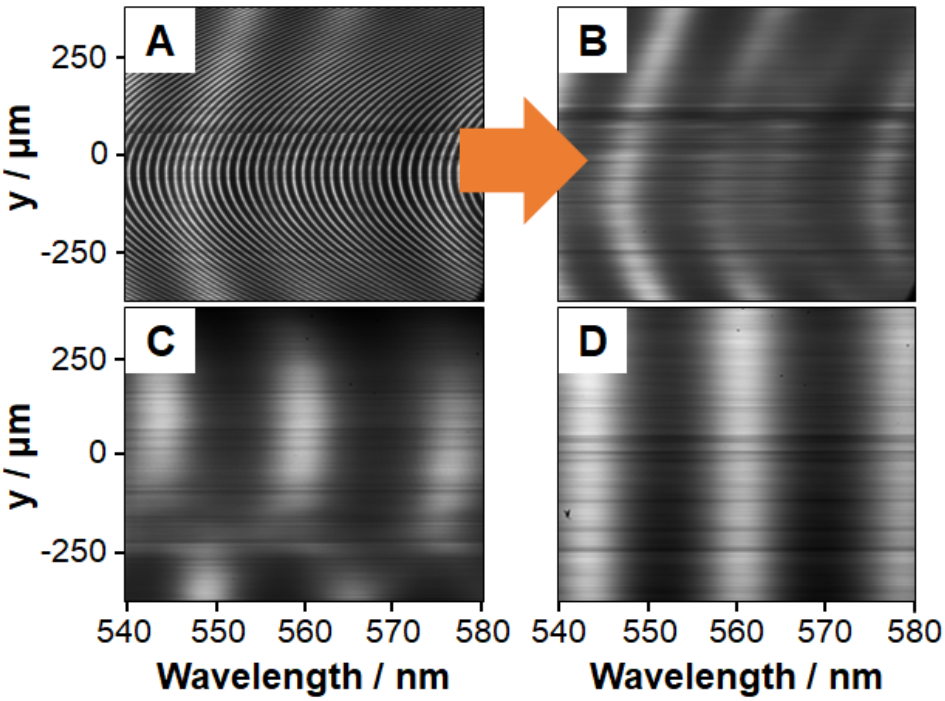


Figure 4.6: *Interferograms showing secondary fringe patterns of gSFB lenses prepared using the indirect spin-coating method described in section 3.2. (A) Interferogram recorded with the surfaces at rest. (B) Same interferogram as shown in (A), now recorded with surfaces in motion. Moving the surfaces whilst recording an image with long exposure time on the CCD camera results in averaging out of the distance dependent primary fringes and leaves only the secondary fringes. Two sets of secondary fringes are visible, one set is slightly more curved than the other. (C) Another "averaged" interferogram recorded with the surfaces in motion. Here both sets of secondary fringes are almost vertical and overlap. (D) Averaged reference interfergram showing mica fringes.*

4.3 Contact-free calibration

This work was performed in collaboration with a post-doc in our group, Dr. Marco Balabajew, and published in 2017 [144].

4.3.1 Introduction

The analysis of interferometric data recorded during an SFB experiment typically involves a contact calibration (see section 4.1.1). For example, for the analysis of an asymmetric interferometer in which the thicknesses of the spacer layers $\mathbf{Z1} \neq \mathbf{Z2}$ (see Figure 4.1), first the total thickness $\mathbf{Z1} + \mathbf{Z2} = \mathbf{Z_{Total}}$ is determined by numerically fitting the contact fringe positions. Subsequently, the surfaces are separated by a small amount and the FECO positions are numerically fit again. As will be discussed in Chapter 5, the graphene surfaces were often found to be unstable with respect to performing a contact calibration. Therefore it was necessary to develop a novel method for analyzing the obtained interferometric data.

Heuberger developed a method for efficiently fitting the contact fringe positions by comparing the sum of intensities between the experimentally measured peak positions, and those calculated using the MMM as a correlation function. This method effectively minimizes calculation time by only considering values for λ around the peak position. The resulting correlation function exhibits many local maxima at different parameter combinations (generally n or z for one or more of the layers, see equation 4.3). The maxima of this correlation function are equivalent to local minima of sum of squared residuals in conventional fitting approaches and prevent the optimal solution to be reliably found by conventional fitting algorithms. It is therefore necessary to perform brute-force searches to find the optimal fit to the experimental data [137].

The computational cost of using brute-force searching procedures limits the degrees of

freedom or parameter space (Ξ). For a conventional mica setup, for which the mica spacers are of equal thickness and only the total thickness needs to be fitted, $\dim(\Xi) = 1$. In the asymmetric case there a two principle parameters, $\mathbf{Z_{Total}}$ and a parameter accounting for the asymmetry. Since the asymmetry can not be determined in contact, a fringe pattern must also be recorded with the surfaces slightly out of contact. Thus in addition to $\mathbf{Z_{Total}}$ and the asymmetry, a pseudo-parameter - the thickness of the gap - is used (**D** in Figure 4.1), and $\dim(\Xi) \simeq 2$. When the spacers are not of equal thickness and the surfaces may not brought into contact, **Z1**, **Z2** and **D** are all fully free parameters, and $\dim(\Xi) = 3$. Whilst for the first two scenarios a solution may be found within reasonable computation time, running through the vast parameter space to find a solution in the case of $\dim(\Xi) = 3$ is computationally unaffordable.

This section describes a "contact-free" calibration method applicable to the gSFB setup. This contact-free calibration method relies on using the secondary fringe profile to find suitable initial parameters for **Z1** and **Z2**, which greatly reduces the parameter space. Further, a three-step procedure for performing such a calibration and a proof-of-principle measurement of the structure of an ionic liquid confined between mica sheets of unequal thickness using a contact-free calibration will be presented.

4.3.2 Materials & Methods

Experimental Setup

Experiments were performed using the conventional mica SFB setup. A charge-coupled device (CCD; Retiga R6, QImaging) was used to record the interference fringes. The conversion factor to calculate wavelengths from pixel positions was obtained by measuring the positions of mercury emission lines. Muscovite mica (Ruby Mica Grade #1 V-1/V-2, S&J Trading Inc) was cleaved to obtain mica sheets corresponding to a single facet of 2.5 – 7.0 μm in thickness and placed on a freshly cleaved thick mica plate as support

and back-silvered (Silver shot, 99.9999%, Alfa Aesar) using an HHV Auto306 (HVV Ltd) thermal evaporator.

The (mica) SFB lenses were prepared by gluing the mica sheets silver side down onto hemi-cylindrical quartz lenses using paraffin wax (melting point = 53–57°C ASTM D87, Aldrich Chemistry). Gluing at 70°C with as little paraffin as possible and slowly cooling to the freeze-melt transition was necessary due to the slight contraction of the paraffin upon solidification. The ionic liquid, 1-Ethyl-3-methylimidazolium bis(trifluoromethylsulfonyl)-imide ($[C_2C_1Im][NTf_2]$) (99%) was obtained from IOLITEC ionic liquids technologies GmbH and dried under moderate vacuum (5×10^{-3}mbar) at 80°C overnight.

Experimental Procedure

Two pairs of lenses, each set consisting of mica sheets of equal thickness, were prepared. Both sets were separately mounted into the SFB and their fringes recorded. In this symmetric configuration, the mica sheets are of equal thickness so that **Z1** = **Z2** and the secondary fringes overlap (**S1** = **S2**). To obtain the secondary fringe patterns, secondary fringes were recorded at large **D** whilst moving the surfaces using a long exposure time for the CCD camera, as outlined in section 4.2 (see Figure 4.6). Subsequently, the surfaces were brought into contact and the primary fringes were recorded.

Next, one lens of each set was used to form an asymmetric configuration. For the asymmetric set, secondary and primary contact fringes were recorded again. In addition, primary fringes were recorded at moderate distance, having $\sim$ 20 fringes between the mercury reference lines.

In an independent experiment performed according to the same procedure, a set of lenses with mica sheets (**Z1**$\neq$**Z2**) was prepared. After recording secondary fringes and primary fringes at moderate distance, $[C_2C_1Im][NTf_2]$ was injected in between the surfaces. Then, the surfaces were slowly brought into close contact to measure the structural

forces arising from the squeeze out of anion/cation layers in close confinement [145]. Experiments were performed in N_2 atmosphere. During the experiment a small cup of P_2O_5 was placed in the chamber as desiccant.

Data analysis & Fitting

For fitting the positions of the primary fringes we used a method introduced by Heuberger [137]. This technique uses the sum of intensities at the measured peak positions, calculated by the multilayer matrix method as a correlation function, to describe similarity between the measured and calculated interference patterns and is chosen to minimize calculation time. This correlation function exhibits many local maxima at different parameter combinations [137]. The maxima of this correlation function are equivalent to local minima of sum of squared residuals in conventional fitting approaches and prevent the optimal solution to be reliably found by conventional fitting algorithms. Therefore, a brute-force search was used to find the optimal fit. For fitting the secondary fringe profiles a conventional sum of squared residuals was used as correlation function in combination with a brute-force search to find the optimal fit. The procedure to calculate the theoretical secondary profiles is described in detail later.

Optical constants for silver and mica were taken from McPeak [142] and Kienle [146]. All computations were performed on a desktop computer (OptiPlex 7040, Dell) with an Intel Core i5-6500 CPU (3.2 GHz), 16 GB RAM and Windows 7 Enterprise 64-bit. The fitting software was home-written utilizing Armadillo as library for linear algebra.

4.3.3 Results & Discussion

Index matching the glue layer and underlying cylindrical quartz lens

The optical stack considered for the multilayer matrix method calculations for the mica SFB setup generally has the form: [*glue*|silver|mica1|medium|mica2|silver|*glue*]. During

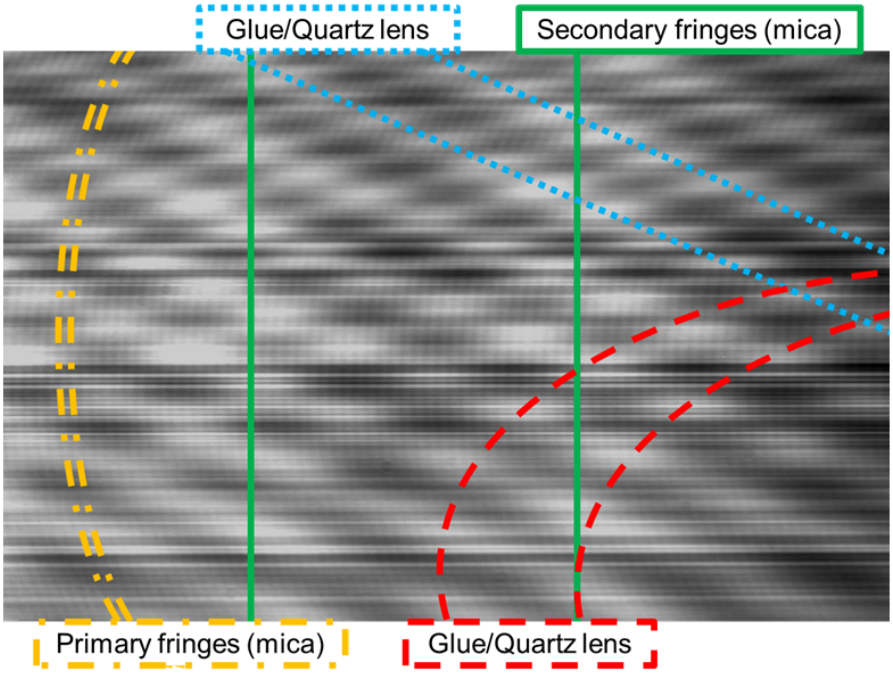


Figure 4.7: *Interferogram recorded using an asymmetric mica SFB setup corresponding to* [*EPON*|silver|mica1|air|mica2|silver|*EPON*]. *The cylindrical quartz lens and the epoxy (EPON1004F) used to glue down the back-silvered micas are not index matched. This results in the observation of additional fringe patterns arising from reflections between the glue*|silver *and the underlying* quartz|*glue interface.*

the calibration the medium is air. EPON1004F, a hard thermoplastic epoxy commonly used in SFB experiments, with refractive index $n_{EPON} \simeq 1.55$, was initially used as the glue layer. However, it was found that in asymmetric configuration, reflections between the *glue*|silver and the underlying quartz|*glue* interface resulted in additional fringe patterns (see Figure 4.7). To prevent the interference due to these additional reflections, paraffin was used. Paraffin is index matched with the cylindrical quartz lens so that $R^*_{Glue,\,Quartz\,lens} \rightarrow 0$ and no additional fringe patterns are observed.

Describing the secondary fringes

By matching the refractive index of the glue and the cylindrical quartz lens, the secondary fringe patterns (**S1** and **S2** in Figure 4.1) could be recorded without the presence of artifacts arising from reflections outside the optical stack. The secondary fringes were recorded by having a long exposure time for the CCD camera whilst moving the surfaces

as suggested by Heuberger [141] (see Figure 4.6). This approach, which averages out the contribution of the distance dependent (primary) fringes, is simple to implement experimentally. However, calculating an interference spectrum via averaging over a large amount of individual spectra - which mimics the experimental approach, is computationally expensive.

Rather than averaging the result from multiple multilayer matrix calculations using the 5-layer optical stack [*paraffin*|silver|mica1|air|mica2|silver|*paraffin*], the secondary fringes originating from one of the mica spacers can be calculated using a single calculation of a 2-layer stack with [*paraffin*|silver|mica1|*air*]. Figure 4.8 shows a comparison between a single symmetric 5-layer interference spectrum (black dots), a spectrum resulting from averaging multiple of such spectra with a slightly different value of **D** (red line), and a spectrum of the 2-layer optical stack (blue dashes). The averaged 5-layer and single 2-layer spectra are almost identical and the small difference between them arises due to the absorbance of the silver layer.

The 2-layer method provides a computationally efficient way to calculate the expected secondary fringes from one of the (mica) spacers. However, simply summing two such spectra for the asymmetric case does not reliably predict the secondary fringe profile. Born & Wolf (paragraph 7.6.8., pg. 360) [136] provides an analytical result to predict the transmittance through two parallel plates at large distance. The transmitted intensity ($I_{Transmitted}$) through a single slab surrounded by a medium of refractive index n, known as Airy's equation, is:

$$\frac{I_{Transmitted}}{I_{Initial}} = \Big(\frac{T^*}{1-R^{*2}}\Big)^2 \Big(\frac{1}{1+F\sin^2(\delta \div 2)}\Big) \tag{4.19}$$

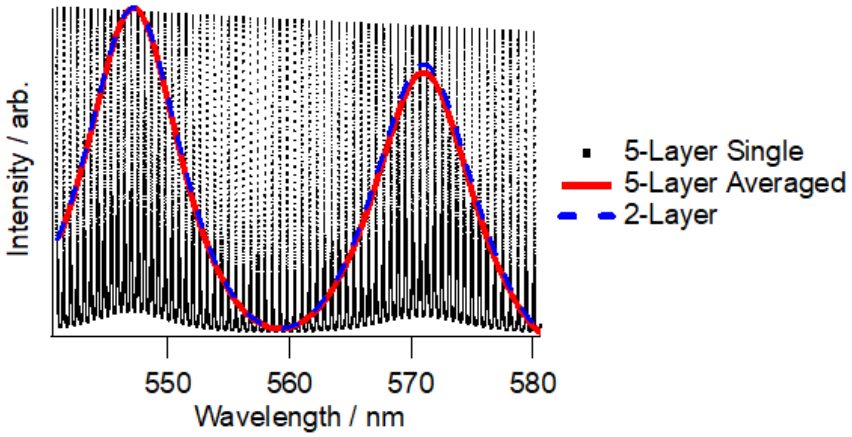


Figure 4.8: *Interference spectra comparing different methods to calculate the secondary fringes. The single (symmetric) 5-layer calculation of the* [*EPON*|silver|mica1|air|mica2|silver|*EPON*] *optical stack is shown in black dots. The secondary fringes appear as elevated background underneath the primary fringes. The red line shows the spectrum resulting from averaging multiple of such calculations at a slightly different value of* ***D****. The spectrum calculated for a single 2-layer calculation of the* [*paraffin*|silver|mica1|*air*] *optical stack is shown as the dashed blue line. The correspondence between the averaged 5-layer and single 2-layer results is remarkable, with the different arising due to the absorption in the silver layer. To increase the visibility of the secondary fringes in the single 5-layer calculation* $n_{Ag,figure} = n_{Ag} + 0.5$ *was used.* Adapted from M. Balabjew*, C.D. van Engers* *et al.*, Review of Scientific Instruments 2017, 88, 123903 [144]. Copyright (2018) AIP Publishing LLC.

where $I_{Initial}$ is the intensity of the incoming light, T^* is the transmittance at the interface (equal to $1 - R^*$ for non-absorbing materials), F is the finesse, defined as:

$$F = \frac{4R^*}{(1 - R^*)^2} \tag{4.20}$$

and δ is defined as:

$$\delta = \frac{4\pi nT}{\lambda} + 2\phi \tag{4.21}$$

where T is the thickness of the slab, λ is the wavelength and ϕ is the phase shift upon reflection. The second part of equation 4.19 governs the pattern in the transmitted light. The reflection for two such slabs at large distance is product for the transmitted intensity

through two such slabs [136], so that the total secondary fringe profile (I_{S1+S2}) is the product of the individual secondary fringe intensities ($I_{S1,S2}$):

$$I_{S1+S2,\,Airy} = I_{S1} I_{S2} \tag{4.22}$$

Figure 4.9 shows the sum of squared residuals (SSR) between a secondary fringe profile of the averaged 5-layer calculation and two 2-layer calculations for which the secondary fringe profiles were "summed" using equation 4.22. This method will be referred to as the "Airy" method. The SSR value was calculated having the thickness of the spacer layer mica1 fixed at **Z1** = 5μm, and spacer layer mica2 ranging from **Z2** = 3 - 6 μm. The high SSR values imply a poor match between the averaged 5-layer calculation and the values obtained using the Airy method. Therefore, several other "summing" methods were investigated.

The other summing methods attempted were strictly empirical. The second method uses the normalized summed intensity of the 2-layer profiles and will be referred to as "sum":

$$I_{S1+S2,\,sum} = I_{S1} + I_{S2} \tag{4.23}$$

The third method considers the reciprocal sum of the two and will be referred to as "reciprocal":

$$I_{S1+S2,\,reciprocal} = \left(\frac{1}{I_{S1}} + \frac{1}{I_{S2}}\right)^{-1} = \frac{I_{S1} I_{S2}}{I_{S1} + I_{S2}} \tag{4.24}$$

The forth method was derived from equation 4.22. However, it considers the product of only the second part of equation 4.19 (which accounts for the transmitted light pattern)

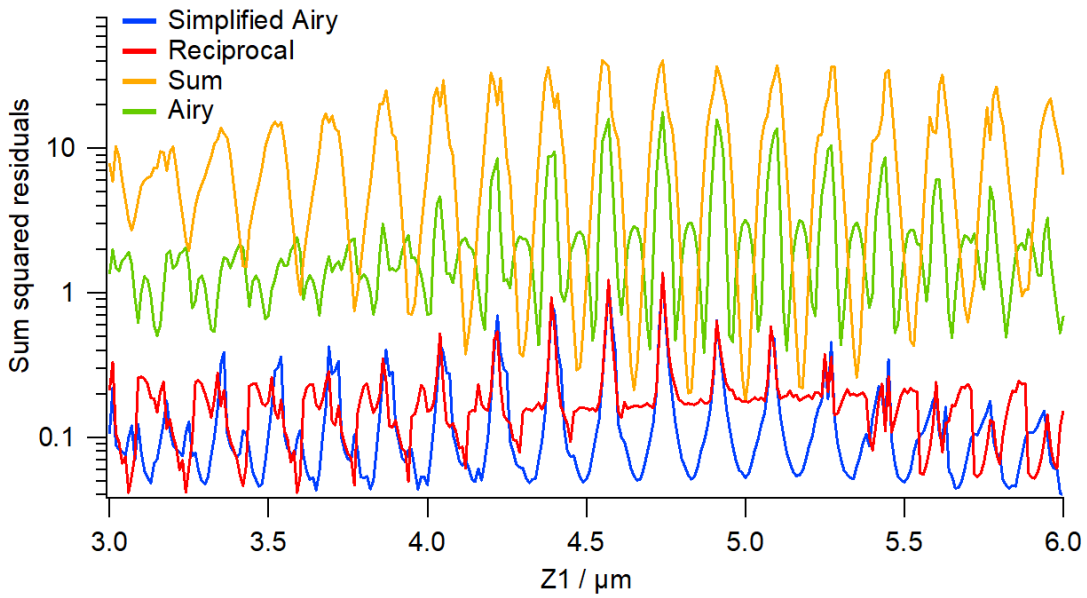


Figure 4.9: *Log-normal plot of sum of squared residual showing the performance of different summing methods as compared to the spectra calculated via averaging as a function of the thickness of one of the mica spacers,* ***Z1****. The thickness of the other mica spacer was kept constant at* ***Z2*** *= 5 µm. High values correspond to poor fits. The worst fits for the simplified Airy method arise when the secondary fringe patterns of the two two-layer calculations are out of phase.*

but neglects the fourth term in the denominator. It will be referred to as the "simplified Airy" method:

$$I_{S1+S2,\,simplified\,Airy} = \frac{1}{1 + F_1 \sin^2(\delta_1 \div 2) + F_2 \sin^2(\delta_2 \div 2)} = \frac{I_{S1} I_{S2}}{I_{S1} + I_{S2} - I_{S1} I_{S2}} \quad (4.25)$$

Figure 4.9 shows that the simplified Airy method (equation 4.25) outperforms the other summing methods attempted. The reason for this is not clear. However, the analytical solution presented in equation 4.19 assumed that the refractive index around the slab is uniform, which is not the case in the optical stack considered here. Further, it does not account for the absorption of light.

The use of a suitable summing method for individual secondary fringes, allows the full asymmetric secondary fringe profile to be calculated at much smaller computational cost compared to averaging a full 5-layer calculation. As such, the obtained experimental

secondary fringe profile can be fitted to the sum of two secondary fringes representing **Z1** and **Z2**.

Contact-free calibration

The analysis procedure with contact-free calibration was demonstrated in a proof-of-principle measurement on the interfacial structure of $[C_2C_1Im][NTf_2]$ using an asymmetric mica SFB setup. The general workflow of the data analysis is illustrated in Figure 4.10. It consists of three major steps:

1. Initial guesses for the (mica or epoxy) spacer thicknesses are obtained from the secondary fringe profiles as described in section 4.3.3.

2. The initial guesses are refined by fitting primary fringes measured at a moderate distance using Heuberger's method [141].

3. The obtained spacer thicknesses are used to evaluate the performed experiment.

The red line in Figure 4.11 shows the extracted secondary fringe profile. Subsequently, a sum of two [*glue*|silver|mica|*air*] calculations, with thicknesses **Z1** and **Z2** as fitting parameters, was fitted to the experimental profile using the simplified Airy method. The fit (dashed blue line) shows good agreement with the experimental data and provides good starting parameters for further refinement of **Z1** and **Z2**.

Underneath the experimental profile and fit, the fringe profiles for the fitted thickness are shown (black dash-dot line) next to their experimental counterparts, which were measured in symmetrical configuration. The fits show excellent agreement and deviate only by 3.7 nm for one fringe profile and by 171.2 nm for the other. The larger difference of the latter corresponds to the distance between two consecutive fringe orders, which satisfies the condition:

$$d_{fringe\,orders}(\lambda) = \frac{\lambda}{2n_{spacer}} \tag{4.26}$$

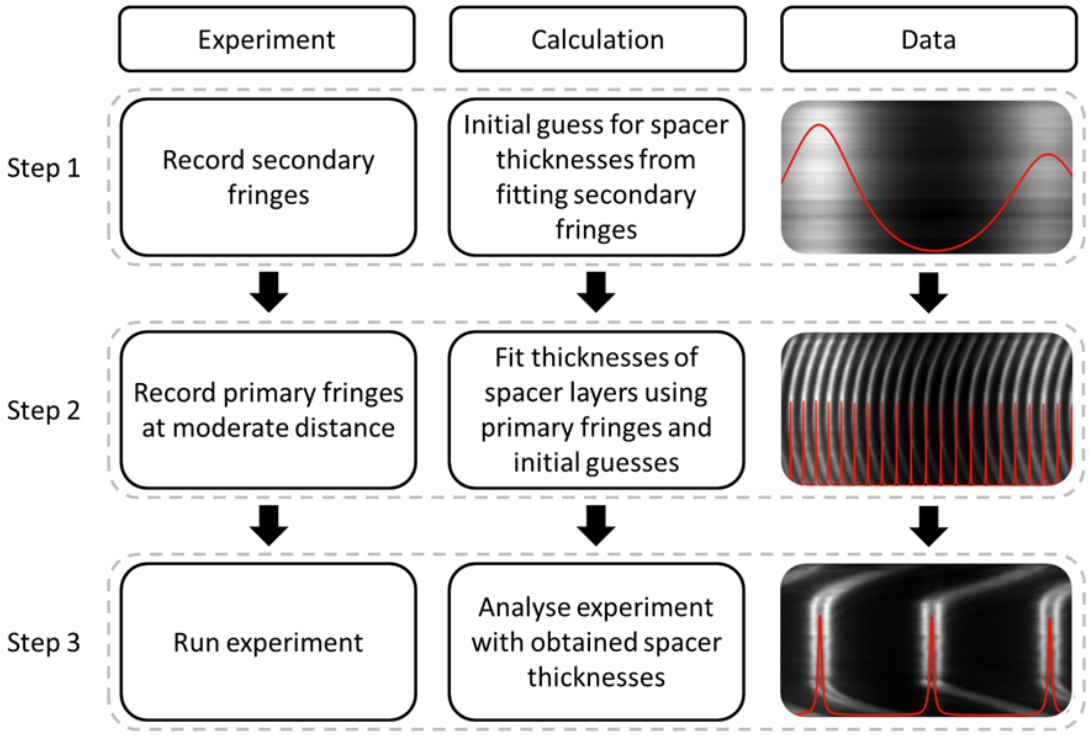


Figure 4.10: *Flow diagram demonstrating the steps involved in the contact-free calibration method. Step one: the secondary fringe traces are recorded at large surface separation while moving the surfaces and fitted to calculated spectra. Step two: Primary fringes are recorded at moderate surface separation. The values obtained in step 1 are used as input parameters for a brute-force search to match the experimental primary fringes with calculated spectra. Step three: The data collected during the experiment can be analyzed. The surface separation* ***D*** *is calculated for approaching surfaces, using the spacer thicknesses found in step 2 and without the need for a contact calibration.* Adapted from M. Balabajew*, C.D. van Engers* *et al.*, Review of Scientific Instruments 2017, 88, 123903 [144]. Copyright (2018) AIP Publishing LLC.

For the wavelength range of interest in this experiment ($\lambda \simeq 540$ nm – 585 nm) this equates to $d_{fringeorders} \simeq 169$ nm – 183 nm. Across experiments, the secondary fringe fitting always found the correct value within a few nanometers or within a few nanometers plus/minus one fringe order. After the initial parameters for **Z1** and **Z2** have been found, they are further refined along with determination of **D** in step two.

To obtain **D** and find more accurate values for **Z1** and **Z2** a primary fringe pattern is recorded at moderate distance, where the secondary fringes have a clear effect on the primary fringes (see Figure 4.2) and the large number of primary fringes provides sufficient peaks to perform a reliable fit. This may be done in liquid, however, performing the

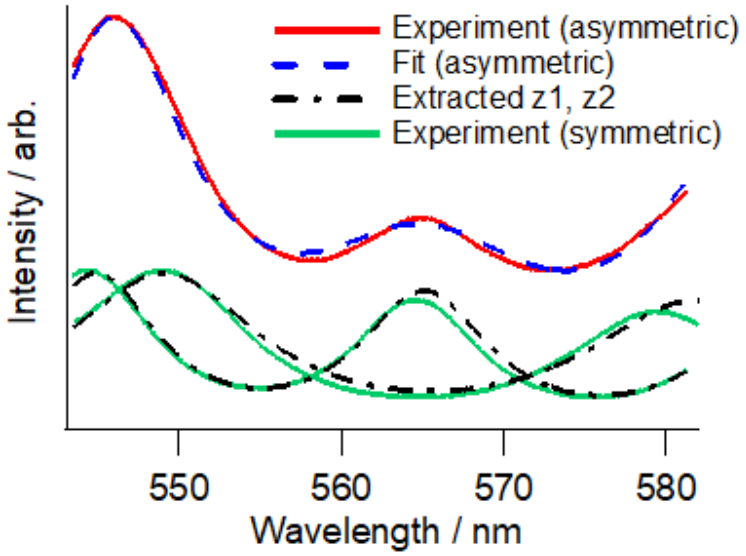


Figure 4.11: *Comparison of experimental data and secondary fringe fits. The red line shows the experimental secondary fringe trace obtained in asymmetric configuration. The fit to this data is shown in blue dashes and was obtained by summing calculated intensities* I_{S1} *and* I_{S2} *using equation 4.25. The dash dotted lines show how the values* I_{S1} *and* I_{S2} *used for the fit compare to the secondary fringe patterns obtained experimentally in symmetric configuration (solid green line).* Adapted from M. Balabajew*, C.D. van Engers* *et al.*, Review of Scientific Instruments 2017, 88, 123903 [144]. Copyright (2018) AIP Publishing LLC.

measurement in air provides a more reliable fit due to the difference in refractive indexes between air and the spacer. The evaluation of the fringe positions involves two steps. First a rough estimate for the gap thickness is obtained by fixing **Z1** and **Z2** to the initial guesses and fitting the positions of the primary fringes with the gap thickness **D** as fitting parameter. For the second step **Z1**, **Z2** and **D** are fitted simultaneously to the primary fringe profile. To fit **Z1** and **Z2** a reduced parameter space, based on the periodicity of suitable solutions (equation 4.26) is used. It was found that using a parameter range equal to ±1% of the initial guess (step one) and ±1% from the two adjacent fringe orders was sufficient. The range of **D** used should still be large; ±5% around the initial guess for this parameter.

In principle, in the case of an experiment involving a confined liquid the parameter space can be further reduced, as follows: The distance of closest approach during the

experimental runs is used for a pseudo-contact calibration assuming the gap thickness to be zero. Fitting the measured fringes with this assumption results in an approximate value for the sum of **Z1** and **Z2**, which is used as a constraint. The sum has to be within a certain range of the pseudo-contact position, so that the range contains the real contact position. In most cases a range of +1 nm (to account for noise in the pseudo-contact position) and -50 nm is sufficient to ensure finding the real contact position by performing the aforementioned final calibration.

Finally, step three is equivalent to a conventional analysis with multilayer matrix method to extract gap thicknesses [137].

Figure 4.12-A shows the primary fringe profile calculated after step two, (blue solid line) for the fitted mica thicknesses **Z1** and **Z2** and the fitted gap thickness **D**, in comparison with the measured experimental fringe pattern (spectrogram at the top) and extracted fringe positions (green dashed lines). The spectrum calculated on basis of the calculated layer thicknesses shows an excellent agreement with the experimental data.

Figure 4.12-B shows the fringe profile for the calculated fringe position ($\mathbf{D} = 0$, bottom, blue solid line). The calculated spectrum shows excellent agreement with the experimentally measured contact position (spectrogram on top and green dashed lines). The latter was measured to illustrate the accuracy of the method, but not used for in the contact-free calibration procedure.

The calculated fringe positions shown in Figure 4.12-B are red shifted by 0.057±0.017 nm compared to the measured fringe positions. However, in other comparable experiments blue shifted values were also measured. These errors may arise due to noise from the light source, systematic error that arises from re-focusing the light after injection of the liquid, the presence of an adsorbed layer of ambient gas or small differences in dispersion between the literature value and real value of both, the mica spacer, and the silver mirrors.

To demonstrate the applicability of the data analysis method, a force profile of the

ionic liquid $[C_2C_1Im][NTf_2]$ confined between two mica sheets of different thicknesses was recorded and analyzed in an independent experiment. Figure 4.12-C shows the measured force profile at small separations, analyzed according to the procedure described here and without reference to a contact calibration. It shows four distinguishable layers with a thickness of 0.73±0.03 nm. The thicknesses of the four observed layers are in excellent agreement with other studies [147, 148, 149, 150, 151]. Further, although a direct comparison between force magnitudes is not strictly informative due to the strong effect of small amounts of water on the interfacial structure [151], both the layer thicknesses and the magnitude of the forces measured agree well with other SFB measurements [150, 151]. This demonstrates the applicability of the presented method for measuring absolute distances without contact calibration.

The contact-free calibration method allows for the extraction of distances from the experimental interferograms within a single day on a desktop computer. This is a strong improvement from performing a brute-force search over the full three-dimensional parameter space spanned by **D**, **Z1** and **Z2**, for which calculation is estimated to take multiple weeks, and allows interpretation of experimental data obtained using the gSFB.

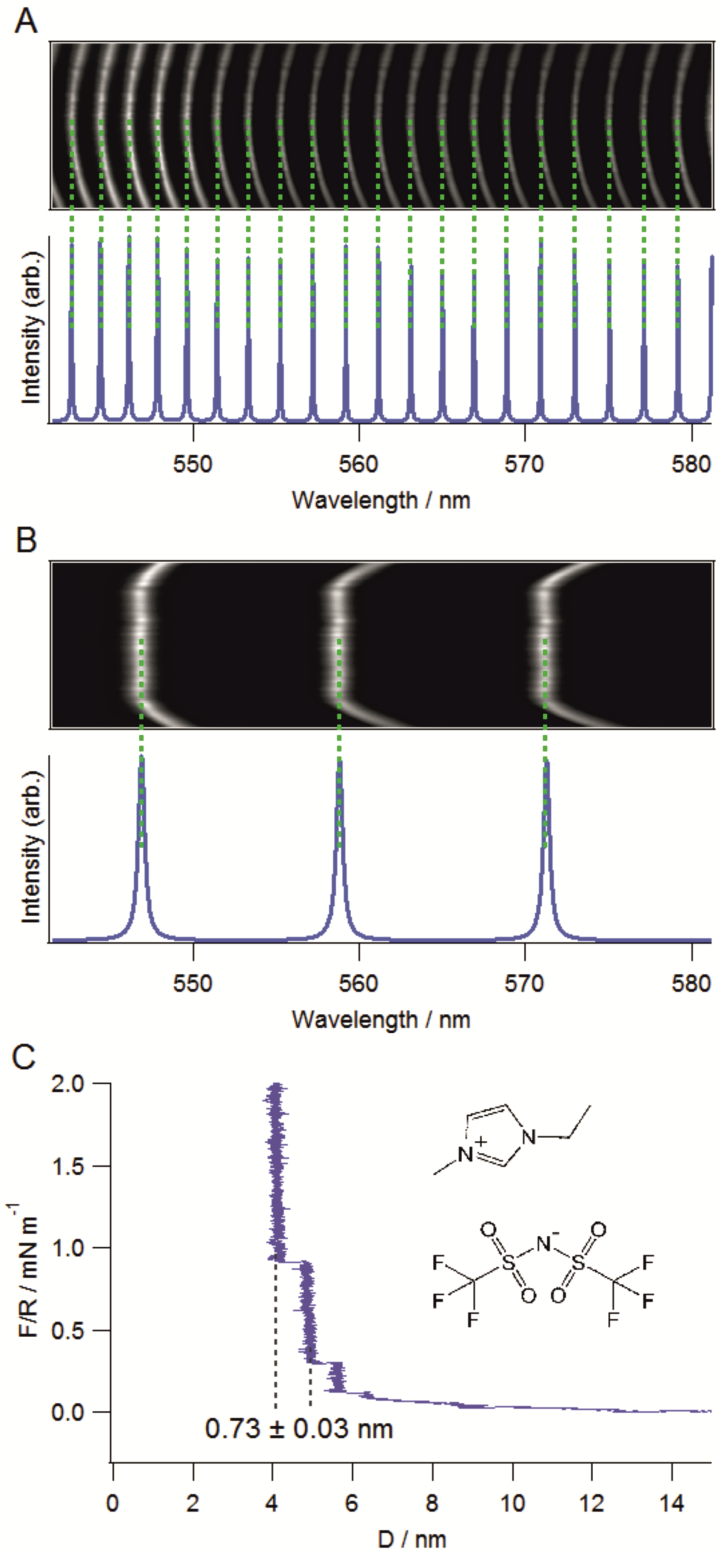


Figure 4.12: *Results of the fitting procedure and force profile of* $[C_2C_1Im][NTf_2]$ *between mica sheets. (A) Experimental interferogram showing primary FECO fringes obtained at moderate distance between the surfaces. The spectrum underneath corresponds to the fit. The dashed lines represent the fringe positions extracted from the measured FECO fringes. (B) Comparison between the experimentally determined contact position (not used to obtain the fit) and the calculated contact spectrum obtained through the fit in A. (C) Force profile of the structural forces arising from the layering of dry* $[C_2C_1Im][NTf_2]$ *anion/cation layers between mica surfaces.* Adapted from M. Balabajew*, C.D. van Engers* *et al.*, Review of Scientific Instruments 2017, 88, 123903 [144]. Copyright (2018) AIP Publishing LLC.

Chapter 5

Measurements using the Graphene Surface Force Balance

The successful fabrication of gSFB lenses and the ability to analyze the collected interferometric data as described in the previous chapters allowed for the measurement of surface forces at the graphene-graphene and graphene-liquid interface. In this chapter the first proof-of-principle experiments using the gSFB will be detailed. The first section in this chapter will describe measurements of the surface energy of graphene and interfacial energies between graphene and liquids. This work was published in 2017 [143]. The second section will discuss the outlook of performing future experiments using the gSFB.

5.1 Direct measurement of the surface energy of graphene

5.1.1 Introduction

The surface energy of graphene

Graphene has been defined as: a single-atom-thick sheet of hexagonally arranged, sp^2-bonded carbon atoms that is not an integral part of a carbon material, but is freely suspended or adhered on a foreign substrate [152]. Surface energy is defined as the free energy change γ when the surface area of some material is increased by unit area [87]. It also corresponds to half the work of cohesion, which is the work required for separating two of the same solids from contact to an infinite distance in vacuum (the work of cohesion is often referred to as the more general term work of adhesion, which formally represents the work required for separating two different materials). Thus, whilst defining a surface energy for a material that has no bulk seems odd, the definition is used with the framework provided: the surface energy of graphene refers to half the work required to separate two graphene sheets from contact to infinite distance.

Accessing the properties of graphene in devices, such as its electrical and mechanical performance [26], impermeability to liquids and gases [67], and optical transparency [153, 154], requires graphene to be in contact with other materials. Therefore, understanding and controlling the interfacial energies of graphene is important for the fabrication and operation of graphene-based technologies [155].

A variety of techniques have been used to measure the surface energy of *graphite* motivated by, for example, the fundamental interest in understanding London-van der Waals dispersion forces. Between these studies, liquid based techniques such as contact angle measurements, report much lower surface energy values than mechanical measurements (e.g. cleavage, sliding) [156]. The reason for this discrepancy is not clear. However, recent studies into the contact angle of water on graphite have revealed that in a large number

of contact angle studies adsorbed contaminants may have been present on the graphite surface [157]. Further, calculation of surface energies from contact angle measurements relies upon models such as the Owens, Wendt, Rabel, and Kaelble model (OWRK), which implicitly assume separability and additivity of polar and dispersive contributions. This assumption is expected to be invalid for a conductor with delocalized sp^2 electrons [158, 159]. Regarding graphene, an additional difficulty with respect to contact angle measurements is the potential influence of the underlying substrate [160].

Recent mechanical studies in which graphite mesas were manipulated using cantilevers have yielded values of 113±3 mJ/m^2 and 185±10 mJ/m^2 [161, 162]. Li *et al.* [163] and Wang *et al.* [164] have experimentally determined the adhesion energy of graphene to graphite, by pushing down a graphene beam onto an underlying graphite substrate and by studying the intercalation of noble gas atoms between graphene and a graphite substrate, measuring 154±21 mJ/m^2 and 110±5 mJ/m^2 as interfacial energies respectively. Theoretical work has predicted values for the surface energy of graphene to be in the range of 144 mJ/m^2 to 171 mJ/m^2 [165, 166, 167, 168].

Mica SFB measurements have been performed to directly determine the surface energy of the mica surface [169]. The lack of studies on graphene surface energy motivated a similar study using the gSFB.

Measurement of surface and adhesion energy using the (g)SFB

To determine the surface energy of graphene in the gSFB, the contact mechanics theory for surface energy and contact of elastic solids as put forth by Johnson, Kendall and Roberts (JKR-theory) is used [170]. JKR-theory is generally assumed to be valid for soft systems with large radius of curvature and high surface energy [171] as would be the case for the gSFB, and has been shown to apply to the (mica) SFB-setup [172, 169]. In a surface energy or adhesion force measuring experiment, the (graphene) surfaces are first brought

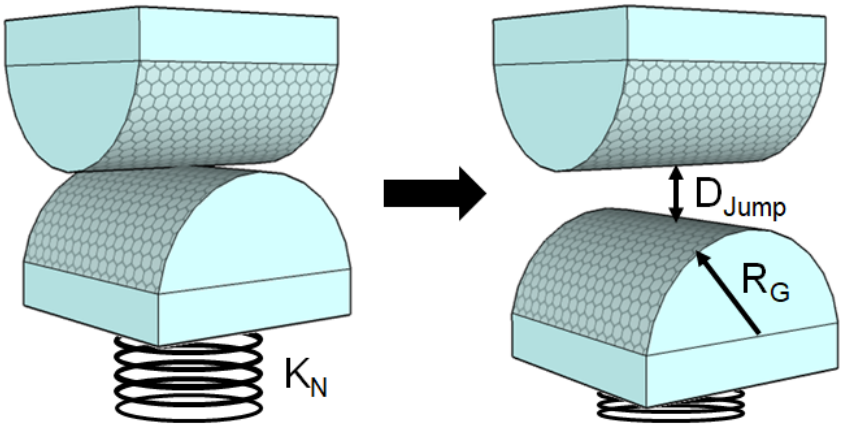


Figure 5.1: *Jump-out experiment performed to determine surface and adhesion energies. The surfaces are brought into adhesive contact (left) and gradually pulled apart by a spring with known spring constant K_N until they suddenly jump out of contact to a distance D_{Jump} (right). The pull-off force is equal to $K_N D_{Jump}$.*

into contact and then slowly pulled apart against the deflection of the normal spring with spring constant K_N until they seperate to a distance D_{Jump}.

Then, the pull-apart force corresponds to the product $F_{Adh} = -K_N D_{Jump}$. Using JKR-theory, the surface energy may be related to the adhesive force as:

$$\gamma_{JKR} = -\frac{F_{Adh}}{3\pi R_G} = \frac{K_N D_{Jump}}{3\pi R_G} \tag{5.1}$$

JKR-theory relates the surface energy γ to the radius of curvature of the surface R_G and adhesive force between the surfaces.

Figure 5.1 illustrates such a jump-out experiment. The advantage of the use of JKR-theory in combination with adhesion force measurements over other mechanical techniques for measuring surface energies is that it only assumes JKR-theory to be valid and does not rely on any other assumptions or complicated models. It thus provides a direct measurement of the surface energy of graphene.

5.1.2 Materials & Methods

The gSFB lenses were prepared as described in Chapters 2 and 3. The values of R_G were determined as described in section 4.2. The value of D_{Jump} was determined by fitting the primary fringe positions in contact and after the surfaces separate using Heuberger's method [137]. The thicknesses of SLG and FLG were assumed to be 0.33 nm and 1 nm, respectively. The experiments were performed in dry nitrogen or liquid.

Contact angles were measured on planar surfaces. The preparation procedure is similar to what is mentioned for the growth and transfer of graphene lenses, however, instead of an SFB lens, a 25 mm x 25 mm glass slide is used. Due to the use of a planar substrate, it was sufficient to directly spin-coat the epoxy layer. Static contact angle measurements were performed using a First Ten Angstroms 1000 Drop Shape Instrument (goniometer). For the measurement of the static contact angles, the mica was removed from the glass slide substrates in ultrapure water (revealing the graphene surface), dried on a hotplate and placed on the stage of the goniometer. Subsequently, 5 μL of ultrapure water was dispensed and carefully touched down to the surface on five different locations of the substrate. The average of these angles, which were all in very close agreement, was taken as the measured value.

Table 5.1 lists the materials, supplier and chemicals used (note that for the previously described preparation procedures the material's specifications are listed in their respective sections).

Table 5.1: Materials

Name	**Abbreviation**	**Supplier**	**Purity**
Ultrapure water	Water	Arium Pro Ultrapure	18.2 MΩ.cm, TOC <2 ppb
Sodium cholate hydrate	NaCh	Sigma Aldrich	≥99%

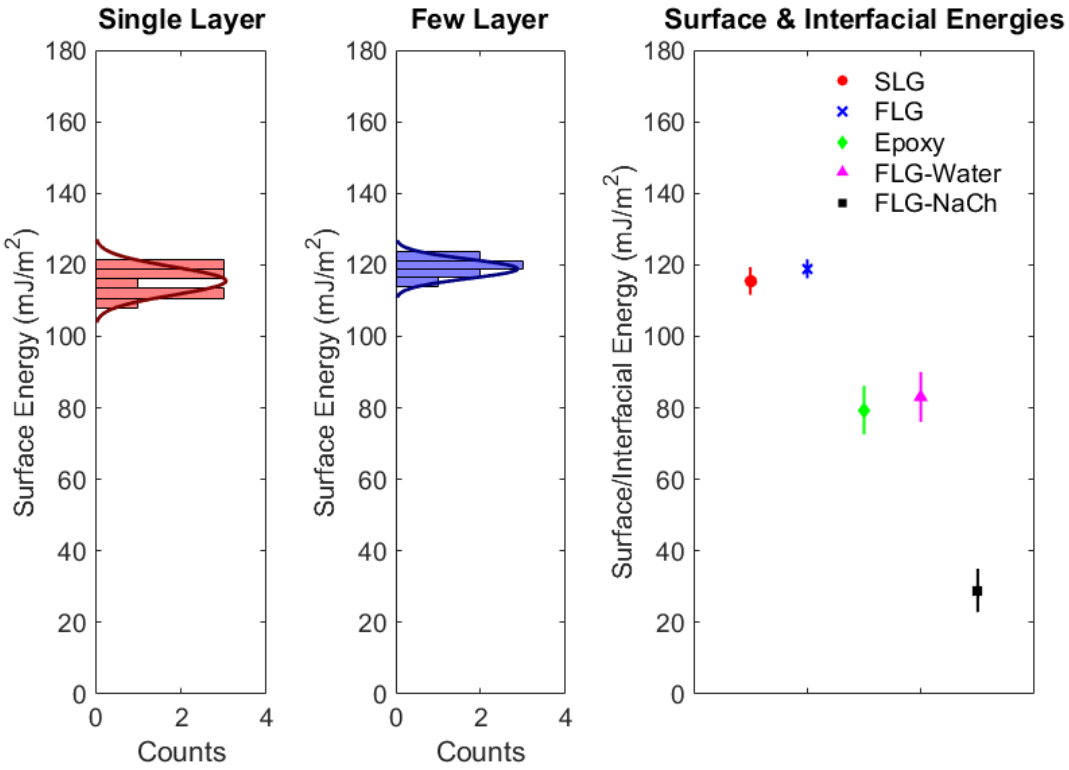


Figure 5.2: *Overview of measured surface and interfacial energies. The histogram and probability distribution to determine the mean and standard deviation for SLG and FLG are shown on the left panels. The right panel shows all measured surface and interfacial energies. The surface energies of SLG, FLG and epoxy were measured in dry nitrogen. Adapted with permission from C.D. van Engers et al., Nano Letters 2017, 17, 3815–3821 [143]. Copyright (2017) American Chemical Society.*

5.1.3 Results & Discussion

Figure 5.2 shows the results of the direct measurements of the surface energy of SLG and FLG graphene in dry nitrogen atmosphere. The surface energy of the underlying epoxy alone and the interfacial energies for graphene in water and aqueous solution of sodium cholate are also shown for comparison. Sodium cholate was chosen because it is a surfactant used as intercalant in the solvomechanical exfoliation of graphite to produce graphene [173].

The surface energies of FLG and SLG were found to be $\gamma_{FLG} = 119 \pm 3$ mJ/m^2 and $\gamma_{SLG} = 115 \pm 4$ mJ/m^2. These values represent the first direct measurements of

the surface energy of both few and single layer graphene. For consistency, each data point in the histogram in Figure 5.2 represents a measurement at a different location on the graphene-covered SFB lenses. Experiments were performed with different pairs of graphene-covered lenses. For FLG, eight different measurements were conducted using two different pairs of lenses; for SLG, it includes eleven different measurements over two different pairs of lenses.

The surface energies of FLG and SLG glued on the epoxy layers were significantly higher than the surface energy of bare epoxy, $\gamma_{Epoxy} = 79 \pm 7$ mJ/m^2. This calibration directly shows the significant contribution to the adhesion force and surface energy due the presence of the atomic layer (or layers) of graphene. We note that interactions between the polymer chains of the epoxy may influence the value measured for the surface energy of the epoxy but do not influence the value measured for graphene [174].

It is striking that the presence of a single layer of graphene was able to so substantially increase the cohesive force and surface energy of the graphene-coated epoxy with respect to the bare epoxy. For the epoxy, a nonconducting polymer, adhesion is due to the van der Waals interactions, which arise from correlated charge fluctuations in the molecular structure and are proportional to the (modest) polarizability of the polymer. In the case of graphene, consisting of a sp^2 hybridized layer with delocalized electron density in π-orbitals above and below the plane, the correlated charge fluctuations occurring when two graphene surfaces approach face-to-face, are expected to be much larger and thus lead to stronger adhesion. In general, the van der Waals forces between two bodies at small separation (e.g., in contact), covered with a surface film, is dominated by the interaction between the surface layers. Therefore, the presence of the graphene film governs the adhesion [87].

By separating the graphenes while fully immersed in water, the interfacial energy of graphene in water was found to be $\gamma_{Graphene-Water} = 83 \pm 7$ mJ/m^2. This value was

compared to the one obtained from the measurement of the static contact angle of water (Θ) on graphene surfaces with samples prepared according to the same procedure but on a planar substrate. The resulting static water contact angles (WCA) were 71 $\pm$ 1° for SLG and 70 $\pm$ 1° for FLG. From the measured values of Θ and the interfacial energy of graphene in water, $\gamma_{Graphene-Water}$, a second, indirectly determined measure of the graphene surface energy can be obtained using the Young-Dupré equation:

$$\gamma_{Graphene-Air} = \gamma_{Graphene-Water} + \gamma_{Water}\cos(\Theta_{Graphene-Water}) \tag{5.2}$$

Using $\gamma_{Water} = 73$ mJ/m^2, gives $\gamma_{Graphene-Air} = 106 \pm 7$ mJ/m^2, comparable but slightly lower than the values γ_{FLG} and γ_{SLG} obtained from adhesion force measurements (Figure 5.2). This result highlights the importance of directly measuring graphene surface energy as in our graphene-SFB method.

The absorption of airborne contaminants on pristine surfaces is a well-known phenomenon that has recently been under rigorous investigation with respect to its effect on the WCA on graphite. A recent examination of the published body of literature by Kozbial *et al.* indicates that the static WCA on pristine graphitic surfaces is $\Theta \simeq 65°$. Upon exposure to laboratory air, this value increases to $\Theta \simeq 90°$. This further demonstrates the cleanliness of the surface preparation [175].

When immersed in aqueous sodium cholate solution (NaCh), the interfacial energy of graphene was significantly lowered with respect to the graphene surface energy to $\gamma_{NaCh} = 29 \pm 6$ mJ/m^2. Indeed, sodium cholate is a surfactant that is known to stabilize graphene in solution by the absorption of a monolayer onto the graphene surface [176].

A similar reduction in measured surface energy was found when the graphene transfer was performed with PDMS-stamps that were not properly treated prior to the transfer procedure (see section 3.1). In this case the measured surface energy was drastically

lowered to 29 ±10 mJ/m^2, most likely due to the presence of PMDS-oligomers on the graphene surface.

It was found that the majority of the pull-off measurements on the graphene surfaces, both in nitrogen or liquid, were not reversible and yielded decreasing values of the surface or interfacial energy on subsequent measurements at the same location on the SFB lenses. In contrast, the pull-off was reversible (over more than five measurements) for the bare (epoxy-coated) SFB lenses. This points to a tendency of the graphene or underlying epoxy to delaminate or break during pull off. The surface instability may be linked to the relative weak bonds created in the plane of the graphene sheet at the boundaries between crystalline domains of CVD-graphene [177], which can be easily broken during pull-off, leading to tearing, delamination, or exfoliation.

Two-dimensional solids exhibit a unique behavior in which the surface energy of graphene is sufficient to promote self-tearing, sliding, and folding of the graphene sheets in particular in the presence of lateral forces [178]. It is thus possible that the lowered adhesion upon subsequent pull-offs originates from tearing, sliding, or folding due to lateral distortions and vibrations and the presence of defects within the contact area.

According to JKR-theory the relationship between contact diameter d and the applied load F is:

$$\left(\frac{d}{2}\right)^3 = \left(\frac{R}{K}\right)\left(F + 6\pi R\gamma + \sqrt{12\pi R\gamma F + (6\pi R\gamma)^2}\right) \tag{5.3}$$

where R is the radius of curvature of the surfaces, γ the surface energy and K is the effective modulus, given by:

$$K = \frac{4}{3}\left(\frac{1-v_1^2}{E_1} + \frac{1-v_2^2}{E_2}\right)^{-1} \tag{5.4}$$

where v_i is poisson's ratio and E_i is the elastic modulus. For two epoxy-supported graphene surfaces in contact under zero applied load ($F = 0$), using $E_{EPON} = 3.4$ GPa,

$v_{EPON} = 0.495$ [172], $R = 0.01$ m and $\gamma = 0.118$ mJ/m^2, the contact diameter $d_{F=0} =$ 106 μm. The grain sizes of the FLG and SLG were $\sim$ 5 - 10 μm and $\sim$ 50 - 100 μm (see sections 2.3.1 and 2.3.2), which is comparable but smaller in size to the contact diameter in predicted from JKR-theory. However, using mmSLG did not lead to an increase in reversibility of the pull-off experiments. Therefore the existence of weaker in-plane bonds at grain boundaries may not be the cause of the reduction in the measured adhesion force.

During the preparation of SLG/mmSLG-covered gSFB lenses, it was found that the underlying epoxy may be damaged during removal of the mica template (see section 3.3). It is thus possible that the reduced surface energy values, found on subsequent pull-offs results from local rupture of the epoxy during pull-off. The presence of small, local rips and debris is expected to cause a decrease in measured surface energy by increasing the roughness of the surface and lowering the contact area.

When polystyrene rather than EPON1004F was used as graphene-supporting epoxy layer, constant values for the adhesion force between the surfaces were found. However the values were much lower at $\gamma_{Graphene-on-Polystyrene} \sim 85$ mJ/m^2. The lowered value is expected due to the much higher roughness of the surface (section 3.3). The increase in roughness is thought to originate from PS's much longer chains, which interdigitate and cause the material to store mechanical stress [130, 100]. Polymer chain length also governs the mechanical properties of polymer films, changing the fracture behavior from brittle to ductile as the chains become longer and start to interdigitate [99]. It is thus possible that a balance between chain length and resulting surface properties of the gSFB lens exist. However, this was not investigated.

The surface energy values measured for graphene, lie close to those for the interfacial energy between graphite and graphene measured by Li *et al.* (154 ± 21 mJ/m^2) and Wang *et al.* (110 ± 5 mJ/m^2) [163, 164]. For graphite, which has been more intensively studied, Koren *et al.* and Wang *et al* measured the surface energy of graphite mesas through

manipulation of the mesa, finding $\gamma = 113 \pm 3$ mJ/m^2 and $\gamma = 185 \pm 10$ mJ/m^2 [161, 162]. Earlier experiments have yielded values within the range of these two experiments through, for example, heat of wetting data (130 mJ/m^2), examination of nanotube collapse (107 $\pm$ 38 mJ/m^2), and desorption measurements (186 $\pm$ 15 mJ/m^2) [179, 180, 181].

The measurements presented use CVD-graphene and are therefore relevant to use of graphene in high-end electronics. CVD-graphene requires the use of a transfer step to transfer the graphene from the growth substrate onto the target substrate, during which the surface is exposed to etchant, ultrapure water, and particle-free laboratory air. As such, the absorption of airborne contaminants or even the presence of an adsorbed layer of water [182] may affect the measured surface energy in a manner similar to that in ultraclean electronics fabrication facilities. Further, incommensurability of the two graphenes that are brought into contact would be expected to lower the effectively measured surface energy. The effect of incommensurability on the surface energy of graphite has been estimated to be in the range of 10 mJ/m^2 by Wang *et al.* [162]. For FLG and SLG, the contact area is larger or equal in size to the average grain size. As such, the measured adhesion can be considered an average over different twist angles existing between incommensurate graphene sheets. Finally, the roughness of our samples may contribute to measuring a lower value of the effective surface energy by reducing the effective area of contact. As a comparison, the RMS roughness measured ($\sim$ 1 nm) is large compared to that of a HOPG terrace, which is atomically smooth, but of similar magnitude to the stepped surface of cleaved HOPG (RMS 0.7 nm, $\sim$ 2 nm) [183, 184].

In conclusion, the experiments shown here represent the first direct measurement of the surface energy of CVD graphene using both single and few layer graphene at 115 $\pm$ 4 mJ/m^2 and 119 $\pm$ 3 mJ/m^2, respectively. The results show that the graphene surface is clean, and may be suitable for experiments with liquids. However, it was found that the surface is not always stable and that a contact-free calibration would need to be performed.

5.2 Outlook for gSFB measurements

In this thesis a method for the fabrication of graphene electrodes and their use inside a SFB has been reported and demonstrated with measurements of the surface energy of graphene. The aim of the gSFB is to enable surface force measurements in electrolytes with control of the surface electrical potential. A new method for the fabrication of smooth graphene surfaces was developed, however it was found that the surfaces cannot be reliably brought into contact to calibrate the optics. To resolve this, a contact-free calibration method was developed.

Owing to the present interest in graphene and its interactions with other media, there exist potential for applying this technique for direct determination of a range of useful properties and parameters. For example, the determination of interfacial energies may be used to investigate intercalation compounds used for the production of graphene via solvo-chemical exfoliation of graphite. Furthermore, scope exists for developing the procedure to study other 2-dimensional materials and doped graphenes in order to interrogate the differences in surface properties and interactions.

The limitation of this method is that only a single measurement spot can be calibrated and used when the gSFB is used to perform force measurements across electrolytes. For the conventional mica SFB the experimental preparation may take a few hours depending on the user. In contrast, for gSFB experiments, the surface preparation takes severals days. Further, using the mica SFB, multiple locations on the mica surfaces are accessible for experimentation. This allows the measurement spot to be changed, which is advantageous since in practice not all measurement spots are clean, and data may be collected on multiple locations. For gSFB experiments, only one location on the graphene surface is available due to the requirement for a contact-free calibration. As a result, only a relatively small amount of data can be collected per experiment. Thus, while careful repetition of measurements may result in the elucidation of interesting phenomena at

the electrolyte/graphene interface, the difficulty and effort required to obtain a working experiment using the gSFB is an important concern.

The gSFB as presented in this thesis may provide useful experimental data, however the continued application of the technique may be impractical. However, the knowledge gained with respect to the preparation of uniform glue layers and analysis of interferometric data can be used to revisit an old concept: that of the 3-mirror interferometer as proposed by Levins and Vanderlick [20], in which gold is used as polarizable surface. This 3-mirror setup is much simpler with respect to the lens preparation and will be discussed in the next chapter.

Chapter 6

The improved 3-mirror Au setup: new fabrication methods and optics for an old problem

This work was performed in collaboration with Dr. Marco Balabajew, a post-doc in our group, and is being prepared for publication.

6.1 Introduction

The desire for an SFB with control over the electrical potential on both surfaces has prompted the development of various setups, each with advantages and disadvantages. The most successful implementation, a setup introduced by the Kurihara group [21], measures forces on thick, template stripped metal surfaces via interferometry *ex situ*. Using this setup, force information can be obtained directly as with the conventional SFB. However, the optical information concerning the surfaces or the medium is lost.

Ruths and Heuberger introduced a 4-mirror setup in which forces between alkanethiol-

covered gold surfaces were measured. This setup requires elaborate surface preparation and optical analysis. Limiting factors are the low light intensity and the roughness of the gold surfaces, which is prepared by direct physical vapor deposition (PVD) of gold onto a thin layer of chromium, which serves as adhesion layer [139]. The 3-mirror setup proposed by Levins and Vanderlick suffers from the same problem with respect to surface roughness: although one of the surfaces may be template stripped, the other consists of a layer that is fabricated by direct PVD [20].

Template stripping involves physical vapor deposition (PVD) of a metal on a smooth template. Due to the poor adhesion between the template and the metal, the metal can be glued to another substrate and then peeled off from the template. This reveals a smooth metal surface, which can be an order of magnitude smoother than if deposited directly [13, 125]. With respect to use in SFB setups, this technique thus enables the measurement of surface forces with small length scales, such as the electrostatic screening length in electrolytes [187].

The optical elements in the 3-mirror setup are as follows: [*quartz*|mirror|spacer|conducting mirror|medium|conducting mirror|*glue*] (see section 4.1.1). In the work of Levins and Vanderlick, the spacer layer corresponds to a piece of mica that is coated with metal on two sides, using direct PVD rather than template stripping. In order to fabricate the metal surface via template stripping rather than direct PVD, the metal would have to be glued down. The fabrication of epoxy layers of uniform thickness using methods presented earlier in this thesis allows for the use of the 3-mirror interferometer *in combination* with template stripping, which enables the measurement of surface forces with small length scales using the 3-mirror setup.

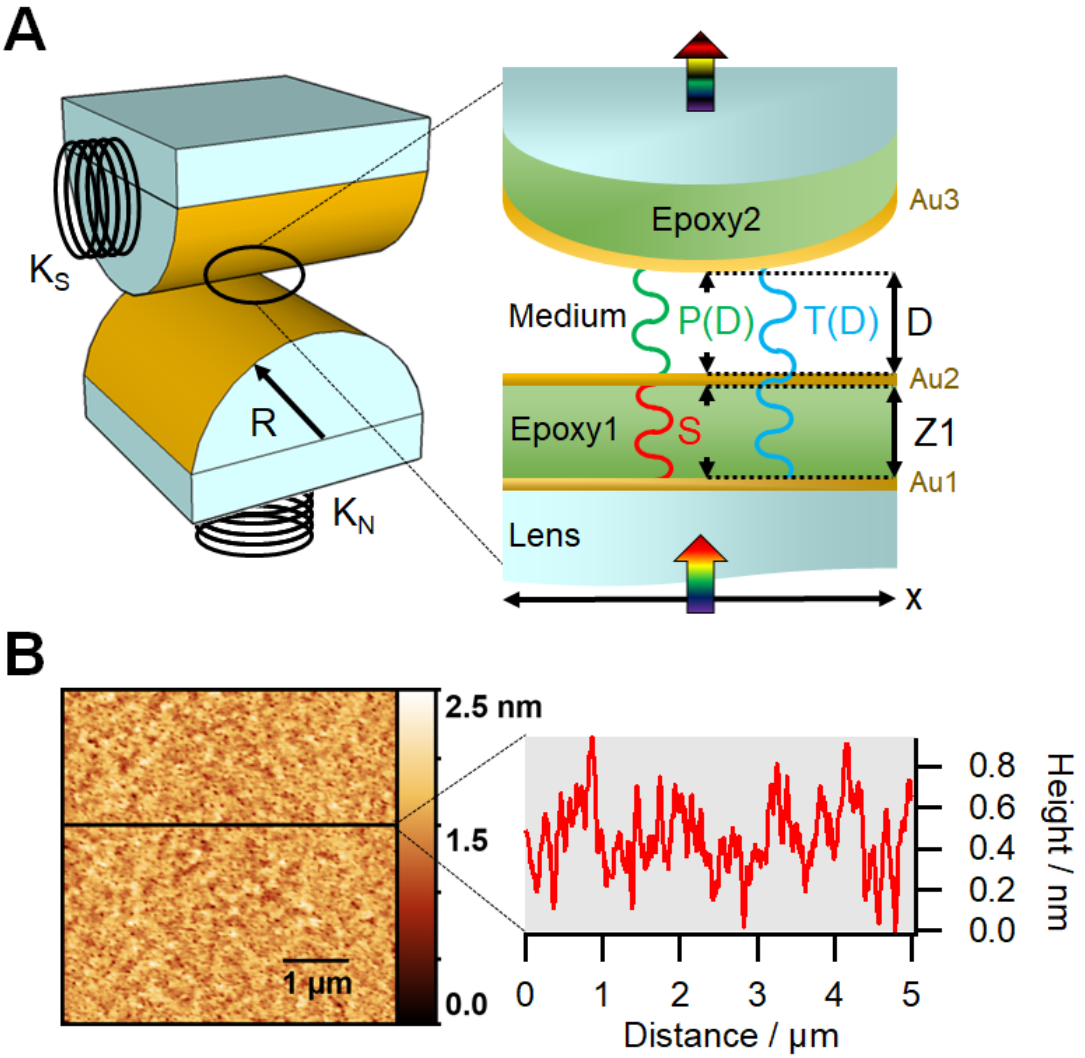


Figure 6.1: *(A) Schematic showing the 3-mirror SFB setup using gold as the mirror material. The gold coated lenses are placed in crossed-cylinder configuration, geometrically equal to a sphere on a flat surface. Normal and lateral forces can be measured by monitoring the displacement of the surfaces with respect to a known applied motion versus the deflection of a spring with known spring constant (K_S and K_N). Light enters the setup, constructively interferes between the different mirrors and emerges as interference pattern. Primary fringes (P(D), shown in green) depend on the distance between the mirrors (D) and originate from reflections between mirrors Au2 and Au3, across the medium. Secondary fringes (S, shown in red) are distance independent and arise from reflections between mirrors Au1 and Au2, across the epoxy spacer with thickness Z. Distance dependent tertiary fringes (T(D), shown in blue) arise from reflections between mirrors Au1 and Au3. (B) CM-AFM height map of a template stripped gold surface. The measured RMS roughness is 0.23 nm. The height profile shown on the right corresponds to the line drawn across the image.*

Figure 6.1-A shows a schematic of a 3-mirror SFB setup using gold as material for the mirrors. Both surfaces are coated with template stripped gold (Au2, Au3) and supported by a layer of epoxy. In order to be able to measure distances when the separation between the surfaces **D** is smaller than the diffraction limit of light, an additional gold layer (Au1) is present underneath one of the template stripped surfaces, separated by epoxy with of thickness **Z1**. Light enters from the bottom and emerges from the other end if it interferes constructively due to the reflections between the mirrors. Three different reflections are identified and are expected to give rise to different FECO patterns in the interferogram. Distant dependent primary fringes (P(D)), marked in green, result from reflections between the mirrors on the surfaces in contact with the medium, Au2 and Au3. A stationary set of secondary fringes (S, shown in red) results from reflections between Au1 and Au2. Finally a third set of distance dependent tertiary fringes arise (T(D), shown in blue) from reflections between the gold coating on the lens and on the other surface, between Au1 and Au3[1].

Figure 6.1-B shows a CM-AFM height map of a template strip gold surface, taken over a 5 x 5 μm^2 area. The measured RMS roughness is 0.23 nm, much smoother than measured for gSFB surfaces (see section 3.3) or surfaces prepared by direct PVD [13, 125].

The rest of this chapter will extensively discuss the optics and practical considerations required for the successful use of the 3-mirror setup, which provides a promising and accessible technique for studying surface forces across electrolytes with direct control of the electrical potential of the confining surfaces. Note that the data presented describes requirements for the successful execution of the setup. Measurements in liquids will be the subject of future work in the Surfaces Forces Laboratory.

[1]Note that the way light interacts through the interferometer is not trivial and the designation of primary, secondary and tertiary fringes to certain sets of reflections though useful, is only approximate

6.2 The tertiary fringes

A comparison between the interferometric data obtained using the conventional mica SFB and the 3-mirror setup, is shown in Figure 6.2. Figure 6.2-A shows a simulated interferogram (calculated using the multilayer matrix method, see section 4.1.1) for the mica setup at large distance (left panel), at $\mathbf{D} = 100$ nm (middle panel) and in contact (right panel). The thicknesses of the mica spacers used for the calculation was 5 μm. The calculation was adjusted to show partially vertical FECO fringes, visible in experiment due to flattening of the surfaces at the contact point (similar in geometry to a truncated sphere on a flat surface): in contact the surfaces flatten due to the deformability of the much softer underlying epoxy. This was also taken into account for the calculations of the 3-mirror setup, shown in Figure 6.2-C and a 2-mirror setup in which the mirror Au1 behind the layer Epoxy1 has been left out (Figure 6.1-B). For the 3-mirror setup, an epoxy thickness of 5.1 μm was used to ensure the secondary fringes were positioned centrally in the spectral range.

Using the non-conductive mica setup, the distance between the surfaces can be determined by analyzing the primary fringes, which are visible at all distances. In the 2-mirror setup, no fringes can be observed in the central contact area (that is, around x = 0 μm) at small separations. This highlights the importance of including the epoxy spacer in the interferometer by addition of another mirror. In the 3-mirror setup, fringes are still observed at close distance (100 nm) and in contact. Further, although three sets of fringes are expected (primary, secondary, tertiary, denoted by P(D), S and T(D) in Figure 6.1-A) only two sets of fringes can be distinguished.

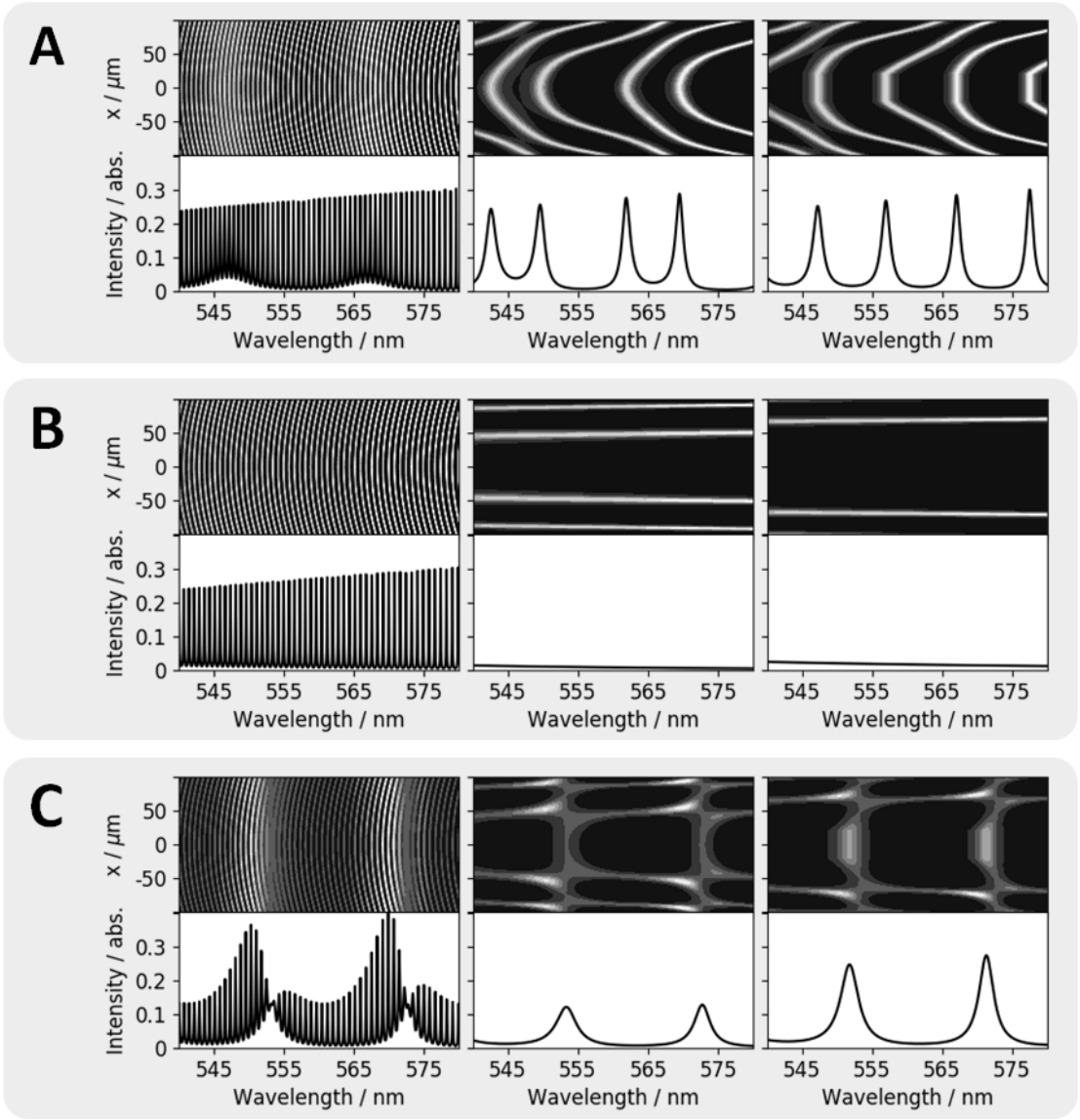


Figure 6.2: *Calculated interferograms of: (A) the conventional mica setup; (B) a 2-mirror gold setup in which the mirror labeled "Au1" in Figure 6.1-A has been omitted; (C) the 3-mirror gold setup. The upper panels show the expected interferogram across the x-axis in Figure 6.1-A. The lower panel shows the spectrum corresponding to* $x = 0$ *μm.*

To elucidate the origin of the fringe patterns shown in Figure 6.2-C, it is informative to consider a simple approximation, in which light intensity I^* of each fringe pattern is the product of light that passes through the interferometer through different transmissions and reflections. The transmission coefficient is $T^*_{i,j}$ and the reflection coefficient is $R^*_{i,j}$, where i, j refers to the materials at the reflecting interface. Approximating the mirrors to be equivalent in thickness and using the geometry [*Lens*|Au|Epoxy|Au|Medium|Au|*Epoxy*], it follows that for the different fringe orders:

$$I^*_{P(D)} \sim T_{Au,Lens}\, T^3_{Au,Epoxy}\, T^2_{Au,Medium}\, R^2_{Au,Medium} \tag{6.1}$$

$$I^*_{S} \sim T_{Au,Lens}\, T^3_{Au,Epoxy}\, T^2_{Au,Medium}\, R^2_{Au,Epoxy} \tag{6.2}$$

$$I^*_{T(D)} \sim T_{Au,Lens}\, T^5_{Au,Epoxy}\, T^4_{Au,Medium}\, R_{Au,Medium}\, R_{Au,Epoxy} \tag{6.3}$$

Equations 6.1-6.3 illustrate that compared to the primary and secondary fringes ($I^*_{P(D)}$ and I^*_S), the light intensity of the tertiary fringes ($I^*_{T(D)}$) results from two additional transmissions through the Au|Epoxy and Au|Medium interfaces ($T_{Au,Epoxy}$ and $T_{Au,Medium}$). The tertiary fringes ($I^*_{T(D)}$) are thus expected to be much lower in intensity than the primary and secondary ones.

To further illustrate the importance of the thickness of the gold layer involved in these additional transmissions (Au2 in Figure 6.1), calculations were performed using the multilayer matrix method (section 4.1.1) in which the thickness of this layer was varied and the obtained interference patterns were studied as a function of the surface separation. Figure 6.3-A shows the expected intensity plot for interference spectra as a function of distance and wavelength when Au1 = Au2 = 40 nm and Au3 = 0 nm. This configuration shows the characteristic distance independent secondary fringes, which appear as vertical bands in the plot and are highlighted by the dashed red line. Another extreme configuration is shown in Figure 6.3-D, in which Au1 = Au3 = 40 nm and Au2 =

0 nm. Here, only the distance dependent primary fringes are shown and highlighted by the green dotted line. The effect of the tertiary reflections becomes apparent when examining Figures 6.3-B,C, for which Au1 = Au3 = 40 nm and Au2 = 10 nm (in B) and Au2 = 40 nm (in C). These intensity plots verify the simple result from equations 6.1-6.3: the presence and influence of the tertiary fringes on the interference spectra becomes more pronounced as the transmission through the Au|Epoxy and Au|Medium interfaces becomes higher. Indeed, for Au2 = 40 nm (Figure 6.3-C) the blueshift caused by the tertiary fringes is almost negligible, whereas for Au2 = 10 nm (Figure 6.3-B), the blueshift caused by the tertiary fringes is so pronounced the intensity plot begins to resemble that of the classic two-mirror SFB. Thus, although the intensity of the tertiary fringes is expected to be small, calculations indicate that they can be used to determine the distance between the surfaces.

Figure 6.4-A shows a calculated spectrogram showing the intensity of the transmitted light as a function of wavelength and distance between the surfaces using the configuration [*Lens*|Au1|Epoxy1|Au2|Air|Au3|*Epoxy2*], using the experimentally feasible configuration: Au1 = 35 nm, Au2 = 20 nm and Au3 = 25 nm. In Figure 6.4-B the spectra corresponding to the lines drawn in Figure 6.4-A are shown. Figures 6.4-C,D show the progression of the spectral features with 5 nm steps from D = 200 nm. The images show how as the distance is decreased, the primary fringes move from longer to shorter wavelength and strongly attenuate the secondary fringes. When the primary fringes are not or barely visible in the wavelength range of interest, the attenuation caused by the tertiary fringes shifts the fringes towards the blue end of the spectrum (as would be the case for the conventional mica SFB or gSFB). This complicates the analysis of the interferometric data compared to the conventional mica setup, as simply tracking the peak positions of the primary fringes is not possible. This indicates that, unless a force profile between only 150 nm and contact is measured, the full spectral profile will need to be analyzed.

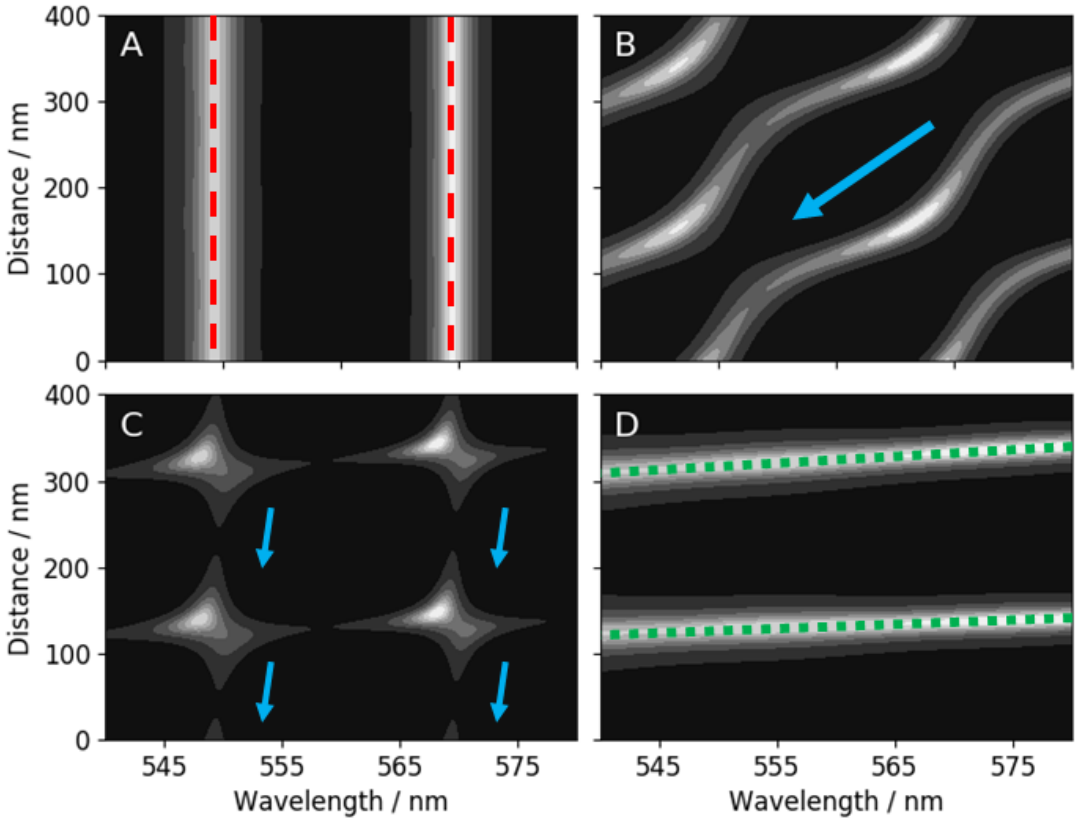


Figure 6.3: *Contour plots showing the transmitted light intensity as function of wavelength and distance for different configurations. (A) Au1 = 40 nm, Au2 = 40 nm, Au3 = 0 nm. This mirror configuration only gives rise to secondary fringes, highlighted by the red dashed lines. (B) Au1 = 40 nm, Au2 = 10 nm, Au3 = 40 nm. The intensity of the tertiary fringes dictates its effect on the observed interference pattern. Here the Au2 is thin and the effect is so strong that the fringes seem to continuously blueshift with decreasing distance (blue arrow). (C) Au1 = 40 nm, Au2 = 40 nm, Au3 = 40 nm. The tertiary fringes appear to attenuate the secondaries resulting in an apparent blueshift of the secondary fringes with decreasing distance (blue arrows). (D) Au1 = 40 nm, Au2 = 0 nm, Au3 = 40 nm. This mirror configuration only gives rise to primary fringes, highlighted by the green dashed lines.*

To further emphasize the importance of full spectrum fitting, the sum of squared residuals (SSR) between spectra corresponding to D = 0 - 500 nm is shown against two distance values for **D** (Distance1, Distance2) in a contour plot in Figure 6.5. Plots for both air and a medium with refractive index $n_{medium} = 1.4244$ (similar to the refractive index of the ionic liquid $[C_2C_1Im][NTf_2]$ used in Chapters 4 and 5) are shown. Dark regions in the plot correspond to two values for Distance1 and Distance2 for which the difference in spectral features is small. These occur periodically as local minima and along the diagonal

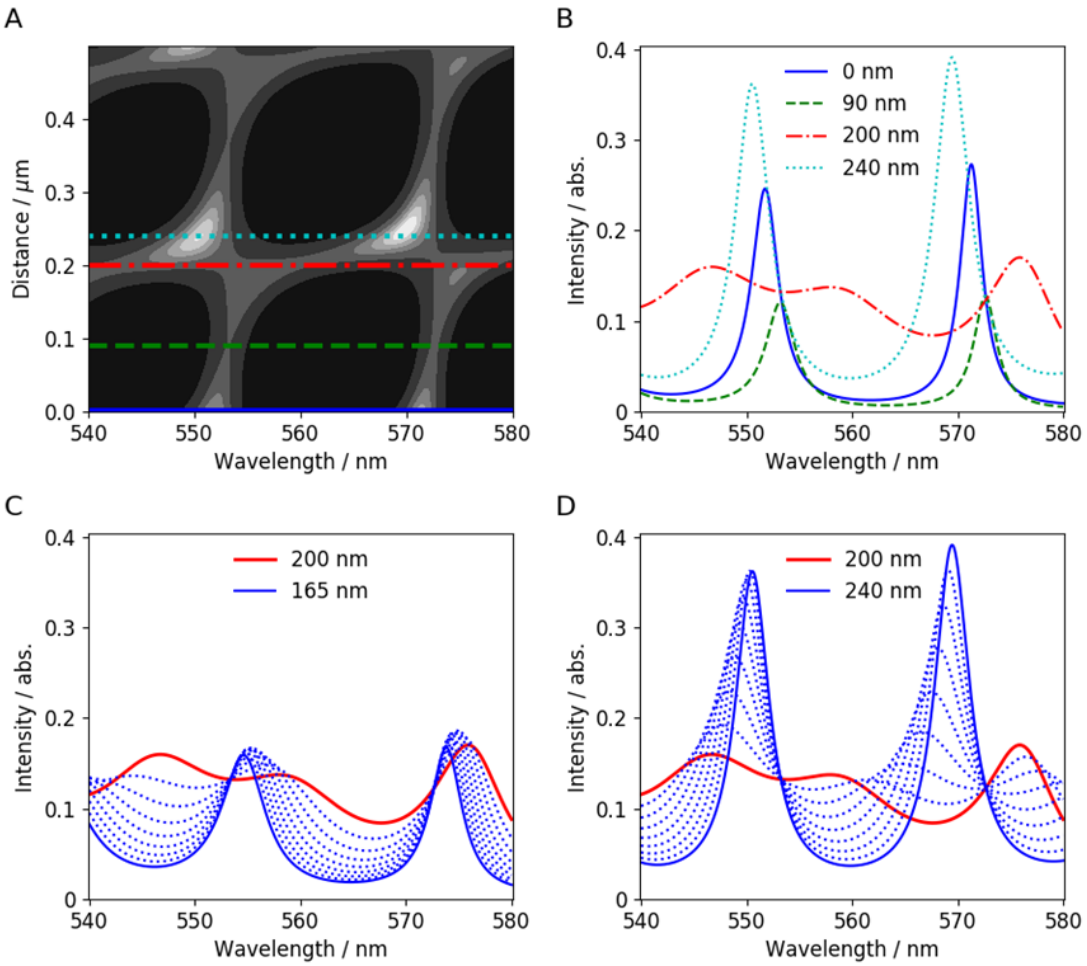


Figure 6.4: *Changes in interference spectra as a function of distance: (A) Contour plot showing the transmitted light as function of wavelength and distance. The lines correspond to the spectra shown in B. (B) Interference spectra corresponding to the lines shown in A. (C,D) Evolution of interference spectra with 5 nm steps from 200 nm to 165 nm and 240 nm respectively.*

as the global minimum Distance1 = Distance2 (for which the SSR = 0). Figures 6.5-B,D show the interference spectra of the combination of distances corresponding to the red and blue dashed lines in A and C respectively. At these values the SSR value has a local minimum. At the peaks of the spectra shown in Figures 6.5-B,D, the spectra are almost identical. However, the spectra deviate in the wavelength range 540-545 nm, showing that

a full spectrum fit will help distinguish between these distances. The spectral similarities occur periodically, according to (similar to equation 4.26):

$$d_{fringe\,orders}(\lambda) = \frac{\lambda}{2n_{medium}} \tag{6.4}$$

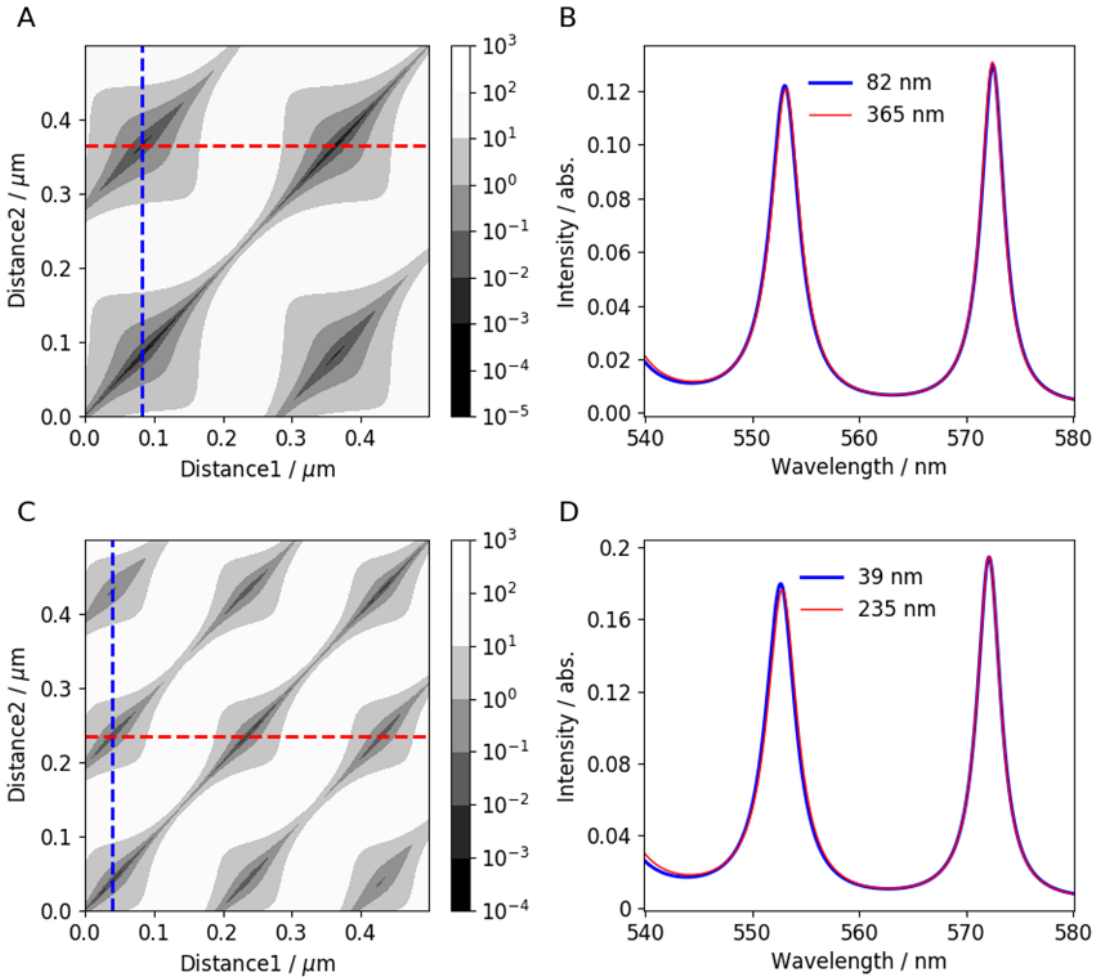


Figure 6.5: *Full spectrum fitting allows better differentiation between interference spectra recorded at different distances using the 3-mirror setup. (A) Contour plot showing the SSR between spectra at different distances (x,y axes) in air. The diagonal corresponds to the global minimum for which Distance1 = Distance2 and the SSR = 0. Local minima are present at* $\boldsymbol{D}$ *= 82 nm and* $\boldsymbol{D}$ *= 365 nm and are indicated with blue and red dashed lines respectively. (B) Interference spectra corresponding to the distances highlighted with the blue and red dashed lines in A. (C) Contour plot showing the SSR between spectra at different distances (x,y axes) in liquid. The diagonal corresponds to the global minimum for which Distance1 = Distance2 and the SSR = 0. Multiple local minima are present in the distance range examined. The minima at* $\boldsymbol{D}$ *= 39 nm and* $\boldsymbol{D}$ *= 235 nm are highlighted with blue and red dashed lines respectively. (D) Interference spectra corresponding to the distances highlighted with the blue and red dashed lines in C.*

Measurements of surface forces across electrolytes are often performed to elucidate mechanisms with length scales < 100 nm. Therefore the effect of system parameters such as the thickness of the gold mirrors or the epoxy spacer on resolution was investigated in the range of 100 nm to contact. Figure 6.6-A shows a contour plot showing the spectral intensity as function of wavelength and distance. Underneath interference spectra corresponding to contact ($\mathbf{D} = 0$ nm) upto $\mathbf{D} = 100$, nm with 10 nm steps are shown. The position and change in intensity of the leftmost peak is shown as a function of the thicknesses of the gold layers in Figures 6.6-C,D,E,F. The legend shows the thicknesses of the corresponding gold layers (Au1:Au2:Au3). A reduction in thickness of the gold layers results in an increase in peak shift across the distances examined. Further, the peak shift and changes in peak intensity are most profound when the center layer (Au2) is reduced with respect to the other layers as shown in Figure 6.3. Both effects arise due to the increase in tertiary fringe intensity with respect to the intensity of the primary and secondary fringes, as approximated in equations 6.1.

In the limiting case in which the thickness of the center gold layer would be reduced to a single atom in thickness, this would correspond to asymmetric mica-gold setup described in Chapter 1 [15, 16, 17]. However, to fabricate a continuous, conductive template stripped gold layer in real experiments, a minimal thickness is required. Conversely, the layers also cannot be too thick since this would lower the intensity of the collected light. When the light intensity is low, the CCD camera requires a much longer exposure time to collect an image, thus limiting the speed at which images can be recorded. A set of gold layers with thicknesses of (Au1:Au2:Au3) = (30 nm : 20 nm : 30 nm) can be easily fabricated. This, in combination with a CCD camera that has 2688 pixels across the wavelength range visible in the spectrometer ($\sim$ 40 nm), using the peak shift observed over 100 nm ($\sim$ 3.5 nm), gives a resolution of 2.4 pixels/nm for the setup calculated, close to that for conventional mica SFB.

The resolution with which the distance between the surfaces can be determined is strongly influenced by the thickness of the (epoxy) spacer (**Z1** in Figure 6.1-A), as is the case in any SFB-type experiment. This is shown in Figures 6.7-A,B which show the effect of the epoxy thickness on the shift in peak intensity and peak position from contact to **D** = 100 nm and indicates a smaller **Z1** provides a higher resolution. However, not all epoxy thicknesses are equally suitable for performing an experiment. Even though the spectra are fit to a fully calculated spectrum, rather than just the peak positions, the fit is more accurate when multiple spectral features (peaks), are present. It is advisable to find a balance between resolution with respect to peak position, and the spectral features available for fitting, for example by using an epoxy thickness corresponding to two secondary fringes within the range of collected wavelengths.

Figure 6.7-C shows a contour plot in which the spectral intensity is shown as a function of wavelength and the thickness of the epoxy spacer when the surfaces are in contact. The red horizontal line corresponds to a single interference spectrum for a given thickness, in this case **Z1** = 4.9 μm (inset in D). The number of peaks present at each of these epoxy thicknesses is shown in Figure 6.7-D. Around **Z1** $\simeq$ 5 μm, two secondary fringes are present in the experimental spectral range ($\sim$ 540 nm - 580 nm), providing a good combination between resolution and spectral features for fitting. By adjusting the concentration and spin speed during spin-casting, epoxy spacers with such thicknesses can be easily fabricated (see sections 3.2 and 4.3.3).

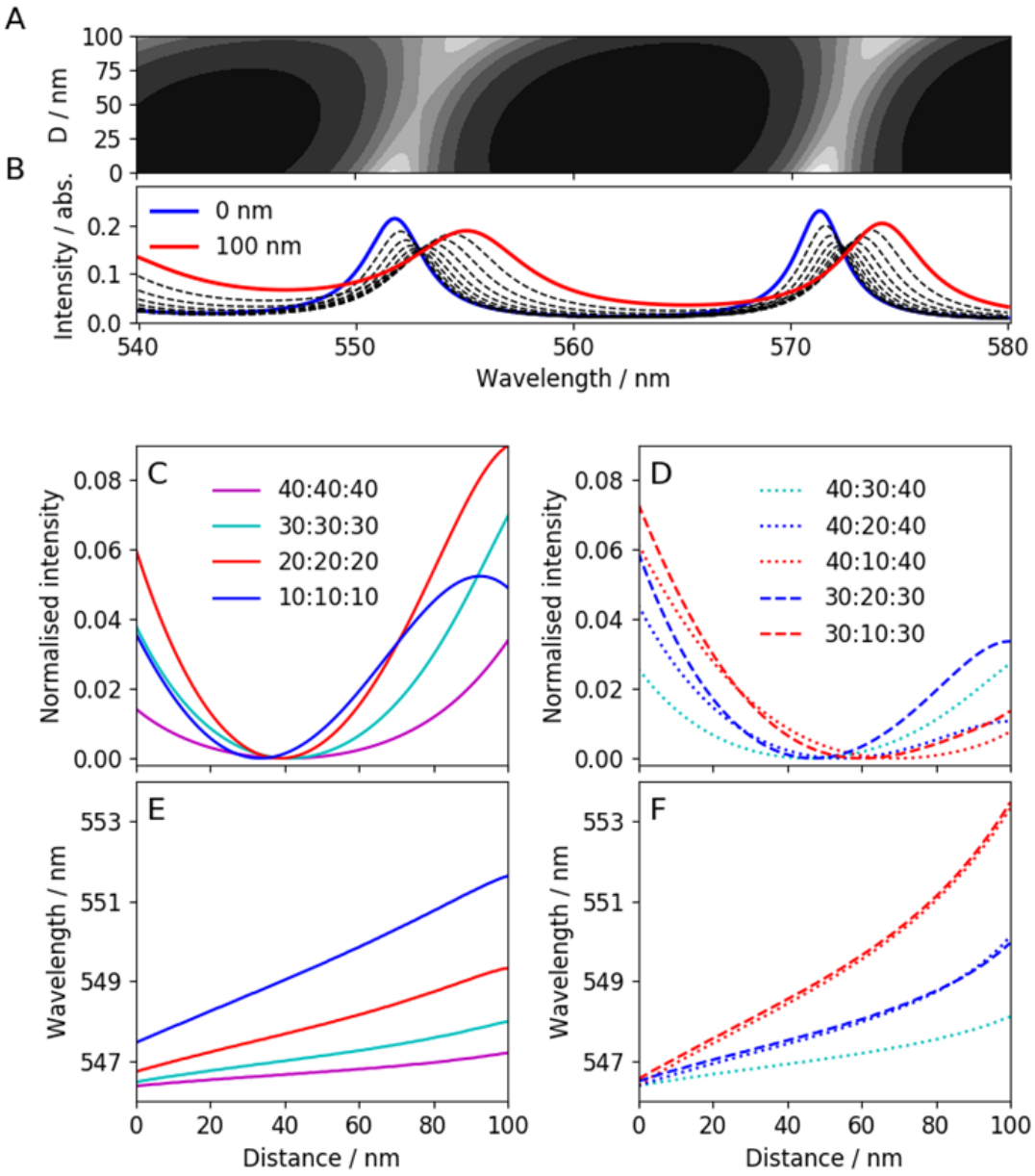


Figure 6.6: *Calculated effect of the thickness of the gold mirrors on spectral resolution. (A) Contour plot showing the spectral intensity as function of wavelength and distance using (Au1:Au2:Au3) = (30 nm : 20 nm : 30 nm) for the thicknesses of the gold layers. (B) Interference spectra corresponding to distances from contact to 100 nm with 10 nm steps, as shown in the plot in A. (C,D) Intensity of the left-most peak as a function of distance for different gold thicknesses. The intensities have been normalized to have their lowest value at zero to allow for facile comparison. The thicknesses are shown in the legends and correspond to (Au1:Au2:Au3). (E,F) Peak position of the left-most peak as a function of distance. The lines shown correspond to the legends shown in C and D.*

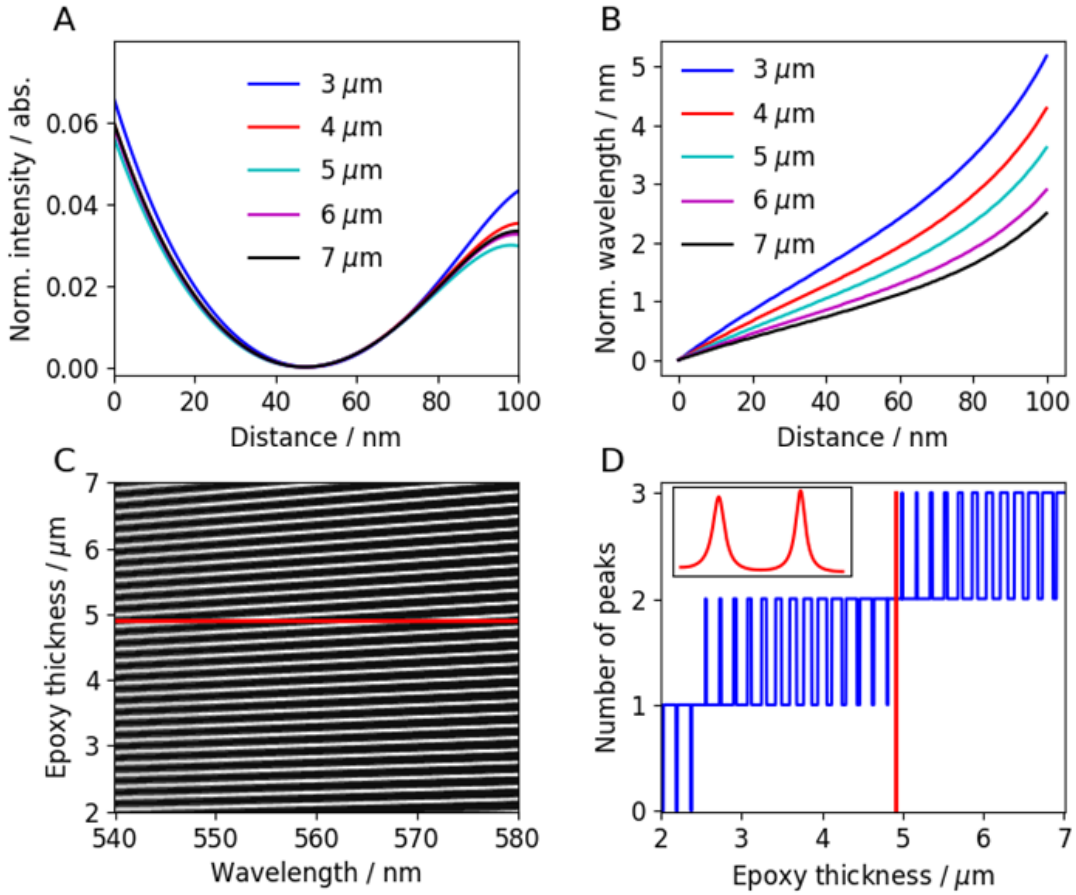


Figure 6.7: *Calculated effect of the thickness of the epoxy spacer (**Z1**) on spectral resolution. (A,B) Intensity and peak position of the left-most peak as a function of distance for different epoxy spacer thicknesses. The intensities and wavelength values have been normalized to have their lowest value at zero to allow for facile comparison. (C) Contour plot showing spectral intensity as a function of wavelength and epoxy thickness in contact. The red horizontal line corresponds to a single interference spectrum for a given thickness, in this case **Z1** = 4.9 μm (inset in D). (D) Number of peaks present in the spectral range 540 nm - 580 nm, as function of the thickness of the epoxy spacer. The red line indicates the epoxy spacer thickness corresponding to **Z1** = 4.9 μm. The inset shows the corresponding interference spectrum.*

6.3 Strengths and limitations

The 3-mirror setup allows for surface force experiments in which the electrical potential of both surfaces can be controlled. By tailoring system parameters, such as the thickness of the mirrors and the epoxy spacers, resolution close to that of the conventional mica SFB can be achieved.

One of the strengths of the setup is that it can be realized without any significant alterations to the SFB, for example as is the case in the setup used by Kurihara [21]. In the 3-mirror setup, the distance between the surfaces is determined using the tertiary FECO (Figure 6.1). However, due to the relatively low intensity of the tertiary fringes it is important to match the refractive index of the lenses, with that of the Epoxy2 layer, the epoxy layer that has so far been considered to be outside of the interferometer and is used to support the mirror Au3 (see Figure 6.1-A). When these materials are not index matched, the reflectance at the interface $R^*_{Epoxy2,\,Lens}$ is not negligible and attenuates the collected light intensity. To correctly interpret the obtained interferometric data the stack: [*Lens*|Au1|Epoxy1|Au2|Air|Au3|Epoxy2|*Lens*], rather than [*Lens*|Au1|Epoxy1|Au2|Air|Au3|*Epoxy2*] would need to be considered.

Figure 6.8-A shows the difference between two spectra that differ only in thickness of the Epoxy2 layer (**Z2**), using $n_{Lens} = 1.46$ and $n_{Epoxy2} = 1.55$. The thickness of the Epoxy1 layer used here is **Z1** = 4.5 μm. Due to the refractive index mismatch, changing the thickness of **Z2** causes a shift in both the absolute peak intensity and the intensity ratio. This change in intensity cannot be accounted for using a simple calibration, as it strongly depends on **Z1** and **Z2**. Figure 6.8-B shows the intensity ratio between the two peaks in the case that the surfaces are in contact (0 nm, teal line) or separated by 100 nm (purple line), as a function of the thickness of Epoxy2. It indicates that small changes in thickness have a strong, nonlinear influence on the intensity of the peaks. The peak ratios of the distances shown in Figure 6.8-A correspond to thicknesses of **Z2** only

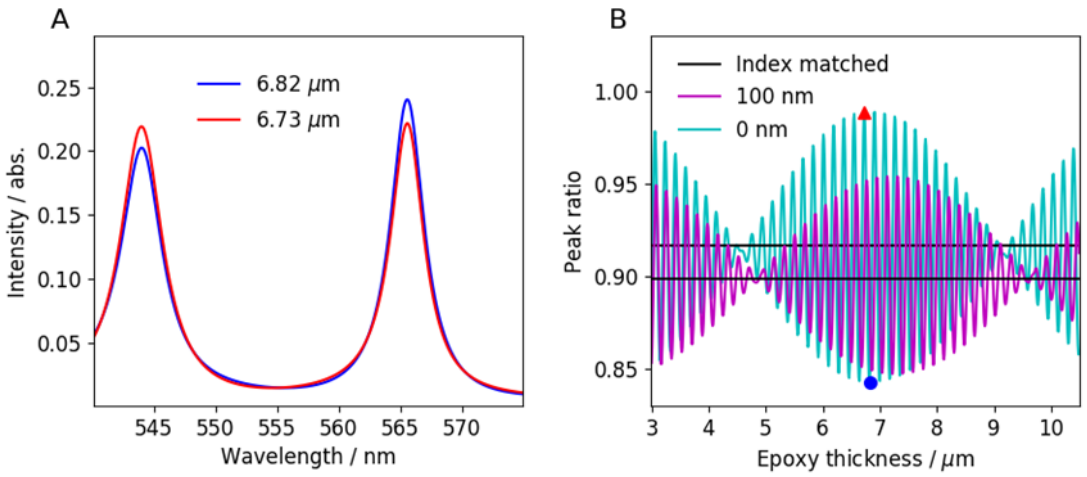


Figure 6.8: *Effect of mismatch between the refractive indexes of the epoxy layer supporting the mirror Au3 (Epoxy2) and the underlying lens (Figure 6.1-A). (A) Varying the thickness of the Epoxy2 layer causes both shifts in absolute intensity and the intensity ratio between the peaks. (B) Intensity ratio between the peaks and a function of the thickness of Epoxy2 in contact (teal line), at a surface separation of 100 nm (purple line), and when index matched (black lines). The peak ratios corresponding to the distances shown in Figure 6.8-A are indicated with the blue circle (**Z2** = 6.82 μm) and red triangle (**Z2** = 6.73 μm).*

90 nm apart, and are indicated with the blue circle (**Z2** = 6.82 μm) and red triangle (**Z2** = 6.73 μm). When the epoxy spacer and the underlying lens are index matched, i.e. $n_{Lens} = n_{Epoxy2}$, the ratio between peak intensities no longer depends on distance (black lines). Therefore, the correct interpretation of interferometric data obtained using this 3-mirror setup, requires lenses with the same refractive index as the epoxy spacer.

A potential limitation of the system lies in the ability to fabricate epoxy spacer layers of sufficient uniformity and stability with respect to the studied electrolyte. It has been shown in this thesis that fabrication of such layers is possible via spin-coating EPON1004-F from Ethyl Acetate onto mica (see sections 3.2 and 4.3.3). Alternatively, fabrication of uniform polymer layers prepared via vapor deposition techniques, with a T_g suitable for template stripping, may provide an alternative route to the fabrication of layers that are uniform across the entire lens surface [188].

To illustrate the importance of having a spacer layer of uniform thickness, Figure 6.9 shows a calculated interferogram for which the thickness of the spacer is uniform (6.9-A),

and one for which the thickness increases linearly with a slope of 1:1000 (6.9-C). The red line through the center of the image corresponds to the point of closest approach, which is used during the analysis to determine the distance between the surfaces. To reduce the noise in the data, the interference spectrum at this line is often averaged by including adjacent lines. The lateral (x in Figure 6.9-A,C) resolution of the CCD camera in the current SFB setup is 0.33 μm/pixel. Averaging is often performed across the 3 nearest pixel positions, corresponding to a range of 2 μm. Figures 6.9-B,D show the interference spectra corresponding to the outer most pixel positions, $\pm$ 1 μm from the central (red) line profile respectively. Whilst for a spacer of uniform thickness, the spectra overlap, there is a clear shift in peak position when the spacer thickness increases linearly. This highlights the importance of being able to fabricate uniform spacer layers (note: due to the use of crossed cylinders, areas of uniform thickness along the apex of the fabricated 3-mirror SFB lenses may be selected by moving the lenses laterally with respect to one another).

As highlighted at the start of this chapter, an advantage of the 3-mirror setup over, for example, Kurihara's setup [21], is that light is passed through the interferometer and changes that occur in the optical path can be monitored *in situ*. This is particularly pertinent when (noble) metal surfaces are brought into contact, since damage may occur due to "cold welding". Figure 6.10 shows the effect the formation of such a cold weld may have on the surfaces. Figure 6.10-A shows an interferogram in which the gold surfaces in a 3-mirror setup were brought into contact in air. Subsequently, the surfaces were slowly moved apart against the deflection of the normal spring. Due to the high adhesion caused by the weld, one of the gold layers was transferred to the other when the surfaces were separated (Figure 6.10-B). The latter was confirmed using the optical microscope, as shown in figure 6.10-C,D.

The observation of surface damage due to cold welding of smooth template stripped

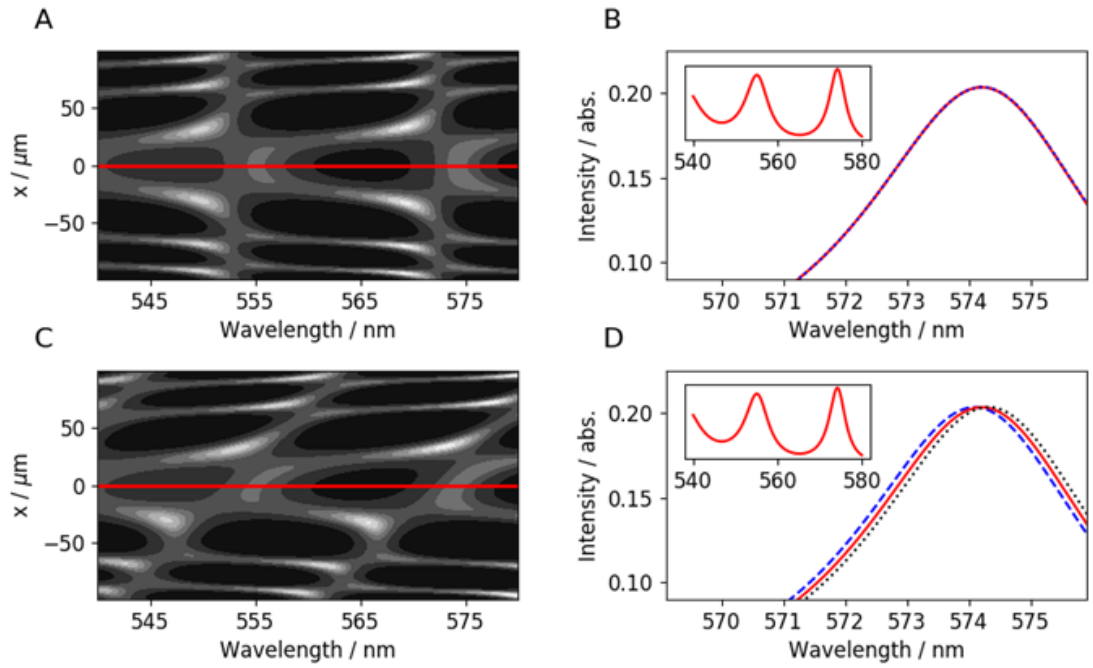


Figure 6.9: *Effect of the uniformity in thickness of the epoxy spacer on spectral processing. (A) Interferogram of the 3-mirror setup with an epoxy spacer of uniform thickness, of which the surfaces are separated 100 nm. (B) Interference spectra corresponding to the red line in A (red line at $x = 0$) and at $x = \pm 1$ μm (blue dashes and dotted lines). The spectra overlap. The inset shows the full spectrum corresponding to the red line. (C) Interferogram of the 3-mirror setup with an epoxy spacer of nonuniform thickness, of which the surfaces are separated 100 nm. The thickness of the spacer increases linearly across the x-range. (D) Interference spectra correspond to the red line in A (at $x = 0$, red line) and at $x = \pm 1$ μm (blue dashes and dotted lines). The peaks are blue/red shifted according to the decrease/increase in epoxy spacer thickness. The inset shows the full spectrum corresponding to the red line.*

Au surfaces, highlights both an advantage and limitation of the 3-mirror technique. In air or in liquids in which the surfaces readily come into contact, the surfaces may be damaged upon separation. However, in liquids in which stable interfacial liquid layers are formed and strong structural forces are present, or when the surfaces have been modified with self-assembled monolayers, this is not a concern. Regardless, the user will know if surface damage has occurred due to changes in the interference spectra.

One unique advantage of the 3-mirror setup is that under certain conditions the contact position of the fringes can be inferred from the behavior of the fringes. As the distance between the surfaces is slowly decreased, the surface separation eventually becomes so small that the primary fringes (P(D) in Figure 6.1) are only periodically visible. Concomitantly,

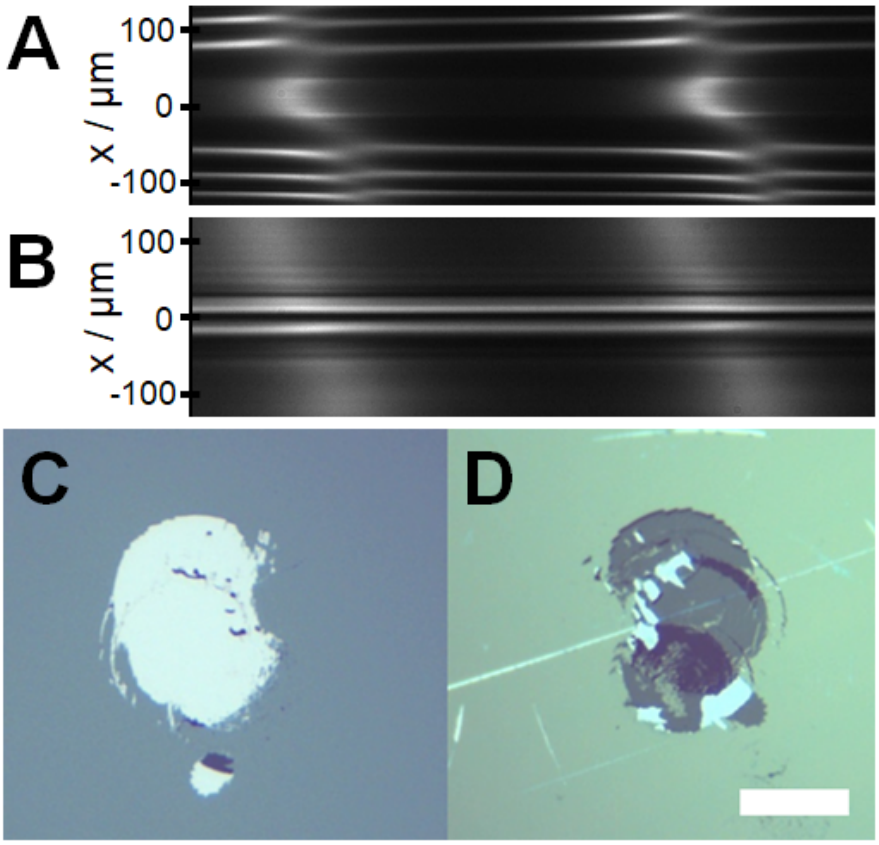


Figure 6.10: *Recorded interferogram of 3-mirror SFB setup using gold surfaces recorded in air: (A) in contact and (B) after separation of the surfaces. Upon separation the surfaces jumped a very large distance apart so that the primary fringes are no longer visible. Further, during separation one of the gold layers (Au2 in Figure 6.1) transferred onto the other (Au3). (C,D) Optical microscope images of the both surfaces. The scatches in D correspond to scratches on the lens surface and were present prior to the experiment. The scale bar is 100 µm.*

the primary fringes undergo significant broadening when the surfaces are close to contact. As a result, the delay between the attenuation (i.e. shift in peak intensity and position) of the two peaks decreases in a characteristic manner.

Figure 6.11 indicates how the broadening of the primary fringes affects the interference spectra. Figures 6.11-A,B show the difference in peak intensity and peak position between the two peaks as a function of distance. As the surfaces approach contact, the broadening of the primary fringes causes the intensity difference between the two peaks to decrease as the primaries move through. Further, the distances over which the peak positions differ, are reduced as well. Figures 6.11-D,E,F show the interference spectra corresponding to

the distances at which the lines are drawn in Figures 6.11-A,B. Equation 6.4 was used to the determine the distances at which to draw the lines of the same color in Figure 6.11, so that between the different fringe orders each set of lines corresponds to the same point in the spectrum. The images show that, due to the broadening of the primary fringes, as the primary fringes move through from Figure 6.11-F to Figure 6.11-D, the increase in spectral intensity at 3 fringes orders from contact is much more localized than the increase in spectral intensity at 1 fringe order from contact.

During an experiment, when the contact spot is changed only by a small amount so that the epoxy thickness on the new contact position is within 100 nm of the old one, the user has a very good estimate of the contact prior to performing a force profile. Further, when well-developed procedures are used for the fabrication of the epoxy spacer, such estimates may be used between experiments.

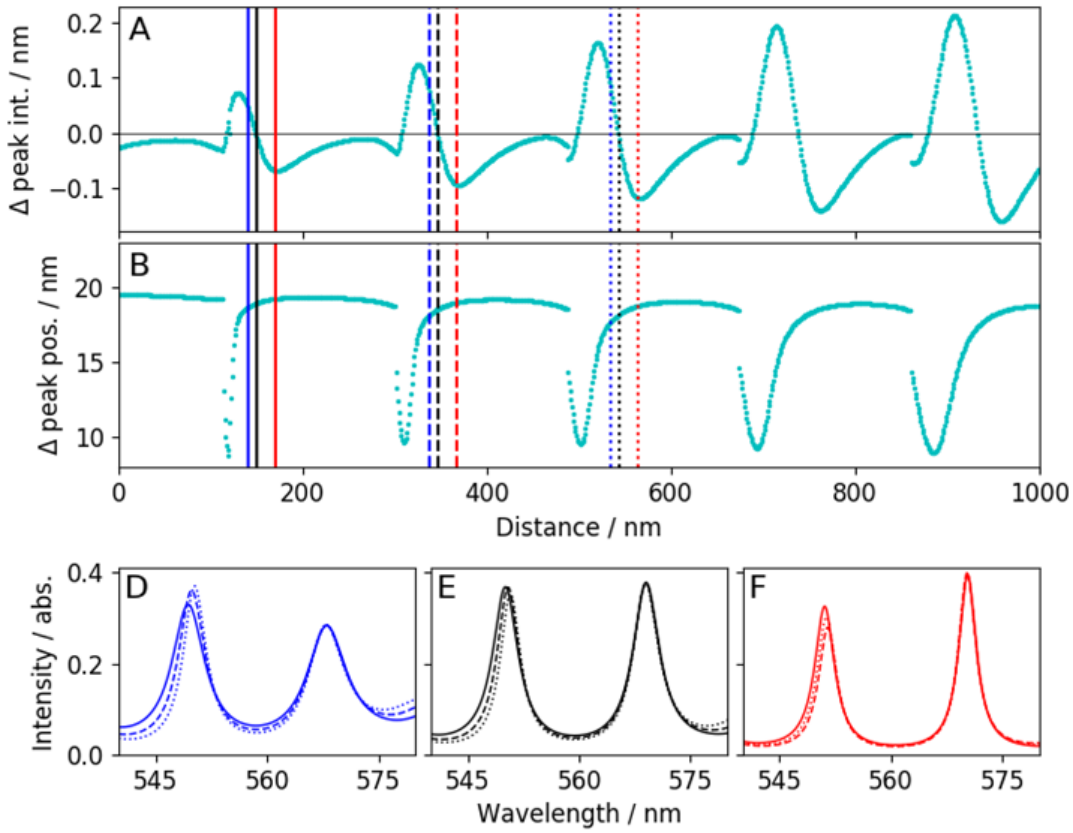


Figure 6.11: *The broadening of the primary fringes allows the contact position to be determined a priori for a given epoxy spacer thickness. (A) Difference in peak intensities between the two visible peaks as a function of distance. (B) Difference in peak position between the two visible peaks as a function of distance. (C,D,E) Spectral evolution of three fringe orders at different distances. Far from contact (dotted lines), the primary fringes are less broad, giving rise to a more localized change in intensity (moving from E to D). Close to contact (solid lines) the broadening of the primary fringes causes both peaks to increase almost simultaneously.*

6.4 Running an experiment

The experimental procedure using the 3-mirror setup differs from the procedure for the conventional mica SFB. For example, due to cold welding of the surfaces, a contact calibration is not possible. However, the bright secondary fringes can be used to determine the contact position without bringing the surfaces into contact.

To record the secondary fringes, the same procedure as outlined in chapter 4 is used: by moving the surfaces whilst recording an image at large distance, the primary (and tertiary) fringes are averaged out. To fit the recorded averaged secondaries, an image of the primary fringes is recorded as well. Since the apex of the primary fringes corresponds to the point of closest approach, the secondary fringes need to be fitted in this region. The apex of the primary fringes is obtained by fitting the primary fringes to a parabola.

The full spectrum of the secondary fringes is fitted using a brute force search. However, after an initial rough estimate is obtained, the fitting range is selected periodically according to equation 4.26. As discussed, it is favorable to have more than one secondary fringes in the spectral range as it improves accuracy.

In contrast to the method presented in chapter 4, no approximations or simplified geometries are used to fit the secondary fringes: a high level of accuracy is required and the inaccuracy due to the absorbance in the metal (gold) layers is too large.

Since the full spectrum needs to be fitted, it is important to account for the light intensity of the incoming light, and the data recorded by the CCD camera in absence of any light, as described by Levins and Vanderlick in their original paper [20].

Finally, a force profile may be analyzed starting at the closest distance during the approach. If a liquid with pronounced interfacial structuring is studied, as is the case for many ionic liquids [145], the surfaces may be brought into close contact without damaging the surface due to cold welding. In this case, the closest distance recorded during the force

profile is used as starting position for the analysis of distances, since it is likely within a few nanometers of the contact position found from fitting the secondary fringes.

6.5 Outlook

This chapter described how the 3-mirror SFB setup, as proposed by Levins and Vanderlick [20] may be used in combination with the fabrcation of uniform epoxy spacer layers as described in sections 3.2 and 4.3.3. The presented method provides a viable, easily adapted method for SFB-users to study surfaces forces across electrolytes with potential control between symmetrically polarizable surfaces. It is expected that the method will help provide valuable new insights into the behavior: of strongly confined concentrated electrolytes currently under investigation in the Perkin research group; controlling friction via surface potentials; and friction between surfaces modified with self-assembled monolayers.

Chapter 7

Summary & Outlook

The aim of this thesis work was to develop a lens modification for the Surface Force Balance (SFB) which would allow for surface force measurements across electrolytes confined between two polarizable surfaces. At the start of this thesis work, graphene had been proposed as suitable candidate for such a modification as the result of a collaboration between the Surface Forces Laboratory (group of Prof. Susan Perkin) and the Nanomaterials by Design group (prof. Nicole Grobert). The main body of the thesis thus describes the fabrication and use of a SFB in which measurements are performed at the graphene/electrolyte interface: the *graphene* Surface Force Balance (gSFB).

The production of graphene using Chemical Vapor Deposition (CVD) and its subsequent use to fabricate gSFB lenses, for which the surface is coated with graphene supported by an uniform layer of epoxy, is described in Chapters 2 and 3. In addition, it discusses the suitability of different CVD graphene production procedures for the fabrication of such lenses. It is found that a limitation of the fabrication technique is the surface roughness which can be obtained. Rougher graphene surfaces can be easily fabricated, whilst the production of gSFB lenses with very smooth graphene surfaces (RMS $\leq$ 0.5 nm) is associated with damage to the graphene-supporting epoxy. This damage is incurred during the removal of the mica template in the final template stripping step of the gSFB lens

fabrication. A likely cause is the high adhesion between graphene and mica. For rougher surfaces, in which the graphene is not completely in conformal contact with the mica template, removal of the mica is likely facilitated by the intercalation of water through small channels between the graphene and the mica. For smoother surfaces less of such channels exist, causing the underlying epoxy to rupture as the mica template is removed.

The surface smoothness of the graphene-coated gSFB lenses that can thus be obtained limits the breadth of experiments that can be performed using the gSFB, as forces with length scales comparable to the surface roughness profile can no longer be resolved. Whilst different transfer approaches and techniques were exhaustively investigated, the surface roughness may be reduced by introducing or changing certain features of the fabrication method. For example, the fabrication of a self-assembled monolayer on the mica template prior to placement of the graphene would reduce the adhesion between the graphene and the mica template and prevent rupture of the underlying epoxy. However, the implementation of such additional steps increases the chance of introducing both particulate and molecular contamination in an already lengthy preparation procedure in which each step may introduce contaminants.

The use of secondary Fringes of Equal Chromatic Order (FECO) to determine the deviation of the radius of curvature as measured using the primary FECO patterns was described in Chapter 4. It was found that adjusting for deviations in the radius of curvature is not necessary when the epoxy layers are fabricated using the protocols described in Chapter 3, since the epoxy layer is essentially uniform. However this method does verify the correct value for the radius of curvature is used and may be implemented in other SFB techniques using spacers of non-uniform thickness.

Chapter 4 also introduced a new method for determining the contact position without bringing the surfaces into contact by using the secondary FECO patterns to obtain initial parameters for the thicknesses of the (epoxy or mica) spacer layers. This contact-free

calibration is pertinent to the use of the gSFB, as it was found that it is not always possible to perform a conventional contact calibration. The method allows other SFB experiments for which it is not feasible to bring the surfaces into contact prior to performing the measurement and thus enables a variety of new SFB experiments. The only disadvantage of this calibration method with respect to the use of spacers of non-uniform thickness, is that only a single location on the cross-cylindrical lenses can be used, as changing the measurement spot would require the system to be calibrated again.

The remarkable increase in adhesive force between a bare epoxy surface and an epoxy surface supporting a single layer of sp^2-hybridized carbon was reported on the Chapter 5. It describes the measurement of surface and interfacial energies of graphene in dry nitrogen and various liquids using adhesion force measurements. In such experiments the two graphene-covered gSFB lenses are brought into contact and pulled apart against the deflection of a spring. The adhesion force at which the surfaces separate was measured by determining the pull-apart distance and converting this into a surface or interfacial energy using JKR-contact mechanics. The increase in adhesion force between the surfaces due to the presence of graphene is ascribed to the much higher polarizability of the free sp^2 electrons in graphene's π-orbitals. Strengths of the study, such as the small number of approximations in the contact mechanics model, and limitations, such as surface roughness, lattice incommensurability and the often occurring reduction of the adhesive force upon subsequent pull-offs due to defect formation, were discussed. The study presented the first direct measurement of graphene surface energy and allows for the determination of surface energies of other 2-dimensional materials as well.

Through the body of the thesis, several limitations to the use of the gSFB have been presented. Primarily, the apparent limited smoothness of the gSFB lens surface limits the measurement of surface forces to forces with relatively large length scales. Second, the large number of steps involved in the fabrication procedure renders the system vulnerable

to contamination. Third, due to the use of a contact-free calibration, only a single measurement spot is available per experiment. Therefore, whilst the gSFB may in principle be used to obtain valuable new insights into the physical properties of confined electrolytes, it may be too cumbersome to use in practice.

An alternative, viable SFB method for measuring surface force across electrolytes confined between two polarizable surfaces is presented in Chapter 6. Drawing on fabrication and analysis methods developed in this thesis, this final thesis chapter describes critical improvements to a 3-mirror SFB setup, originally proposed by Levins and Vanderlick in 1994 [20]. It identifies and explores different system parameters such as the thicknesses of the gold mirrors, the thickness of the epoxy spacer and refractive index mismatch between the epoxies and SFB lens material used, to determine the optimal system configuration. It also describes the experimental procedure. Chapter 6 concludes by considering the exciting potential for new experiments using this setup, such as: the investigation of surface forces across confined electrolytes between polarizable surfaces; the measurement of potential dependent friction; and friction between gold surfaces modified with self-assembled monolayers exposing different head groups.

In conclusion, the work presented in this thesis describes several different approaches towards SFB experiments in which the electrical potential of both surfaces may be controlled. The approaches presented concern modifications to the SFB lenses, rather than the apparatus, and allow optical changes between the surfaces to be monitored *in situ*. The use of graphene as polarizable material at the solid/electrolyte interface suffers from challenges with respect to the obtainable surface smoothness and the complexity of the multi-step fabrication procedure. The use of two template-stripped gold surfaces in a 3-mirror setup, provides a promising alternative which enables a plethora of new experiments and provides exciting prospects for future studies using the SFB.

Bibliography

[1] D. Tabor and R.H.S. Winterton. The Direct Measurement of Normal and Retarded van der Waals Forces. *Proc. R. Soc. Lond. A*, 312(1511):435–450, 1969.

[2] J.N. Israelachvili and D. Tabor. Measurement of van der Waals Dispersion Forces in the Range 1.4 to 130 nm. *Nat. Phys. Sci.*, 236:106, 1972.

[3] J.N Israelachvili. Thin film studies using multiple-beam interferometry. *J. Colloid Interface Sci.*, 44(2):259–272, 1973.

[4] Eugenia Kumacheva and Jacob Klein. Simple liquids confined to molecularly thin layers. II. Shear and frictional behavior of solidified films. *J. Chem. Phys.*, 108(16):7010, 1998.

[5] R.M. Pashley. DLVO and Hydration Forces between Mica Surfaces in Li+, Na+, K+, and Cs+ Electrolyte Solutions. *J. Coll. Interf. Sci.*, 83(2):531–546, 1981.

[6] J.N. Israelachvili and G.E. Adams. Direct measurement of long range forces between two mica surfaces in aqueous KNO3 solutions. *Nature*, 262:774–776, 1976.

[7] R.G. Horn and J.N. Israelachvili. Direct measurement of structural forces between two surfaces in a nonpolar liquid. *J. Chem. Phys.*, 75(3):1400–1411, 1981.

[8] Uri Raviv and Jacob Klein. Fluidity of Bound Hydration Layers. *Science*, 297:1540–1544, 2013.

[9] A.M. Smith, K.R.J. Lovelock, N.N. Gosvami, T. Welton, and S. Perkin. Quantized friction across ionic liquid thin films. *Phys. Chem. Chem. Phys.*, 15:15317–15320, 2013.

[10] Alexander M Smith, Alpha A Lee, and Susan Perkin. The Electrostatic Screening Length in Concentrated Electrolytes Increases with Concentration. *Phys. Chem. Lett.*, 7:2157–2163, 2016.

[11] Hugo K Christenson and Neil H Thomson. The nature of the air-cleaved mica surface. *Surf. Sci. Rep.*, 71(2):367–390, 2016.

[12] LR White. On the Deryaguin Approximation for the Interaction of Macrobodies. *J. Colloid Interface Sci.*, 95(1):286–288, 1983.

[13] Liraz Chai and Jacob Klein. Large Area, Molecularly Smooth (0.2 nm rms) Gold Films for Surface Forces and Other Studies. *Langmuir*, 23:7777–7783, 2007.

[14] Chun Hung Lui, Li Liu, Kin Fai Mak, George W Flynn, and Tony F Heinz. Ultraflat graphene. *Nature*, 462(November):339–341, 2009.

[15] Joelle Frechette and T Kyle Vanderlick. Double Layer Forces over Large Potential Ranges as Measured in an Electrochemical Surface Forces Apparatus. *Langmuir*, 17:7620–7627, 2001.

[16] Markus Valtiner, Xavier Banquy, Kai Kristiansen, George W Greene, and Jacob N Israelachvili. The Electrochemical Surface Forces Apparatus: The Effect of Surface Roughness, Electrostatic Surface Potentials, and Anodic Oxide Growth on Interaction Forces, and Friction between Dissimilar Surfaces in Aqueous Solutions. *Langmuir*, 28:13080–13093, 2012.

[17] Ran Tivony, Dan Ben Yaakov, Gilad Silbert, and Jacob Klein. Direct Observation of Confinement-Induced Charge Inversion at a Metal Surface. *Langmuir*, 31:12845–12849, 2015.

[18] Jason N Connor and Roger G Horn. Extending the surface force apparatus capabilities by using white light interferometry in reflection Extending the surface force apparatus capabilities by using white light interferometry in reflection. *Rev. Sci. Instrum.*, 74:4601–4606, 2003.

[19] Boaz Moeremans, Hsiu-wei Cheng, Qingyun Hu, Hector F Garces, Nitin P Padture, Frank Uwe Renner, and Markus Valtiner. Lithium-ion battery electrolyte mobility at nano-confined graphene interfaces. *Nat. Commun.*, 7:1–7, 2016.

[20] Kyle T Vanderlick and John M Levins. Extended Spectral Analysis of Multiple Beam Interferometry: A Technique To Study Metallic Films in the Surface Forces Apparatus. *Langmuir*, 10(7):2389–2394, 1994.

[21] Hiroshi Kawai, Hiroshi Sakuma, Masashi Mizukami, Takashi Abe, Yasuhiro Fukao, Haruo Tajima, Hiroshi Kawai, Hiroshi Sakuma, Masashi Mizukami, Takashi Abe, and Yasuhiro Fukao. New surface forces apparatus using two-beam interferometry New surface forces apparatus using two-beam interferometry. *Rev. Sci. Instrum.*, 79, 2008.

[22] M Kasuya and K Kurihara. Novel Surface Forces Apparatus for Characterizing Solid-Liquid Interfaces. *Electrochem. Soc. Japan*, 82:317–321, 2014.

[23] Mirijam Zobel, Reinhard B Neder, and Simon A J Kimber. Universal solvent restructuring induced by colloidal nanoparticles. *Science*, 347(6219):201–204, 2015.

[24] Rob Atkin, Natalia Borisenko, Marcel Drüschler, Frank Endres, Robert Hayes, Benedikt Huber, and Bernhard Roling. Structure and dynamics of the interfacial layer between ionic liquids and electrode materials. *J. Mol. Liq.*, 192:44–54, 2014.

[25] Léo Garcia, Chloé Barraud, Cyril Picard, Jérôme Giraud, Elisabeth Charlaix, Benjamin Cross, Léo Garcia, Chloé Barraud, Cyril Picard, Jérôme Giraud, Elisabeth Charlaix, and Benjamin Cross. A micro-nano-rheometer for the mechanics of soft matter at interfaces A micro-nano-rheometer for the mechanics of soft matter at interfaces. *Rev. Sci. Instrum.*, 87(113906), 2016.

[26] Konstantin S Novoselov, A K Geim, S V Morozov, D Jiang, Y Zhang, S V Dubonos, I V Grigorieva, and A A Firsov. Electric Field Effect in Atomically Thin Carbon Films. *Science*, 306(5696):666–669, 2004.

[27] Xuesong Li, Weiwei Cai, Jinho An, Seyoung Kim, Junghyo Nah, Dongxing Yang, Richard Piner, Aruna Velamakanni, Inhwa Jung, Emanuel Tutuc, Sanjay K Banerjee, Luigi Colombo, and Rodney S Ruoff. Large-Area Synthesis of High-Quality Graphene Films on Copper Foils. *Science*, 324:1312–1314, 2009.

[28] Cecilia Mattevi and Manish Chhowalla. A review of chemical vapour deposition of graphene on copper †. *J. Mater. Chem.*, 21:3324–3334, 2011.

[29] Alexander E Karu and Michael Beer. Pyrolytic Formation of Highly Crystalline Graphite Films. *J. Appl. Phys.*, 37:2179–2181, 1966.

[30] Wenhua Zhang, Ping Wu, Zhenyu Li, and Jinlong Yang. First-Principles Thermodynamics of Graphene Growth on Cu Surfaces. *J. Phys. Chem. C*, 115:17782–17787, 2011.

[31] Robert G Van Wesep, Hua Chen, Wenguang Zhu, Zhenyu Zhang, Robert G Van Wesep, Hua Chen, Wenguang Zhu, and Zhenyu Zhang. Communication : Stable carbon nanoarches in the initial stages of epitaxial growth of graphene on Cu (111) Communication : Stable carbon nanoarches in the initial stages of epitaxial growth of graphene on Cu (111). 171105(111), 2011.

[32] Hokwon Kim, Cecilia Mattevi, M Reyes Calvo, Jenny C Oberg, Luca Artiglia, Stefano Agnoli, Cyrus F Hirjibehedin, Manish Chhowalla, Eduardo Saiz, and K I M E T Al. Activation Energy Paths for Graphene Nucleation and Growth on Cu. *ACS Nano*, 6(4):3614–3623, 2012.

[33] Ivan Vlassiouk, Murari Regmi, Pasquale Fulvio, Sheng Dai, Panos Datskos, Gyula Eres, and Sergei Smirnov. Role of Hydrogen in Chemical Vapor Deposition Growth of Large Single-Crystal Graphene. *ACS Nano*, 5(7):6069–6076, 2011.

[34] Martin Kalbac, Otakar Frank, and Ladislav Kavan. The control of graphene double-layer formation in copper- catalyzed chemical vapor deposition. *Carbon*, 50(10):3682–3687, 2012.

[35] Bin Wu, Dechao Geng, Zhiping Xu, Yunlong Guo, Liping Huang, Yunzhou Xue, Jianyi Chen, Gui Yu, and Yunqi Liu. Self-organized graphene crystal patterns. *NPG Asia Mater.*, 5, 2013.

[36] Yufeng Hao, M S Bharathi, Lei Wang, Yuanyue Liu, Hua Chen, Shu Nie, Xiaohan Wang, Harry Chou, Cheng Tan, Babak Fallahazad, H Ramanarayan, Carl W Magnuson, Emanuel Tutuc, Boris I Yakobson, Kevin F Mccarty, Yong-wei Zhang, Philip Kim, James Hone, Luigi Colombo, and Rodney S Ruoff. The Role of Surface Oxygen in the Growth of Large Single-Crystal Graphene on Copper. *Science*, 342:720–724, 2013.

[37] G. Eres, M. Regmi, C.M. Rouleau, J. Chen, I.N. Ivanov, A.A. Puretzky, and D.B. Geohegan. Cooperative Island Growth of on Copper Using Chemical Vapor Deposition. *ACS Nano*, 8(6):5657–5669, 2014.

[38] Wei Huang, Zhi-fei Liu, and Zhi-yong Yang. Top or underneath ? Revealing the structure of multilayer graphene domains with atomic force microscopy and theoretical analysis. *Carbon*, 99:131–137, 2016.

[39] D.R. Lide. *CRC Handbook of Chemistry and Physics*. CRC Press LCC, 84th edition, 2013.

[40] Ivan Vlassiouk, Sergei Smirnov, Murari Regmi, Sumedh P Surwade, Nishtha Srivastava, Randall Feenstra, Gyula Eres, Chad Parish, Nick Lavrik, Panos Datskos, Sheng Dai, and Pasquale Fulvio. Graphene Nucleation Density on Copper : Fundamental Role of Background Pressure. *J. Phys. Chem. C*, 117:18919–18926, 2013.

[41] Zheng Yan, Jian Lin, Zhiwei Peng, Zhengzong Sun, Yu Zhu, Lei Li, Changsheng Xiang, E Loı, Carter Kittrell, and James M Tour. Toward the Synthesis of Wafer-Scale Single-Crystal Graphene on Copper Foils. *ACS Nano*, 6(10):9110–9117, 2012.

[42] Zhengtang Luo, Ye Lu, Daniel W Singer, Matthew E Berck, Luke A Somers, Brett R Goldsmith, and A T Charlie Johnson. Effect of Substrate Roughness and Feedstock Concentration on Growth of Wafer-Scale Graphene at Atmospheric Pressure. *Chem. Mater.*, 23:1441–1447, 2011.

[43] Gang Hee Han, Jung Jun Bae, Eun Sung Kim, Seung Jin Chae, Hyeon-jin Shin, Jae-young Choi, Didier Pribat, and Young Hee Lee. Influence of Copper Morphology in Forming Nucleation Seeds for Graphene Growth. *Nano Lett.*, 11:4144–4148, 2011.

[44] Hong Wang, Guanzhong Wang, Pengfei Bao, Shaolin Yang, Wei Zhu, Xing Xie, and Wen-jun Zhang. Controllable Synthesis of Submillimeter Single-Crystal Monolayer Graphene Domains on Copper Foils by Suppressing Nucleation. *J. Am. Chem. Soc.*, 134:3627–3630, 2012.

[45] Ali Mohsin, Lei Liu, Peizhi Liu, Wan Deng, Ilia N Ivanov, Guoliang Li, Ondrej E Dyck, and Gerd Duscher. Synthesis of Millimeter-Size Hexagon-Shaped Graphene Single Crystals on Resolidi fi ed Copper. *ACS Nano*, 7(10):8924–8931, 2013.

[46] Adrian T Murdock, Christian D Van Engers, Jude Britton, Vitaliy Babenko, Seyyed Shayan Meysami, Hugh Bishop, Alison Crossley, Antal A Koos, and Nicole Grobert. Targeted removal of copper foil surface impurities for improved synthesis of CVD graphene. *Carbon*, 122:207–216, 2017.

[47] Adrian T Murdock, Antal Koos, T Ben Britton, Lothar Houben, Tim Batten, Tong Zhang, Angus J Wilkinson, Rafal E Dunin-borkowski, Christina E Lekka, Nicole Grobert, and Murdock E T Al. Controlling the Orientation , Edge Geometry , and Thickness of Chemical Vapor Deposition Graphene. *ACS Nano*, 7(2):1351–1359, 2013.

[48] Hak Ki Yu, Kannan Balasubramanian, Kisoo Kim, Jong-lam Lee, Manisankar Maiti, Claus Ropers, Janina Krieg, Klaus Kern, and Alec M Wodtke. Chemical Vapor Deposition of Graphene on a "Peeled-O ff " Epitaxial Cu (111) Foil : A Simple Approach to Improved Properties. *ACS Nano*, 8(8):8636–8643, 2014.

[49] Dechao Geng, Bin Wu, Yunlong Guo, Liping Huang, Yunzhou Xue, Jianyi Chen, Gui Yu, and Lang Jiang. Uniform hexagonal graphene flakes and films grown on liquid copper surface. *Proc. Nat. Acad. Sci.*, 109(21):7992–7996, 2012.

[50] Philipp Braeuninger-weimer, Barry Brennan, Andrew J Pollard, and Stephan Hofmann. Understanding and Controlling Cu-Catalyzed Graphene Nucleation: The Role of Impurities, Roughness, and Oxygen Scavenging. *Chem. Mater.*, 28:8905–8915, 2016.

[51] Andrea Cabrero-vilatela, Robert S Weatherup, Philipp Braeuninger-weimer, Sabina Caneva, and Stephan Hofmann. Towards a general growth model for graphene CVD on transition metal catalysts. *Nanoscale*, 8:2149–2158, 2016.

[52] K S Novoselov, A K Geim, S V Morozov, D Jiang, M I Katsnelson, I V Grigorieva, and S V Dubonos. Two-dimensional gas of massless Dirac fermions in graphene. *Nature*, 438(November):197–200, 2005.

[53] Andrea C Ferrari and Denis M Basko. Raman spectroscopy as a versatile tool for studying the properties of graphene. *Nat. Publ. Gr.*, 8(4):235–246, 2013.

[54] P H Tan, W P Han, W J Zhao, Z H Wu, K Chang, H Wang, Y F Wang, N Bonini, N Marzari, N Pugno, G Savini, A Lombardo, and A C Ferrari. The shear mode of multilayer graphene. *Nat. Mater.*, 11(4):294–300, 2012.

[55] A C Ferrari, J C Meyer, V Scardaci, C Casiraghi, M Lazzeri, F Mauri, S Piscanec, D Jiang, K S Novoselov, S Roth, and A K Geim. Raman Spectrum of Graphene and Graphene Layers. *Phys. Rev. Lett.*, 97(187401):1–4, 2006.

[56] Kwanpyo Kim, Sinisa Coh, Liang Z Tan, William Regan, Jong Min Yuk, Eric Chatterjee, M F Crommie, Marvin L Cohen, Steven G Louie, and A Zettl. Raman Spectroscopy Study of Rotated Double-Layer Graphene : Misorientation-Angle Dependence of Electronic Structure. *Phys. Rev. Lett.*, 108(246103):1–6, 2012.

[57] A Jorio, E H Martins Ferreira, F Stavale, C A Achete, R B Capaz, M V O Moutinho, A Lombardo, T S Kulmala, and A C Ferrari. Quantifying Defects in Graphene via Raman Spectroscopy at Different Excitation Energies. *Nano Lett.*, 11:3190–3196, 2011.

[58] Duhee Yoon, Hyerim Moon, Young-woo Son, Jin Sik Choi, Bae Ho Park, and Young Hun Cha. Interference effect on Raman spectrum of graphene on SiO2/Si. *Phys. Rev. B*, 80(125422):1–6, 2009.

[59] Ying Wang, Zhen Ni, Ting Yu, Ze Xiang Shen, Hao Wang, Yi Wu, Wei Chen, Andrew Thye, and Shen Wee. Raman Studies of Monolayer Graphene : The Substrate Effect. *J. Phys. Chem. C*, 112:10637–10640, 2008.

[60] F Tuinstra and J L Koenig. Raman Spectrum of Graphite. *J. Chem. Phys.*, 53:1126–1130, 1970.

[61] L M Malard, M A Pimenta, G Dresselhaus, and M S Dresselhaus. Raman spectroscopy in graphene. *Phys. Rep.*, 473:51–87, 2009.

[62] Patrick May, Michele Lazzeri, Felix Herziger, Gordon Callsen, Juan S Reparaz, Axel Hoffmann, Francesco Mauri, and Janina Maultzsch. Signature of the two-dimensional phonon dispersion in graphene probed by double-resonant Raman scattering. *Phys. Rev. B*, 075402:1–6, 2013.

[63] A Gupta, G Chen, P Joshi, S Tadigadapa, and P C Eklund. Raman Scattering from High-Frequency Phonons in Supported n-Graphene Layer Films. *Nano Lett.*, 6(12):2667–2673, 2006.

[64] Vidya Kochat, Nath Pal, E S Sneha, Arjun Sampathkumar, and Anshita Gairola. High contrast imaging and thickness determination of graphene with in-column secondary electron microscopy. *J. Appl. Phys.*, 110(014315):1–5, 2011.

[65] Hidefumi Hiura, Hisao Miyazaki, and Kazuhito Tsukagoshi. Determination of the Number of Graphene Layers: Discrete Distribution of the Secondary Electron Intensity Stemming from Individual Graphene Layers. *Appl. Phys. Expr.*, 3(095101):1–3, 2010.

[66] L. Reimer. *Image formation in low-voltage scanning electron microscopy, SPIE tutorial texts in Optical Engineering, Vol. TT12.* Bellingham, WA, 1993.

[67] J Scott Bunch, Scott S Verbridge, Jonathan S Alden, Arend M Van Der Zande, Jeevak M Parpia, Harold G Craighead, and Paul L Mceuen. Impermeable Atomic Membranes from Graphene Sheets. *Nano Lett.*, 8:3–7, 2008.

[68] Zhijiang Ye and Ashlie Martini. Atomic friction at exposed and buried graphite step edges : Experiments and Atomic friction at exposed and buried graphite step edges : Experiments and simulations. *Appl. Phys. Lett.*, 106:231603, 2015.

[69] Hyunsoo Lee, Han-Bo-Ram Lee, Sangku Kwon, Miquel Salmeron, and Jeong Young Park. Internal and External Atomic Steps in Graphite Exhibit Dramatically Di ff erent Physical and Chemical Properties. *ACS Nano*, 9(4):3814–3819, 2015.

[70] Qiongyu Li, Harry Chou, Jin-hui Zhong, Jun-yang Liu, Andrei Dolocan, Junyan Zhang, Yinghui Zhou, Rodney S Ruo, Shanshan Chen, and Weiwei Cai. Growth of Adlayer Graphene on Cu Studied by Carbon Isotope Labeling. *Nano Lett.*, 13:486–490, 2013.

[71] Wenjing Fang, Allen L Hsu, Roman Caudillo, Yi Song, A Glen Birdwell, Eugene Zakar, Martin Kalbac, Madan Dubey, Millie S Dresselhaus, and Paulo T Araujo. Rapid Identi fi cation of Stacking Orientation in Isotopically Labeled Chemical-Vapor Grown Bilayer Graphene by Raman Spectroscopy. *Nano Lett.*, 13:1541–1548, 2013.

[72] Xiuyun Zhang, Lu Wang, John Xin, Boris I Yakobson, and Feng Ding. Role of Hydrogen in Graphene Chemical Vapor Deposition Growth on a Copper Surface. *J. Am. Chem. Soc.*, 136(8):3040–3047, 2014.

[73] Ivan Vlassiouk, Pasquale Fulvio, Harry Meyer, Nick Lavrik, Sheng Dai, Panos Datskos, and Sergei Smirnov. Large scale atmospheric pressure chemical vapor deposition of graphene. *Carbon*, 54:58–67, 2013.

[74] Lili Fan, Kunlin Wang, Jinquan Wei, Minlin Zhong, Dehai Wu, and Hongwei Zhu. Correlation between nanoparticle location and graphene nucleation in chemical vapour deposition of graphene. *J. Mater. Chem. A*, 2:13123–13128, 2014.

[75] Dechao Geng, Lan Meng, Bingyan Chen, Enlai Gao, Wei Yan, Hui Yan, Birong Luo, Jie Xu, Huaping Wang, Zupan Mao, Zhiping Xu, Lin He, and Zhiyong Zhang. Controlled Growth of Single-Crystal Twelve-Pointed Graphene Grains on a Liquid Cu Surface. *Adv. Mater.*, 26:6423–6429, 2014.

[76] Gwan-hyoung Lee, Ryan C Cooper, Sung Joo An, Sunwoo Lee, Arend Van Der Zande, Nicholas Petrone, Alexandra G Hammerberg, Changgu Lee, Bryan Crawford, Warren Oliver, Jeffrey W Kysar, and James Hone. High-Strength Chemical-Vapor – Deposited Graphene and Grain Boundaries. *Science*, 340:1073–1077, 2013.

[77] Dae Woo Kim, Yun Ho Kim, Hyeon Su Jeong, and Hee-tae Jung. Direct visualization of large-area graphene domains and boundaries by optical birefringency. *Nat. Nanotechnol.*, 7:29–34, 2012.

[78] Jong-ho Son, Seung-jae Baeck, Min-ho Park, Jae-bok Lee, Cheol-woong Yang, Jang-kun Song, Wang-cheol Zin, and Jong-hyun Ahn. Detection of graphene domains and defects using liquid crystals. *Nat. Commun.*, 5:1–7, 2014.

[79] Susan Perkin, Liraz Chai, Nir Kampf, Uri Raviv, Wuge Briscoe, Iain Dunlop, Simon Titmuss, Minseok Seo, Eugenia Kumacheva, and Jacob Klein. Forces between Mica Surfaces, Prepared in Different Ways, Across Aqueous and Nonaqueous Liquids Confined to Molecularly Thin Films. *Langmuir*, 22(14):6142–6152, 2006.

[80] Gang Hee Han, Jung Jun Bae, Eun Sung Kim, Seung Jin Chae, Hyeon-jin Shin, Jae-young Choi, Didier Pribat, and Young Hee Lee. Influence of Copper Morphology in Forming Nucleation Seeds for Graphene Growth. *Nano Lett.*, 11:4144–4148, 2011.

[81] Qingkai Yu, Luis A. Jauregui, Wei Wu, Robert Colby, Jifa Tian, Zhihua Su, Helin Cao, Zhihong Liu, Deepak Pandey, Dongguang Wei, Ting Fung Chung, Peng Peng, Nathan P. Guisinger, Eric A. Stach, Jiming Bao, Shin-Shem Pei, and Yong P. Chen. Control and characterization of individual grains and grain boundaries in graphene grown by chemical vapour deposition. *Nat. Mater.*, 10(6):443–449, 2011.

[82] Lin Gan and Zhengtang Luo. Turning off Hydrogen To Realize Seeded Growth of Subcentimeter Single-Crystal Graphene Grains on Copper. *ACS Nano*, 7(10):9480–9488, 2013.

[83] Tomohiro Yasunishi, Yuya Takabayashi, Shigeru Kishimoto, Ryo Kitaura, Hisanori Shinohara, and Yutaka Ohno. Origin of residual particles on transferred graphene grown by CVD. *Jpn. J. Appl. Phys.*, 55:080305, 2016.

[84] Zhu-Jun Wang, Gisela Weinberg, Qiang Zhang, Thomas Lunkenbein, Achim Klein-Hoffmann, Michalina Kurnatowska, Milivoj Plodinec, Qing Li, Lifeng Chi, R Schloegl, and Marc-georg Willinger. Direct Observation of Graphene Growth and Associated Copper Substrate Dynamics by in Situ Scanning Electron Microscopy. *ACS Nano*, 9(2):1506–1519, 2015.

[85] Soo Min Kim, Allen Hsu, Yi-hsien Lee, Mildred Dresselhaus, Ki Kang Kim, and Jing Kong. The effect of copper pre-cleaning on graphene synthesis. *Nanotechnology*, 24:365602, 2013.

[86] Jude Britton, Nico E A Cousens, Samuel W Coles, Christian D Van Engers, Vitaliy Babenko, Adrian T Murdock, Antal Koo, Susan Perkin, and Nicole Grobert. A Graphene Surface Force Balance. *Langmuir*, 30:11485–11492, 2014.

[87] Jacob N. Israelachvili. *Intermolecular and Surface Forces*. Elsevier, Kidlington, 3 edition, 2011.

[88] Mingguang Chen, Robert C Haddon, Ruoxue Yan, and Elena Bekyarova. Materials Horizons Advances in transferring chemical vapour deposition graphene: a review. *Mater. Horizons*, 2017.

[89] Alessia Matruglio, Silvia Nappini, Denys Naumenko, Elena Magnano, Federica Bondino, Marco Lazzarino, and Simone Dal Zilio. Contamination-free suspended graphene structures by a Ti-based transfer method. *Carbon*, 103:305–310, 2016.

[90] A Capasso, M De Francesco, E Leoni, T Dikonimos, F Buonocore, L Lancellotti, E Bobeico, M S Sarto, G De Bellis, and N Lisi. Cyclododecane as support material for clean and facile transfer of large-area few-layer graphene. *Appl. Phys. Lett.*, 105(113101):1–4, 2014.

[91] Mingguang Chen, Dejan Stekovic, and Wangxiang Li. Sublimation-assisted graphene transfer technique based on small polyaromatic hydrocarbons. *Nanotechnology*, 28(255701):1–6, 2017.

[92] Di-yan Wang, I-sheng Huang, Po-hsun Ho, Shao-sian Li, Yun-chieh Yeh, Duan-wei Wang, Wei-liang Chen, Yu-yang Lee, Yu-ming Chang, Chia-chun Chen, Chi-te Liang, and Chun-wei Chen. Clean-Lifting Transfer of Large-area Residual-Free Graphene Films. *Adv. Mater.*, 25:4521–4526, 2013.

[93] Luiz G P Martins, Yi Song, Tingying Zeng, Mildred S Dresselhaus, Jing Kong, and Paulo T Araujo. Direct transfer of graphene onto flexible substrates. *Proc. Nat. Acad. Sci.*, 110(44):17762–17767, 2013.

[94] Guilhermino J M Fechine, Inigo Martin-Fernandez, George Yiapanis, Ricardo Bentini, Eeshan Sandeep Kulkarni, Ricardo V. Bof de Oliveira, Xiao Hu, Irene Yarovsky, Antonio H. Castro Neto, and Barbaros Ozyilmaz. Direct dry transfer of chemical vapor deposition graphene to polymeric substrates. *Carbon*, 83:224–231, 2015.

[95] Wei-Hsiang Lin, Ting-Hui Chen, Jan-Kai Chang, Jieh-I Taur, Yuan-Yen Lo, Wei-Li Lee, Chia-Seng Chang, Wei-Bin Su, and Chih-I Wu. A Direct and Polymer-Free Method for Transferring Graphene Grown by Chemical Vapor Deposition to Any Substrate. *ACS Nano*, 8(2):1784–1791, 2014.

[96] Guohui Zhang, Aleix G Gu, Paul M Kirkman, Robert A Lazenby, Thomas S Miller, and Patrick R Unwin. Versatile Polymer-Free Graphene Transfer Method and Applications. *ACS Appl. Mater. Interfaces*, 8:8008–8016, 2016.

[97] C Casiraghi, A Hartschuh, E Lidorikis, H Qian, H Harutyunyan, and T Gokus. Rayleigh Imaging of Graphene and Graphene Layers. *Nano Lett.*, 7(9):2711–2717, 2007.

[98] P Blake, E W Hill, A H Castro Neto, K S Novoselov, D Jiang, R Yang, T J Booth, A K Geim, P Blake, and E W Hill. Making graphene visible. *Appl. Phys. Lett.*, 91(063124):1–3, 2007.

[99] J P Berry. Fracture Processes in Polymeric Materials . V. Dependence of the Ultimate Properties of Poly (methyl Methacrylate) on Molecular Weight. *J. Polym. Sci.*, 2:4069–4076, 1964.

[100] K Jordens, G L Wilkes, J Janzen, D C Rohlfing, and M B Welch. The influence of molecular weight and thermal history on the thermal, rheological, and mechanical properties of metallocene-catalyzed linear polyethylenes. *Polymer*, 41:7175–7192, 2000.

[101] G Carbone, L Mangialardi, and B N J Persson. Adhesion between a thin elastic plate and a hard randomly rough substrate. *Phys. Rev. B*, 70(125407):1–10, 2004.

[102] Ji Won Suk, Alexander Kitt, Carl W Magnuson, Yufeng Hao, Samir Ahmed, Jinho An, Anna K Swan, Bennett B Goldberg, and Rodney S Ruoff. Transfer of CVD-Grown Monolayer Graphene onto Arbitrary Substrates. *ACS Nano*, 5(9):6916–6924, 2011.

[103] Jie Song, Fong-Yu Kam, Rui-Qi Png, Wei-Ling Seah, Jing-Mei Zhuo, Geok-Kieng Lim, Peter K H Ho, and Lay-Lay Chua. A general method for transferring graphene onto soft surfaces. *Nat. Nanotechnol.*, 8(5):356–62, 2013.

[104] Hyun Ho Kim, Seong Kyu Lee, Seung Goo Lee, Eunho Lee, and Kilwon Cho. Wetting-Assisted Crack- and Wrinkle-Free Transfer of Wafer-Scale Graphene onto Arbitrary Substrates over a Wide Range of Surface Energies. *Adv. Funct. Mater.*, 26:2070–2077, 2016.

[105] Xuesong Li, Yanwu Zhu, Weiwei Cai, Mark Borysiak, Boyang Han, David Chen, Richard D Piner, Luigi Colombo, and Rodney S Ruoff. Transfer of Large-Area Graphene Films for High-Performance Transparent Conductive Electrodes. *Nano Lett.*, 9:4359–4363, 2009.

[106] Xuelei Liang, Brent A Sperling, Irene Calizo, Guangjun Cheng, Christina Ann Hacker, Qin Zhang, Yaw Obeng, Kai Yan, Hailin Peng, Qiliang Li, Xiaoxiao Zhu, Hui Yuan, Angela R Hight Walker, Zhongfan Liu, Lian-mao Peng, and Curt A Richter. Toward Clean and Crackless Transfer of Graphene. *ACS Nano*, 5(11):9144–9153, 2011.

[107] Jin-yong Hong, Yong Cheol Shin, Ahmad Zubair, Yunwei Mao, Tomás Palacios, Mildred S Dresselhaus, Sung Hyun Kim, and Jing Kong. A Rational Strategy for Graphene Transfer on Substrates with Rough Features. *Adv. Mater.*, 28:2382–2392, 2016.

[108] A Pirkle, J Chan, A Venugopal, D Hinojos, C W Magnuson, S McDonnell, L Colombo, E M Vogel, R S Ruoff, and R M Wallace. The effect of chemical residues on the physical and electrical properties of chemical vapor deposited graphene transferred to SiO2. *Appl. Phys. Lett.*, 99(122108):1–5, 2011.

[109] J Manjkow, J S Papanu, D W Hess, D S Soane Soong, and A T Bell. Influence of Processing and Molecular Parameters on the Dissolution Rate of Poly- (Methyl Methacrylate) Thin Films. *J. Electrochem. Soc.*, 134(8):2003–2007, 1987.

[110] J S Papanu, D W Hess, D S Soane, and A T Bell. Dissolution of Thin Poly (methyl methacrylate) Films in Ketones , Binary Ketone / Alcohol Mixtures , and Hydroxy Ketones. *J. Electrochem. Soc.*, 136(10):3077–3083, 1989.

[111] H Richardson, M Sferrazza, and J L Keddie. EPJ E direct electronic only Influence of the glass transition on solvent loss from spin-cast glassy polymer thin films. *Eur. Phys. J. E*, 12(1):87–91, 2003.

[112] I Yu Evchuk, R I Musii, R G Makitra, and R E Pristanskii. Solubility of Polymethyl Methacrylate in Organic Solvents. *Russ. J. Appl. Chem.*, 78(10):1576–1580, 2005.

[113] J L Keddie, M Sferrazza, and John Wiley. Probing the early stages of solvent evaporation and relaxation in solvent-cast polymer thin films by spectroscopic ellipsometry. *Surf. Interf. Anal.*, 43:1448–1452, 2011.

[114] Gabriela Borin, Yi Song, Iara De Fa, Antonio Gomes, Souza Filho, Ledjane Silva, and Jing Kong. Optimized graphene transfer : Influence of polymethylmethacrylate (PMMA) layer concentration and baking time on graphene final performance. *Carbon*, 84:82–90, 2015.

[115] Seonyeong Kim, Somyeong Shin, Taekwang Kim, Hyewon Du, Minho Song, Changwon Lee, Kisoo Kim, Seungmin Cho, David H Seo, and Sunae Seo. Robust graphene wet transfer process through low molecular weight polymethylmethacrylate. *Carbon*, 98:352–357, 2016.

[116] Zengguang Cheng, Qiaoyu Zhou, Chenxuan Wang, Qiang Li, Chen Wang, and Ying Fang. Toward Intrinsic Graphene Surfaces : A Systematic Study on Thermal Annealing and Wet-Chemical Treatment of SiO2-Supported Graphene Devices. *Nano Lett.*, 11:767–771, 2011.

[117] Hee Jin, Ho Young, Seung Yol, Joong Tark, Kang-jun Baeg, Jun Yeon, and Geon-woong Lee. Improved transfer of chemical-vapor-deposited graphene through modification of intermolecular interactions and solubility of poly (methylmethacrylate) layers. *Carbon*, 66:612–618, 2013.

[118] Malkolm Hinnemo, Patrick Ahlberg, Carl Hagglund, Wencai Ren, Hui-ming Cheng, Shi-li Zhang, and Zhi-bin Zhang. Scalable residue-free graphene for surface-enhanced Raman scattering. *Carbon*, 98:567–571, 2016.

[119] Kunpeng Jia, Jun Luo, Rongyan Hu, Jun Zhan, Heshi Cao, Yajuan Su, Huilong Zhu, Ling Xie, Chao Zhao, Dapeng Chen, and Tianchun Ye. Evaluation of PMMA Residues as a Function of Baking Temperature and a Graphene Heat-Free-Transfer Process to Reduce Them. *ECS J. Solid State Sc. Techn.*, 5(3):138–141, 2016.

[120] Joshua D Wood, Gregory P Doidge, Enrique A Carrion, Justin C Koepke, Joshua A Kaitz, Isha Datye, Ashkan Benham, Jayan Hewaparakrama, Basil Aruin, Yaofeng Chen, Hefei Dong, Richard T Haasch, Joseph W Lyding, and Eric Pop. Annealing free, clean graphene transfer using alternative polymer scaffolds. *Nanotechnology*, 26(055302):1–9, 2015.

[121] Christian Pick, Christopher Argento, German Drazer, and Joelle Frechette. Micropatterned Charge Heterogeneities via Vapor Deposition of Aminosilanes. *Langmuir*, 31:70725–10733, 2015.

[122] Daniel J Graham, David D Price, and Buddy D Ratner. Solution Assembled and Microcontact Printed Monolayers of Dodecanethiol on Gold : A Multivariate Exploration of Chemistry and Contamination. *Langmuir*, 18(5):1518–1527, 2002.

[123] Werner Kern. The Evolution of Silicon Wafer Cleaning Technology. *J. Elec*, 137(6):1887–1891, 1990.

[124] H-J Butt, D N Wang, P K Hansma, and W Kuhlbrandt. Effect of surface roughness of carbon support films on high- resolution electron diffraction of two-dimensional protein crystals. *Ultramicroscopy*, 36:307–318, 1991.

[125] Jason J Blackstock, Zhiyong Li, Mark R Freeman, and Duncan R Stewart. Ultra-flat platinum surfaces from template-stripping of sputter deposited films. *Surf. Sci.*, 546:87–96, 2003.

[126] Ran Tivony and Jacob Klein. Probing the Surface Properties of Gold at Low Electrolyte Concentration. *Langmuir*, 32(7346-7355), 2016.

[127] Nagaiyanallur V Venkataraman, Jia Pei, V M Cremmel, Antonella Rossi, and Nicholas D Spencer. Template-Stripped, Ultraflat Gold Surfaces with Coplanar, Embedded Titanium Micropatterns. *Langmuir*, 29:9935–9943, 2013.

[128] Kevin M McPeak, Sriharsha V Jayanti, Stephan J P Kress, Stefan Meyer, Stelio Iotti, Aurelio Rossinelli, and David J Norris. Plasmonic Films Can Easily Be Better: Rules and Recipes. *ACS Photonics*, 2:326–333, 2015.

[129] Hexion. EPON Resin 1004F, technical data sheet.

[130] Gunther Reiter, Moustafa Hamieh, Pascal Damman, S Everine, Sylvain Gabriele, Thomas Vilmin, and Elie Rapha El. Residual stresses in thin polymer films cause rupture and dominate early stages of dewetting. *Nat. Mater.*, 4:754–758, 2005.

[131] Hu Lin, Andre Schilo, A Rauf Kamoka, Nikolai Severin, Igor M Sokolov, and Jürgen P Rabe. Insight into the wetting of a graphene-mica slit pore with a monolayer of water. *Phys. Rev. B*, 95(195414):1–7, 2017.

[132] O Ochedowski, B Kleine Bussmann, and M Schleberger. Graphene on Mica - Intercalated Water Trapped for Life. *Sci. Rep.*, 4(6003):1–6, 2014.

[133] Pantelis Bampoulis, Detlef Lohse, Harold J W Zandvliet, and Bene Poelsema. Coarsening dynamics of ice crystals intercalated between graphene and supporting mica. *Appl. Phys. Lett.*, 108(011601):1–4, 2016.

[134] MT Clarkson. Multiple-beam interferometry with thin metal films and unsymmetrical systems. *J. Phys. D. Appl. Phys.*, 22:475–482, 1989.

[135] Roger G Horn and Douglas T Smith. Analytic solution for the three-layer multiple beam interferometer. *Appl. Opt.*, 30(1):59–65, 1991.

[136] Born and Wolf. Principles Of Optics. page 859, 1970.

[137] M Heuberger. The extended surface forces apparatus . Part I . Fast spectral correlation interferometry. *Rev. Sci. Instrum.*, 72(3):1700–1707, 2001.

[138] Daniel F Kienle and Tonya L Kuhl. Analyzing Refractive Index Profiles of Confined Fluids by Interferometry. *Anal. Chem.*, 86:11860–11867, 2014.

[139] Marina Ruths, Manfred Heuberger, Volker Scheumann, Jianjiang Hu, and Wolfgang Knoll. Confinement-Induced Film Thickness Transitions in Liquid Crystals between Two Alkanethiol Monolayers on Gold. *Langmuir*, 17:6213–6219, 2001.

[140] Daniel F Kienle and Tonya L Kuhl. Analytica Chimica Acta Analyzing refractive index pro fi les of con fi ned fl uids by interferometry part II : Multilayer and asymmetric systems. *Anal. Chim. Acta*, 936:236–244, 2016.

[141] M. Heuberger, G. Luengo, and J. Israelachvili. Topographic Information from Multiple Beam Interferometry in the Surface Forces Apparatus. *Langmuir*, 13(14):3839–3848, 1997.

[142] Kevin M McPeak, Sriharsha V Jayanti, Stephan J P Kress, Stefan Meyer, Stelio Iotti, Aurelio Rossinelli, and David J Norris. Plasmonic Films Can Easily Be Better: Rules and Recipes. *ACS Photonics*, 2:326–333, 2015.

[143] Christian D van Engers, Nico E A Cousens, Vitaliy Babenko, Jude Britton, Bruno Zappone, Nicole Grobert, and Susan Perkin. Direct Measurement of the Surface Energy of Graphene. *Nano Lett.*, 17:3815–3821, 2017.

[144] Marco Balabajew, Christian D Van Engers, and Susan Perkin. Contact-free calibration of an asymmetric multi-layer interferometer for the surface force balance Contact-free calibration of an asymmetric multi-layer interferometer for the surface force balance. *Rev. Sci. Instrum.*, 88:123903, 2017.

[145] Susan Perkin. Ionic liquids in confined geometries. *Phys. Chem. Chem. Phys.*, 14:5052–5062, 2012.

[146] Daniel F Kienle, João V De Souza, Erik B Watkins, and Tonya L Kuhl. Thickness and refractive index of DPPC and DPPE monolayers by multiple-beam interferometry. *Anal Bioanal Chem*, 406:4725–4733, 2014.

[147] Rob Atkin, Sherif Zein, El Abedin, Robert Hayes, Luiz H S Gasparotto, Natalia Borisenko, and Frank Endres. AFM and STM Studies on the Surface Interaction of [BMP]TFSA and [EMIm]TFSA Ionic Liquids with Au (111). *J. Phys. Chem. C*, 113:13266–13272, 2009.

[148] Robert Hayes, Sherif Zein, El Abedin, and Rob Atkin. Pronounced Structure in Confined Aprotic Room-Temperature Ionic Liquids. *J. Phys. Chem. B*, 113:7049–7052, 2009.

[149] Hsiu-Wei Cheng, Philipp Stock, Boaz Moeremans, Theodoros Baimpos, Xavier Banquy, Frank Uwe Renner, and Markus Valtiner. Characterizing the Influence of Water on Charging and Layering at Electrified Ionic-Liquid/Solid Interfaces. *Adv. Mater. Interfaces*, 2(12), 2015.

[150] Alexander M Smith and Susan Perkin. Influence of Lithium Solutes on Double-Layer Structure of Ionic Liquids. *Phys. Chem. Lett.*, 6:4857–4861, 2015.

[151] H Cheng, J Dienemann, P Stock, C Merola, Y Chen, and M Valtiner. The Effect of Water and Confinement on Self-Assembly of Imidazolium Based Ionic Liquids at Mica Interfaces. *Sci. Rep.*, 6(30058):1–9, 2016.

[152] Alberto Bianco, Hui-ming Cheng, Toshiaki Enoki, Yury Gogotsi, Robert H Hurt, Nikhil Koratkar, Takashi Kyotani, Marc Monthioux, Chong Rae Park, Juan MD Tascon, and Jin Zhang. All in the graphene family – A recommended nomenclature for two-dimensional carbon materials. *Carbon*, 65:1–6, 2013.

[153] Xuan Wang, Linjie Zhi, and Klaus Müllen. Transparent, conductive graphene electrodes for dye-sensitized solar cells. *Nano Lett.*, 8:323–327, 2008.

[154] Sukang Bae, Hyeongkeun Kim, Youngbin Lee, Xiangfan Xu, Jae-Sung Park, Yi Zheng, Jayakumar Balakrishnan, Tian Lei, Hye Ri Kim, Young Il Song, Young-Jin Kim, Kwang S. Kim, Barbaros Özyilmaz, Jong-Hyun Ahn, Byung Hee Hong, and Sumio Iijima. Roll-to-roll production of 30-inch graphene films for transparent electrodes. *Nat. Nanotechnol.*, 5(8):574–578, 2010.

[155] Steven P Koenig, Narasimha G Boddeti, Martin L Dunn, and J Scott Bunch. Ultrastrong adhesion of graphene membranes. *Nat. Nanotechnol.*, 6(9):543–546, 2011.

[156] Auren Ferguson, Ivan T Ca, Claudia Backes, Jonathan N Coleman, and Shane D Bergin. Differentiating Defect and Basal Plane Contributions to the Surface Energy of Graphite Using Inverse Gas Chromatography. *Chem. Mater.*, 28:6355–6366, 2016.

[157] Andrew Kozbial, Feng Zhou, Zhiting Li, Haitao Liu, and Lei Li. Are Graphitic Surfaces Hydrophobic? *Acc. Chem. Res.*, 49:2765–2773, 2016.

[158] D. K. Owens and R. C. Wendt. Estimation of the Surface Free Energy of Polymers. *J. Appl. Polym. Sci.*, 13:1741–1747, 1969.

[159] F.M. Fowkes. Determination of Interfacial Tensions, Contact Angles, and Dispersion Forces in Surfaces by Assuming Additivity of Intermolecular Interactions in Surfaces. *J. Phys. Chem.*, 66(2):382, 1962.

[160] Zhiting Li, Yongjin Wang, Andrew Kozbial, Ganesh Shenoy, Feng Zhou, Rebecca McGinley, Patrick Ireland, Brittni Morganstein, Alyssa Kunkel, Sumedh P Surwade, Lei Li, and Haitao Liu. Effect of airborne contaminants on the wettability of supported graphene and graphite. *Nat. Mater.*, 12(10):925–31, 2013.

[161] Elad Koren, Colin Rawlings, Armin W Knoll, and Urs Duerig. Adhesion and friction in mesoscopic graphite contacts. *Science*, 348(6235):679–684, 2015.

[162] Wen Wang, Shuyang Dai, Xide Li, Jiarui Yang, David J. Srolovitz, and Quanshui Zheng. Measurement of the cleavage energy of graphite. *Nat. Commun.*, 6:7853, 2015.

[163] Peng Li, Zheng You, and Tianhong Cui. Adhesion energy of few layer graphene characterized by atomic force microscope. *Sens. Act.*, 217:56–61, 2014.

[164] Jun Wang, Dan C Sorescu, Seokmin Jeon, Alexei Belianinov, Sergei V Kalinin, Arthur P Baddorf, and Petro Maksymovych. Atomic intercalation to measure adhesion of graphene on graphite. *Nat. Commun.*, 7:1–7, 2016.

[165] Leonardo Spanu, Sandro Sorella, and Giulia Galli. Nature and Strength of Interlayer Binding in Graphite. *Phys. Rev. Lett.*, 103(19):1–4, 2009.

[166] S. Lebègue, J. Harl, Tim Gould, J. G. Ángyán, G. Kresse, and J. F. Dobson. Cohesive Properties and Asymptotics of the Dispersion Interaction in Graphite by the Random Phase Approximation. *Phys. Rev. Lett.*, 105(19):196401, 2010.

[167] T. Björkman, A. Gulans, A.V. Krasheninnikov, and R.M. Nieminen. Van der Waals bonding in layered compounds from advanced density-functional first-principles calculations. *Phys. Rev. Lett.*, 108(June):1–5, 2012.

[168] John F. Dobson, Tim Gould, and Giovanni Vignale. How many-body effects modify the van der waals interaction between graphene sheets. *Phys. Rev. X*, 4(2):1–9, 2014.

[169] H.K. Christenson. Adhesion and Surface Energy of Mica in Air and Water. *J. Phys. Chem.*, 97:12034–12041, 1993.

[170] K.L.; Johnson, K.; Kendall, and A.D. Roberts. Surface energy and the contact of elastic solids. *Proc. R. Soc. Lond. A*, 304:301–313, 1971.

[171] Daniel Maugis. Adhesion of Spheres : The JKR-DMT Transition Using a Dugdale Model. *J. Colloid Interface Sci.*, 150(1):243–269, 1992.

[172] P M McGuiggan, J S Wallace, D T Smith, I Sridhar, Z W Zheng, and K L Johnson. Contact mechanics of layered elastic materials: experiment and theory. *J. Phys. D. Appl. Phys.*, 40(19):5984–5994, 2007.

[173] Keith R. Paton, Eswaraiah Varrla, Claudia Backes, Ronan J. Smith, Umar Khan, Arlene O'Neill, Conor Boland, Mustafa Lotya, Oana M. Istrate, Paul King, Tom Higgins, Sebastian Barwich, Peter May, Pawel Puczkarski, Iftikhar Ahmed, Matthias Moebius, Henrik Pettersson, Edmund Long, João Coelho, Sean E. O'Brien, Eva K. McGuire, Beatriz Mendoza Sanchez, Georg S. Duesberg, Niall McEvoy, Timothy J. Pennycook, Clive Downing, Alison Crossley, Valeria Nicolosi, and Jonathan N. Coleman. Scalable production of large quantities of defect-free few-layer graphene by shear exfoliation in liquids. *Nat. Mater.*, 13(6):624–630, 2014.

[174] Hongbo Zeng, Jun Huang, Yu Tian, Lin Li, Matthew V Tirrell, and Jacob N Israelachvili. Adhesion and Detachment Mechanisms between Polymer and Solid Substrate Surfaces: Using Polystyrene - Mica as a Model System. *Macromolecules*, 49:5223–5231, 2016.

[175] Andrew Kozbial, Charles Trouba, Haitao Liu, and Lei Li. Characterization of the Intrinsic Water Wettability of Graphite Using Contact Angle Measurements: Effect of Defects on Static and Dynamic Contact Angles. *Langmuir*, 33(4):959–967, 2017.

[176] Shangchao Lin, Chih Jen Shih, Michael S. Strano, and Daniel Blankschtein. Molecular insights into the surface morphology, layering structure, and aggregation kinetics of surfactant-stabilized graphene dispersions. *J. Am. Chem. Soc.*, 133(32):12810–12823, 2011.

[177] Pinshane Y Huang, Carlos S Ruiz-Vargas, Arend M van der Zande, William S Whitney, Mark P Levendorf, Joshua W Kevek, Shivank Garg, Jonathan S Alden, Caleb J Hustedt, Ye Zhu, Jiwoong Park, Paul L McEuen, and David A Muller. Grains and grain boundaries in single-layer graphene atomic patchwork quilts. *Nature*, 469(7330):389–92, 2011.

[178] James Annett and Graham L. W. Cross. Self-assembly of graphene ribbons by spontaneous self-tearing and peeling from a substrate. *Nature*, 535(7611):271–275, 2016.

[179] L.A. Girifalco and R.A. Lad. Energy of Cohesion, Compressibility, and the Potential Energy Functions of the Graphite System. *J. Chem. Phys.*, 25(4):693, 1956.

[180] Lorin X Benedict, Nasreen G Chopra, Marvin L Cohen, A Zettl, Steven G Louie, and Vincent H Crespi. Microscopic determination of the interlayer binding energy in graphite. *Chem. Phys. Lett.*, 286(5):490–496, 1998.

[181] Renju Zacharia, Hendrik Ulbricht, and Tobias Hertel. Interlayer cohesive energy of graphite from thermal desorption of polyaromatic hydrocarbons. *Phys. Rev. B*, 69(15):1–7, 2004.

[182] Zhiting Li, Andrew Kozbial, Nikoloz Nioradze, David Parobek, Ganesh Jagadeesh Shenoy, Muhammad Salim, Shigeru Amemiya, Lei Li, and Haitao Liu. Water Protects Graphitic Surface from Airborne Hydrocarbon Contamination. *ACS Nano*, 10(1):349–59, 2016.

[183] Ali Ashraf, Yanbin Wu, Michael C Wang, Narayana R Aluru, Seyed A Dastgheib, and Sungwoo Nam. Spectroscopic Investigation of the Wettability of Multilayer Graphene Using Highly Ordered Pyrolytic Graphite as a Model Material. *Langmuir*, 30:12827–12836, 2014.

[184] S. Yang, E.S. Kooij, B. Poelsema, D. Lohse, and H.J.W. Zandvliet. Correlation between geometry and nanobubble distribution on HOPG surface. *Europhys. Lett.*, 81, 2008.

[185] Leo Garcia, Lea Jacquot, Elisabeth Charlaix, and Benjamin Cross. Nano-mechanics of ionic liquids at dielectric and metallic interfaces. *Faraday Discuss.*, 206:443–457, 2018.

[186] Jean Comtet, Antoine Niguès, Vojtech Kaiser, Benoit Coasne, Lydéric Bocquet, and Alessandro Siria. Nanoscale capillary freezing of ionic liquids confined between metallic interfaces and the role of electronic screening. *Nat. Mater.*, 16(June):634–639, 2017.

[187] Sho Fujii, Motohiro Kasuya, and Kazue Kurihara. Characterization of Platinum Electrode Surfaces by Electrochemical Surface Forces Measurement. *J. Phys. Chem. C*, 121(47):26406–26413, 2017.

[188] Salmaan H Baxamusa, Sung Gap Im, and Karen K Gleason. Initiated and oxidative chemical vapor deposition: a scalable method for conformal and functional polymer films on real substrates. *Phys. Chem. Chem. Phys.*, 11(26):5227–5240, 2009.

Appendix:
A. List of Symbols

D	Surface separation
E	Young's modulus
ϵ	Relative permittivity
F	Force
I	Intensity
K_L	Lateral spring constant
K_N	Normal spring constant
λ	Wavelength
μ	Relative permeability
n	Refractive index
$\tilde{n}$	Complex refractive index
P(D)	Primary fringes (dependant on surface separation, D)
R	Radius of curvature
R*	Reflectance
R_G	Radius of curvature at the surface of the gSFB lens
R_L	Radius of curvature of the gold-coated quartz lens underneath the epoxy/graphene
R_S	Radius of curvature of the secondary fringes
$R_{G\parallel}$	Radius of curvature along the apex of the cylindrical gSFB lens
$R_{G\perp}$	Radius of curvature perpendicular to the cylindrical gSFB lens
S	Secondary fringe
T	Transmission
T(D)	Tertiary fringe (dependent on the surface separation, D)
T*	Transmittance
T_g	Glass transition temperature
θ	Angle of incidence with respect to the surface normal
Θ	Contact angle
Ξ	Degrees of freedom; parameter space
Z	Spacer layer thickness

Appendix:
B. List of Abbreviations

AcH	Acetic acid
AFM	Atomic force microscope/microscopy
APS	Ammonium persulphate
Ar	Argon (gas)
BSE	Back scattered electron
Bz-Cl	Chlorobenzene
CCD	Charge coupled device
CM-AFM	Contact mode AFM
CVD	Chemical vapour deposition
DCB	1,2-Dichlorobenzene
DI	Deionized water
EDX	Energy dispersive x-ray spectroscopy
EP1	Electropolishing recipe 1
EP2	Electropolishing recipe 2
EPON	EPON resin 1004F
EpoThin	Buehler EpoThin 2 Resin
EtAc	Ethyl acetate
EtOH	Ethanol
FECO	Fringes of equal chromatic order
FLG	Few layer graphene as grown using the procedures presented in this thesis
FWHM	Full width half maximum
gSFB	graphene Surface Force Balance
H_2	Hydrogen (gas)
H_2/Ar	2.5% hydrogen in argon (gas)
HOPG	Highly oriented pyrolythic graphite
IPA	2-propanol
JKR	Contact mechanics model named after Johnson, Kendall and Roberts
MBI	Multiple beam interferometry
Me	Methane (gas)
Me/Ar	250 ppm methane in argon (gas)
MFC	Mass flow controller
MIBK	4-methyl-2-pentanone
MMM	Multilayer matrix method
mmSLG	Single layer graphene with a diameter $\geq$ 1 mm

B.1 List of Abbreviations (Continued)

NaCh	Aqueous sodium cholate solution
OM	Optical microscopy
PC	Polycarbonate
PDMS	Polydimethylsiloxane
PMMA	Poly(methyl methacrylate)
PS	Polystyrene
PTFE	Polytetrafluoroethylene
PVD	Physical vapour deposition
Raman	Raman spectroscopy
SE	Secondary electron
SEM	Scanning electron microscope/microscopy
SFA	Surface force apparatus
SFB	Surface force balance
TM-AFM	Tapping mode AFM
Tol	Toluene
WCA	Water contact angle
XPS	X-ray photoelectron spectroscopy

Appendix:
C. Clean Handling & Practices

C.1 Flowhood operation: keeping it clean

C.1.1 Laminor flow hoods

Cleaving mica may yield large atomically smooth facets. However, this feature may only be utilized if the surface stays free of (particulate) contamination. Prompted for example by the requirement for particle-free environments in the (semiconductor) electronics industry, filtration systems have been developed to provide working environments low in particulate content. Such "cleanrooms" (Figure C.1) are classified by the number of particulates they contain. Due to the high cost of operating a cleanroom, we cleave mica in a laminar flowhood (LFH).

A LFH operates under the same principles as a cleanroom. Similarly to a cleanroom, air is passed through an air filter, with laminar outward flow preventing influx of particulates. The filters are either "high-efficiency particulate absorption" (HEPA) or "ultra-low particulate air" (ULPA) filters. To put the use of an LFH into context: ambient air contains about a billion particulates with a diameter larger than 100 nm per cubic meter (appendix Figure C.2). Our LFH (BassAire, model P4HF, # PH334) has 2 filters. The first filters 92% of particles > 5 μm. The second filter is a HEPA filter with filter-classification H14, reducing this number to 50000 per cubic meter. This would translate to an ISO 5 class cleanroom environment, according to the ISO14644-1 standard (Figure C.2).

C.1.2 LFH setup and operation

The laminar flow provides a relatively particulate-free environment. However, cleanliness is only guaranteed in the areas where the laminar flow is unobstructed. Figure C.3, shows a schematic of the SFB-flow hood, the tools in front of the SFB will not be as clean as the dishes in the back left. Prior to every SFB experiment, it is important to ensure all the equipment used in the experiment is clean.

C.1.3 Cleaning tools and surfaces

SFB Cleaning

Upon placement in the LFH, blow off the SFB with N_2 (outward) and wipe the surfaces with EtOH, using a cleanroom wipe. The SFB can be filled with solvent (if necessary) and dried with N_2. The N_2 is blown through a gun with a particle filter.

LFH Cleaning

The LFH is cleaned by blowing out with N_2, then rinsing with EtOH and dilute HNO_3. (HNO_3:H_2O = 1:10). The role of HNO_3 is to dissolve metals and salts, and oxidize organics. HNO_3 oxidizes a number of metals, including steel. However, its oxidizing nature "passivates" the stainless steel surface, by removing Fe and forming a protective Cr_2O_3 (and NiO)-layer. Removal of "exposed" Fe(-rich) areas, prevents oxidation.

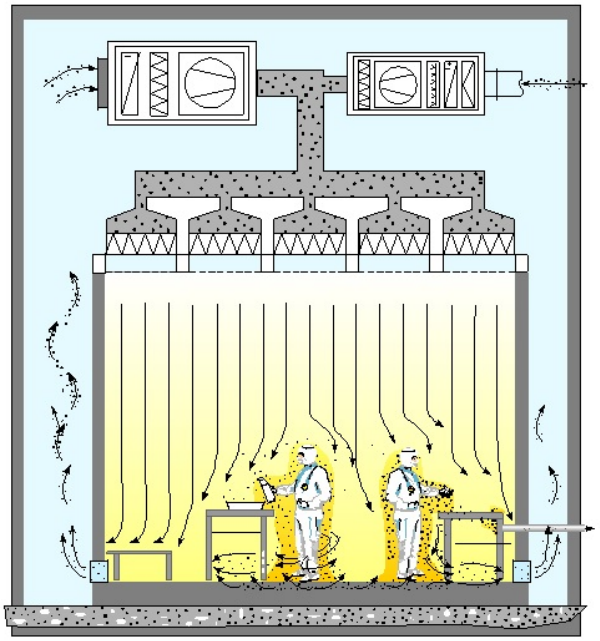


Figure C.1: *Air flow pattern for laminar flow in a cleanroom, designed to keep particulate contamination in the working areas as low as possible. The air is passed through HEPA- or ULPA-filters, designed to intercept particulates. Source: http://en.wikipedia.org/wiki/Cleanroom, visited 2017-10-18.*

Tools

Stainless steel tools are first degreased with EtOH (possibly in combination with sonication) and Toluene. Subsequently they are treated with diluted HNO_3 After the HNO3-treatment, tools are stored in EtOH, in a Piranha – H2O2 : H2SO4 = 1:3 – cleaned beaker covered with Aluminum foil.

Non-stainless steel items

Non-stainless steel items are preferentially made out of water insoluble polymers with high chemical resistance such as Teflon (PTFE, poly(tetrafluorethylene)), Delrin (POM, poly(oxomethylene)) or Kel-F. These are poorly wetted by aqueous solutions, preventing them from fouling (i.e. becoming contaminated with organics originating from microbial activity in water) and allowing them to be cleaned in aggressive aqueous etchants, such as HNO_3.

Glassware

Glassware is cleaned with Piranha solution (H_2O_2 : H_2SO_4 = 1:3). This will remove organics and most metals. If no H_2O_2 is available, NoChromix (mainly ammonium persulfate $(NH_4)_2S_2O_8$), may be used. Both mixtures cause fast dehydration and hydrolysis due to the presence of sulfuric acid (which efficiently cleans organics in itself, e.g. it was used as drain cleaner) and produce highly reactive O-radicals that turn organics into CO_2. *(Make sure whatever you're cleaning has been rinsed with H_2O prior to being piranha-cleaned, since piranha will react violently with solvents.)*

C.2 Cleaving mica

Mica is cleaved in a dedicated flow hood (see Figure C.4). Mica can be cleaved by rubbing its edge with a needle to expose the facets and subsequently inserting the needle in the roughened area. Next the area pulled up by the needle is carefully grabbed as to separate

Class	maximum particles/m³						FED STD 209E equivalent
	≥0.1 µm	≥0.2 µm	≥0.3 µm	≥0.5 µm	≥1 µm	≥5 µm	
ISO 1	10	2.37	1.02	0.35	0.083	0.0029	-
ISO 2	100	23.7	10.2	3.5	0.83	0.029	-
ISO 3	1,000	237	102	35	8.3	0.29	Class 1
ISO 4	10,000	2,370	1,020	352	83	2.9	Class 10
ISO 5	100,000	23,700	10,200	3,520	832	29	Class 100
ISO 6	1,000,000	237,000	102,000	35,200	8,320	293	Class 1,000
ISO 7	10,000,000	2,370,000	1,020,000	352,000	83,200	2,930	Class 10,000
ISO 8	100,000,000	23,700,000	10,200,000	3,520,000	832,000	29,300	Class 100,000
ISO 9	1,000,000,000	237,000,000	102,000,000	35,200,000	8,320,000	293,000	Room air

Figure C.2: *ISO14644-1 Clean room air quality standards. Source: http://en.wikipedia.org/wiki/Cleanroom, visited 2017-10-18.*

the two surfaces. Tearing can also induce cleavage. During cleaving it is imperative to ensure the cleaved (clean) side is always facing unblocked laminar flow.

C.2.1 The base sheet

A base-sheet is cleaved off a thick mica sheet. The starting sheet is placed in the "toast-rack" at the back left of the flow hood, with the clean side facing in (Figure C.4). The base sheet may be placed on a clean dish, clean side up. It is on here that the cleaved mica facets will be placed from back to front. Ideally, a base sheet is used within 1 hour of exposure, to prevent contamination.

C.2.2 Getting the right facet

The thinner the mica, the higher the experimental resolution and the higher its flexibility and fragility. Mica that is very thin (down to 2 μm), but still allows for handling during lens preparation is therefore desired. Mica thickness is inferred from flexibility (thin mica flexibly moves in the flow of the LFH) and color. The color arises from internal interference due to the partial transmission/reflection of light at the mica/air interface. The thinner the mica is, the brighter (spectrally defined) this color will appear.

C.2.3 Cutting the mica

When after cleaving, a facet of the right thickness is identified, it has to be isolated from the rest of the sheet. This is done by cutting it with a current (Joule) heated Pt-wire. The cutting direction needs to prevent Pt nanoparticles from landing on the substrate by choosing the right direction with respect to laminar flow (see Figure C.5). Since the hot air from the wire locally pushes particles up, the facet needs to be turned over as it is laid down on the base sheet.

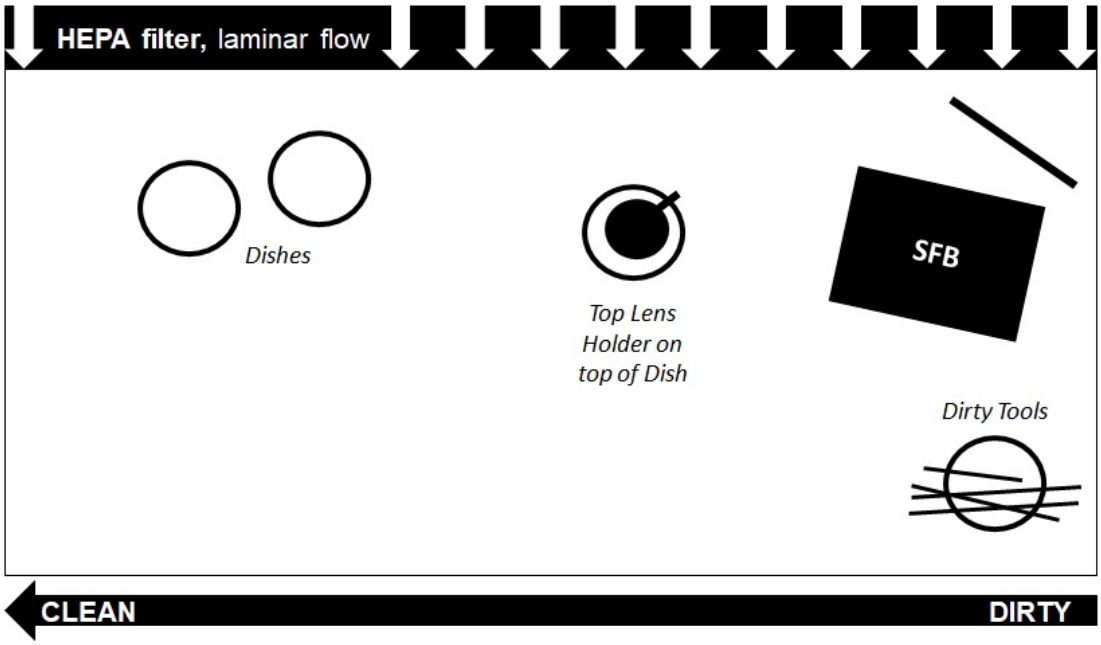


Figure C.3: *Schematic showing a typical lay-out of a LFH with the SFB.*

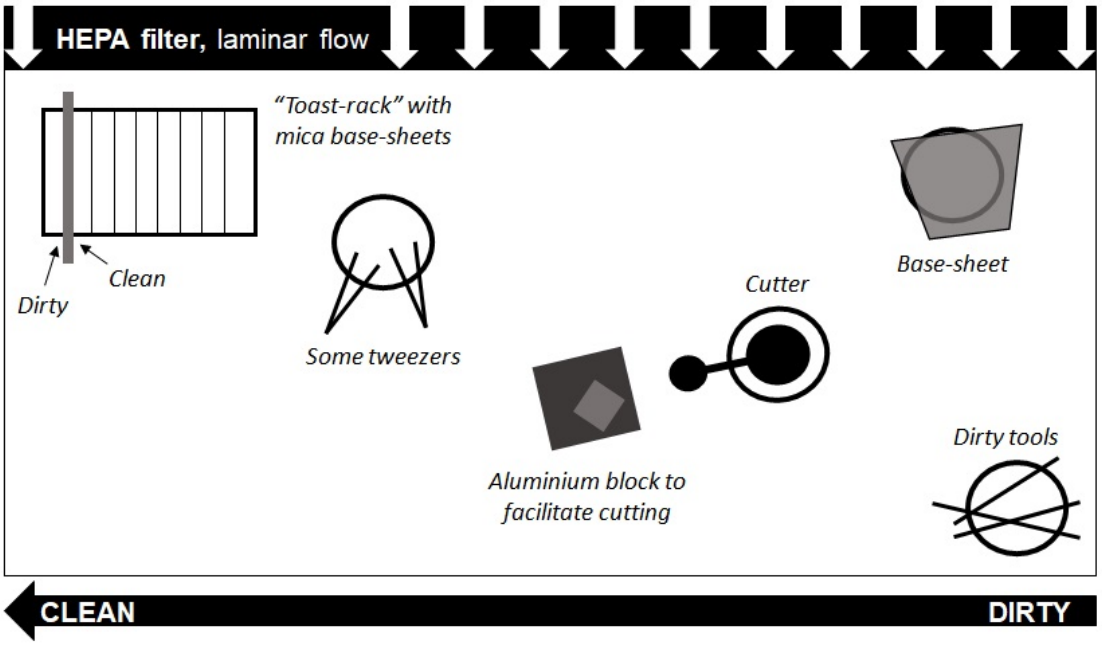


Figure C.4: *Schematic showing a typical lay-out of a LFH for cleaving mica.*

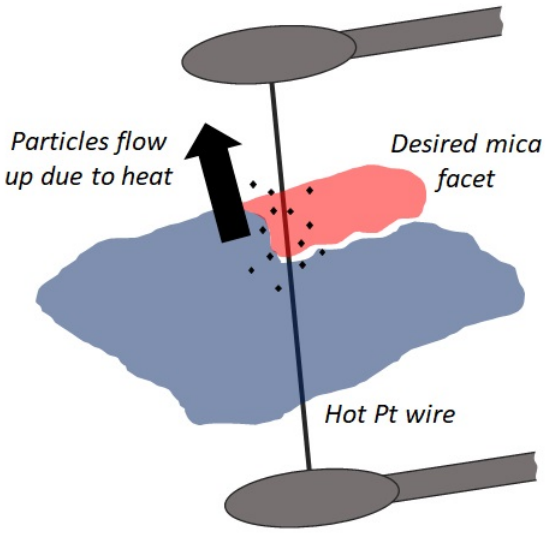


Figure C.5: *Schematic showing a Pt-wire cutting a mica facet.*